Università degli Studi di Trieste

Doctoral Thesis

Force and temperature measurements on DNA-based nanostructures

---

Author:
Valeria Cotta

Supervisor:
Dr. Dan Cojoc,
Dr. Marco Lazzarino

*A thesis submitted in fulfillment of the requirements
for the degree of Doctor of Philosophy*

in the

PhD Course in Nanotechnology

Funding agency: PO FRIULI VENEZIA GIULIA - FONDO SOCIALE EUROPEO 2014/2020

Contents

Abstract

Il lavoro di ricerca presentato in questa tesi di Dottorato riguarda lo sviluppo di un nanosistema in grado di indurre contemporaneamente variazioni di temperatura e di forza su una biomolecola di interesse – nel nostro caso, una hairpin di DNA a singolo filamento (ssDNA). Questo progetto si inserisce in un filone più ampio, volto a studiare gli effetti del riscaldamento localizzato sulle funzioni biologiche di strutture di DNA o proteine. Un approccio simile è stato utilizzato per esempio da Iwaki e collaboratori [7], i quali hanno costruito un sistema ad alta risoluzione per monitorare la dinamica di una molecola di miosina riscaldata localmente.

Allo scopo di investigare la dinamica di una hairpin di ssDNA a 24 coppie di basi, abbiamo progettato, sintetizzato e caratterizzato due diverse nanostrutture di DNA origami, le quali sono state utilizzate come supporti rigidi per la molecola di hairpin stessa. Grazie alla sua elevata versatilità, la nanotecnologia del DNA origami offre infatti la possibilità di creare dispositivi nella scala del nanometro con geometrie arbitrarie [3]. Inoltre, dato che le nanostrutture di DNA origami vengono realizzate sfruttando il preciso appaiamento delle basi di DNA, possono essere utilizzate per collocare nanoparticelle metalliche in posizioni specifiche, con precisione nanometrica.

Nel nostro schema, le nanoparticelle d'oro (AuNPs) sono state utilizzate come fonti di riscaldamento locale. Infatti, quando le AuNPs assorbono la luce alla frequenza di risonanza plasmonica, vengono indotte oscillazioni collettive degli elettroni liberi. Gli elettroni, interagendo con il reticolo cristallino delle AuNPs, rilasciano energia termica all'ambiente circostante e inducono così un riscaldamento localizzato [87].

Abbiamo testato e confrontato due metodi distinti per applicare forze nell'ordine del piconewton alla molecola di interesse. Nel primo caso, abbiamo eseguito misure di Magnetic Tweezing (MT) sulla hairpin, utilizzando una struttura rigida di DNA origami a quattro eliche come tramite tra la celletta del MT e le biglie magnetiche utilizzate per applicare la forza. Per fare ciò, abbiamo dovuto mettere a punto un apposito protocollo per effettuare misure di MT sugli origami. Nel secondo caso, abbiamo sfruttato il sensore di forza progettato da Nickels et al. [17] e basato sulla nanotecnologia del DNA origami per aprire la ssDNA hairpin. Questo nanodispositivo consiste in una struttura rigida caratterizzata da un filamento di ssDNA, il quale può esercitare forze dell'ordine del piconewton su una molecola di interesse, sfruttando le proprietà entropiche del DNA. Abbiamo tuttavia modificato il disegno originale del nanosensore di forza in modo da posizionare la ssDNA hairpin nella regione centrale a singolo filamento, dove viene applicata la forza entropica. Le variazioni conformazionali della hairpin sono state monitorate tramite misure di Förster Resonance Energy Transfer (FRET). Infatti, quando la forza entropica del nanodispositivo di DNA origami è pari alla forza di apertura e chiusura della hairpin, dovrebbe verificarsi una transizione tra gli stati 'aperto' e 'chiuso' della molecola stessa, dando quindi origine ad un segnale FRET a due livelli. Nei casi limite in cui la hairpin si trova sempre nella configurazione chiusa o aperta, il segnale FRET dovrebbe invece rimanere costante, con efficienza rispettivamente pari a 1 o a 0. A differenza degli esperimenti FRET tradizionali, nel nostro caso è stato fondamentale confrontare tra loro i risultati di diversi nanosensori, ciascuno caratterizzato da una forza entropica costante e quindi da una ben fissata conformazione della hairpin.

Entrambi gli approcci hanno confermato che la forza di apertura della hairpin di interesse corrisponde a F=12 pN ± 1 pN. Tuttavia, il sensore di forza di DNA origami rappresenta un metodo

migliore per applicare forze controllate ad una biomolecola bersaglio, in quanto permette di superare una delle principali limitazioni della spettroscopia di forza dovuta alla presenza di interazioni non-specifiche tra la superficie della celletta del MT e la molecola in esame.

Abbiamo infine attaccato una nanoparticella d'oro di 10 nm di diametro al sensore di forza di DNA origami, al fine di riscaldare localmente la biomolecola d'interesse in condizioni di risonanza plasmonica. In questo modo, il nostro sistema permette di studiare le proprietà di molecole di DNA controllando contemporaneamente la forza esercitata e la temperatura localmente indotta.

My PhD project was aimed at studying how local heating affects biological functions. More specifically, the research activity was focused on the development of a nanosystem apt to simultaneously control the effects of temperature and force variations on a biomolecule of interest. A similar approach has been used also by Iwaki and coworkers [7], who constructed indeed an observation system to monitor single myosin dynamics under local heating with high resolution.

To the purpose of investigating the dynamics of a 24 base-pairs long single-strand DNA (ssDNA) hairpin, we designed, synthesized and characterized two different DNA origami nanostructures that were used as rigid holders for the ssDNA hairpin. Due to its nearly unlimited design flexibility, the DNA origami nanotechnology provides indeed an unmatched platform for the realization of structures and devices at the nanoscale [3]. Moreover, because of their unique self-recognition properties, DNA origami can be employed to organize metal particles in desired geometries with nanometric precision. In our scheme, gold nanoparticles (AuNPs) were used as local heating sources. In fact, when AuNPs absorb light at the plasmon resonance frequency, collective oscillations of the free electrons are induced. Upon interaction between the electrons and the crystal lattice of the AuNPs, the electrons relax and the thermal energy is transferred to the surrounding environment, thus inducing local heating [87].

We tested and compared two distinct methods to apply piconewton forces to the target hairpin. In the first case, we performed Magnetic Tweezer (MT) measurements on the ssDNA hairpin by using a stiff 4-helix bundle DNA origami as a tether between the MT flow cell and the magnetic beads used to apply the force. We thus developed a specific protocol to include the ssDNA hairpin in the origami nanostructure - in order to increase the overall stability and rigidity of the system - and to measure it with the MT technique. In the second case, we exploited the DNA origami force-sensor designed by Nickels et al. [17] to stretch the target hairpin. This nanodevice consists of a rigid supporting structure characterized by a ssDNA filament that can exert forces in the low piconewton range on a molecule of interest by exploiting the entropic properties of DNA. We modified the original design of the force clamp in order to place the target ssDNA hairpin in the central region of the sensor, where the entropic force is applied. Conformational transitions were monitored by single-molecule Förster Resonance Energy Transfer (FRET). In fact, when the entropic force of the force clamp equals the unzipping force of the hairpin, a transition between the open and the closed states should occur, thus determining a two-state FRET signal. Nonetheless, in the limiting cases in which the hairpin is constantly either zipped or unzipped, the FRET signal should remain constant and the corresponding efficiency should respectively be 1 or 0. Unlike traditional FRET experiments, in our case, it was hence fundamental to compare the data from different DNA origami force sensors, as each one is characterized by a constant entropic force and therefore by a well-established conformation of the hairpin.

Both approaches confirmed that the unzipping force of the target hairpin corresponds to $F=12$ pN $\pm$ 1 pN. Nonetheless, the DNA origami force sensor represents a better method to apply controlled tensions to a target biomolecule, as it overcomes the main limitation of force spectroscopy due to unspecific interactions with the surface of the MT flow cell.

We finally attached a single 10 nm AuNP to the force-sensor DNA origami to allow heat generation in plasmonic resonance conditions. In this way, our new force system can be employed for further investigations that include both force and temperature control.

Chapter 1

Introduction

In his famous speech *There's Plenty of Room at the Bottom* [1], Richard Feynman addresses the problem of "manipulating and controlling things on a small scale". After challenging the audience to answer the question "Why cannot we write the entire 24 volumes of the Encyclopaedia Britannica on the head of a pin?", Feynman draws the attention of the physicists to the ′marvellous biological system. He points out that "Biology is not simply writing information; it is doing something about it". He thus wishes that "we too can make a thing very small, which does what we want - that we can manufacture an object that manoeuvers at that level!".
In the last 30 years, the field of the DNA origami nanotechnology has accomplished this goal. Since the pioneering work of Ned Seeman in 1992, who realized the first DNA nanostructure [2], and the original paper of Paul Rothemund in 2006, which set the basis of the DNA origami technique, there has been indeed a pursuit to build DNA-based artificial system that can control geometry, motion and optical properties at the nanoscale and that can mimic biological functions such as walking, sliding or rotating [4].

In this PhD thesis, I will present several DNA-based structures that were used to investigate how force and temperature act at the nanoscale. In particular, we were interested in studying how local temperature variations - as those induced by the plasmons generated in gold nanoparticles - can influence the mechanical properties of simple biomolecules, such as a single-strand DNA (ssDNA) hairpin. This work can be a starting point for establishing a method to study more complex macromolecules, such as proteins. Measurement of protein stability in different mechanical and thermal conditions is indeed central to understanding their structure, function and role in diseases. While proteins are also sought as therapeutic agents, they can cause diseases by misfolding and aggregation in vivo. We thus envision possible bio-medical applications for our study [5] [6].
A similar approach has been followed by Iwaki et al. [7] to study the influence of local heating on the myosin movement by using a DNA origami bundle to precisely control the distance between the myosin and the nanoparticle. The researchers were able to control thermal gradients in the order of $0.1\,\mathrm{K\,nm^{-1}}$. They further applied a DNA origami nanospring to study the movement of myosin under a mechanical tension and found that mechanical force could induce the transition of myosin heads from the nonadjacent binding state to the adjacent binding state [8].
Baffou and coworkers [12] developed thermodynamic arguments to show that temperature variations inside cells can be on the order of $\Delta T \approx 10^{-5}$ K, conversely to what claimed by K. Okabe et al. [13], who reported temperature increases of around 1 K. Even without assuming thermogenesis inside cells, controlling heat at the nanoscale can be useful for a deeper understanding of biochemical phenomena, such as enzymatic reactions and protein folding. It has been proven that local heating itself can also induce local gene expression [9], membrane depolarization [10], and muscle contraction [11].
We then studied how heat is generated in clusters of DNA-mediated gold nanoparticles (AuNPs) in surface plasmon resonance conditions (see Chapter 6). In this configuration, the DNA dehybridization process was used as a probe. To the purpose of studying how local heating is produced with single AuNPs - thus avoiding collective effects - we designed and validated a complex system made up of a DNA origami nanostructure and a target biomolecule (a ssDNA

hairpin). DNA origami nanotechnology offers indeed the possibility to precisely control composite nanoscale geometries and functionalizations and to assemble AuNPs at precise locations, while manipulating single molecules [14]. We then created two different systems in which a rigid DNA origami was decorated with a single AuNP and a ssDNA hairpin, directly inserted into the DNA nanostructure, was expected to act as a probe of local heating. As a starting point, we characterized the dynamics of the target hairpin in the DNA origami system at constant temperature. Forces at the nanoscale were controlled by performing Magnetic Tweezing (MT) (as described in Chapter 4) and DNA origami force spectroscopy (Chapter 5) experiments.
Magnetic tweezing is a single-molecule force technique that allows manipulation of biomolecules [15] by applying an external magnetic field to superparamagnetic beads specifically bound to the polymer of interest. The resulting forces are in the range between 0.1-100 pN. In a recent work, Pfitzer et al [55]. showed that using DNA origami structures as tethers in a MT setup reduces noise with respect to double-strand DNA (dsDNA) anchors. This work led us to design a rigid 4-helix bundle DNA origami that was internally modified to include the target ssDNA hairpin and to use it to investigate the dynamics of the hairpin. A 20 nm AuNP was also attached to the origami as a potential heating source. By performing MT experiments, we were able to measure the unzipping force of the hairpin.
We also tested an alternative approach for applying forces at the nanoscale which was presented in a work of Nickels et al. [17] and which is based on a DNA origami nanodevice that exploits the entropic force generated by a ssDNA spring. In this case, the dynamics of the ssDNA hairpin was monitored with single-molecule Förster Resonance Energy Transfer with the addition of two fluorophores placed at the extremities of the hairpin (see Chapter 5). These experiments confirmed the results obtained with the MT.
Finally, in Chapter 7, I will present a side-project that used a AuNPs-DNA-origami composite to investigate the forces generated by a complex DNA origami system that imitates motor proteins and that can undergo sliding after the addition of suitable oligonucleotides [16]. Also in this study, a multi-helix bundle was used as a tether for performing MT experiments, with the aim of detecting nanometric movements of the main sliding structure.

A systematic description of the fundamental properties of the DNA molecules and of the DNA origami nanostructures is presented in Chapters 2 and 3. In Chapter 3 the main experimental techniques used to study the physiochemical properties of the DNA origami, such as Transmission Electron Microscopy and gel electrophoresis, are also illustrated. The other experimental methods used to characterize the DNA-based structures, *i.e.* Magnetic Tweezing, Förster Resonance Energy Transfer and Surface Plasmon Resonance Spectroscopy, are explained respectively at the beginning of Chapters 4, 5 and 6, before the presentation of the corresponding experimental results.

The research project presented in this thesis was done in collaboration with the Ludwig Maximilians Universitaet in Munich. In particular, the experiments described in chapters 3, 4, 5 and 7 were carried out at the Ludwig Maximilians Universitaet in the group of Prof. Tim Liedl.

Chapter 2

The DNA origami nanotechnology

2.1 The DNA origami nanotechnology

2.1.1 DNA origami: a bottom-up self-assembly technique

The issue of building nanostructures can be addressed with two different methods: top-down and bottom-up fabrication. In top-down nanotechnology, large substrates are modified and modelled with manipulation tools to produce nanostructures in series. On the other hand, in bottom-up nanotechnology ordered nanosystems are produced by exploiting the recognition mechanism of biomolecules without any external guidance. In self-assembly, an ordered complex system forms from a disordered group of pre-existing building blocks that can interact between themselves in a specific way.

A successful example of a bottom-up self-assembly technique is the DNA origami nanotechnology, which uses DNA oligonucleotides as building blocks and enables the synthesis of a complex nanostructure with desired characteristics such as shape, dimensions and tensegrity. Using DNA as a construction material at the nanoscale offers several advantages, such as robustness, stability over a long period, ease of operation, modularity, biocompatibility and programmability. Concerning that, Paul Rothemund, the computational bioengineer at the California Institute of Technology in Pasadena who created the first DNA origami, said "the problem is that we don't just want to make small stuff, we want to make complicated small stuff, cheaply and easily".

2.1.2 DNA origami: a brief historical introduction

The concept behind DNA origami was laid down in the early 1980s by the crystallographer Nadrian Seeman, who realized that the ability of DNA molecules to carry and transfer information according to strict base-pairing rules could be used to rationally assemble structures with precisely controlled nanoscale features. Nadrian Seeman was driven by the research of an alternative way to perform X-ray crystallography experiments on non-soluble proteins, that could not be crystallized: his idea was then to design periodic three-dimensional lattices made of DNA to place and orientate proteins. To create a basic motif for the construction of regular, crystal-like structures, Seeman was guided by the study of the Holliday junction, a key motif in biology, that consists of a covalent phosphate linkage between two DNA duplexes. Several Holliday junctions can be bound together at the desired distance *via* sticky-end hybridization (*i.e.* short single-strands DNA sequences which protrude from a structure and which are complementary to the analogous complementary sequence on the other structure to be bound). Starting from this fundamental idea, in 1991 Seeman's group was able to create the first DNA based supramolecular assembly, a three-dimensional cube made of six ssDNA loops (see Figure 2.1) [2].

In 2006 Paul Rothemund published his pioneering work [3] which set the fundamentals of the DNA origami technique, based on the use of hundreds of synthetic short oligonucleotides (staples) to fold a 7 kilobases long viral genome (scaffold) into arbitrary shapes. In his design, he visualized how the genome could be folded into a predetermined, two-dimensional shape.

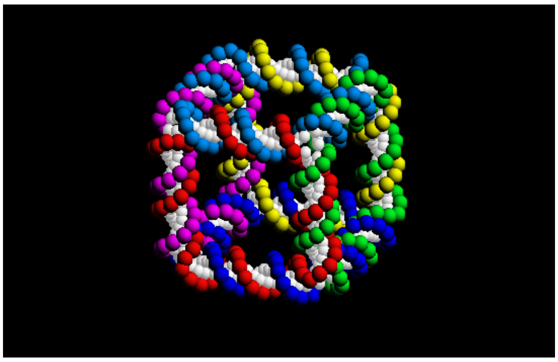

Figure 2.1: Model of the DNA cube created by N. Seeman in 1991 [2]. The cube contains six different cyclic strands: each nucleotide is represented by a single coloured dot for the backbone - respectively red (front), green (right), yellow (back), magenta (left), cyan (top) and dark blue (bottom) - and a single white dot representing the base. The helix axes of the molecule have the connectivity of a cube and the strands are linked to each other twice on every edge. The assembly of this nanostructure was realized by attaching specific sticky ends to a DNA branched junction, inspired by the biological Holliday junction.

Knowing the sequence of the virus at every twist and turn, he was able to write complementary DNA sequences, about 16-base-pairs long, that would essentially fold the staples in place. After mixing the staples and the scaffold in a suitable buffer and annealing them according to a specifically arranged thermal ramp, he obtained the famous smiley face and several other shapes illustrated in Figure 2.2.

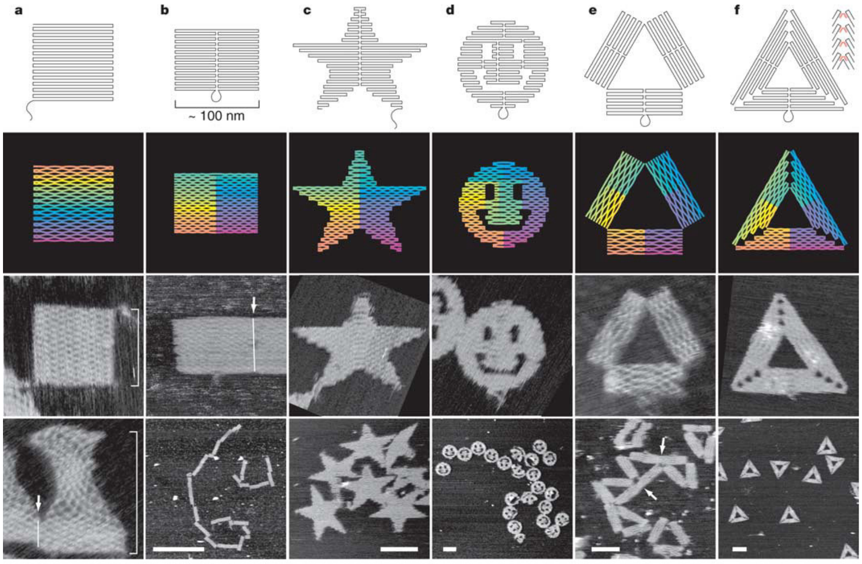

Figure 2.2: Schematic representations (first and seconds rows) and atomic force microscopy images (third and fourth rows) of the DNA origami nanostructures presented in P. Rothemund's paper in 2006 [3]

.

Since the synthesis of the first DNA nanostructures, much progress has been made in the field of the DNA origami nanotechnology. Researchers have first increased the complexity of two-dimensional (2D) nanostructures and then moved to the three-dimensional (3D) world.
For instance, Gothelf and co-workers [20] constructed a boxlike structure with an external size of $42 \times 36 \times 36\,\text{nm}^3$ that had a lid that could open or close in a boxlike way. They were able to create this reconfigurable DNA nanostructure by designing the scaffold to route through all

of the faces of the box and by introducing flexible hinges. In this case, the 2D planar structure was not completely paired with staples. Rather, the scaffold was intentionally left as a single strand in certain regions so that the relatively compact 2D planar structure could be broken into well-cut pieces, such as triangles and squares. Semi-rigid 2D shapes were then folded into 3D shapes when they joined with the matching well-cut pieces.

In 2009, Douglas et al.[21] reported on three-dimensional DNA origami nanostructures formed as pleated layers of helices constrained to a honeycomb lattice. In this case, they used a six-helix bundle as a basic unit and exploited the possibility to place crossovers at desired positions to induce the packing of duplexes in multi-layered 3D shapes (see Figure 2.3). By engineering 3D solid structures, they overcome the problem of conformational flexibility and structural heterogeneity observed in single-layered structures. Ke et al. reported a similar approach, based on a four-helix bundle, to achieve a square lattice alignment of the helices [22].

Dietz et al. expanded the multilayered design to include more complex structures that have programmable twists and curvatures [23]. Liedl and coworkers reported the synthesis of 3D prestressed tensegrity structures in which rigid bundles of DNA double helices resist compressive forces exerted by segments of single-stranded DNA that act as tension-bearing cables, thus inaugurating the field of the study of molecular forces [24].

3D origami structures, like the ones described above, were characterized by an increased range of spatial positioning that was not accessible by flat structures, thus expanding the range of possible applications to mimicking natural biosynthetic machines, such as a polymerase, ribosomes or chaperones, and even to create topological nanostructures, such as the Mobius strip designed by Yan and coworkers [25].

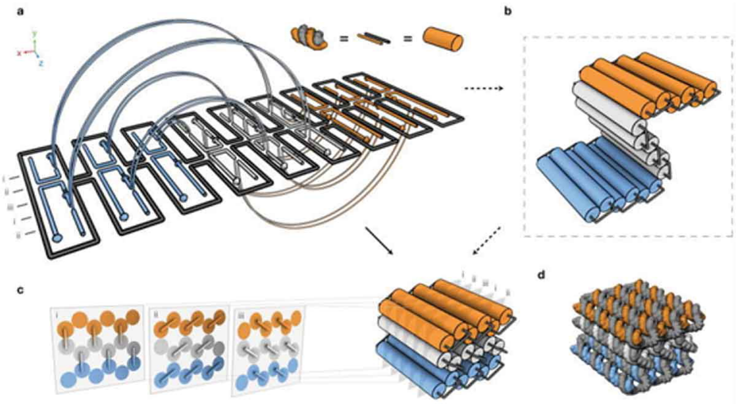

Figure 2.3: Schematic representation of the strategy used by Douglas et al. to build multi-layered 3D origami: crossovers were placed every 7 base-pairs, with an orientation of 120°, to connect adjacent double helices in a honeycomb lattice configuration [21]

Recently, one of the major interests in nanoscience has become the construction of macroscopic objects with programmable nanosized features by using DNA molecules as building blocks. A first attempt to create larger DNA origami structures has been made by extending the scaffold length with a variety of biotechnological methods [4]. Zhao et al. proposed instead a method, called "super DNA origami", that employs a conventional scaffold together with DNA tiles made of multiple strands to increase the size of an individual origami structure [26]. Finally, large-scale structures have been achieved by combining DNA origami molecules. Each DNA origami molecule can act as a DNA tile unit to form infinite crystal-like structures, or finite structures, through hierarchical self-assembly by taking advantage not only of the canonical hybridization interactions but also of base stacking, shape complementarity and template-assisted growth [27]. Atomic force microscopy (AFM) images of complex structures obtained from self-assembled DNA origami are illustrated in Figure 2.4.

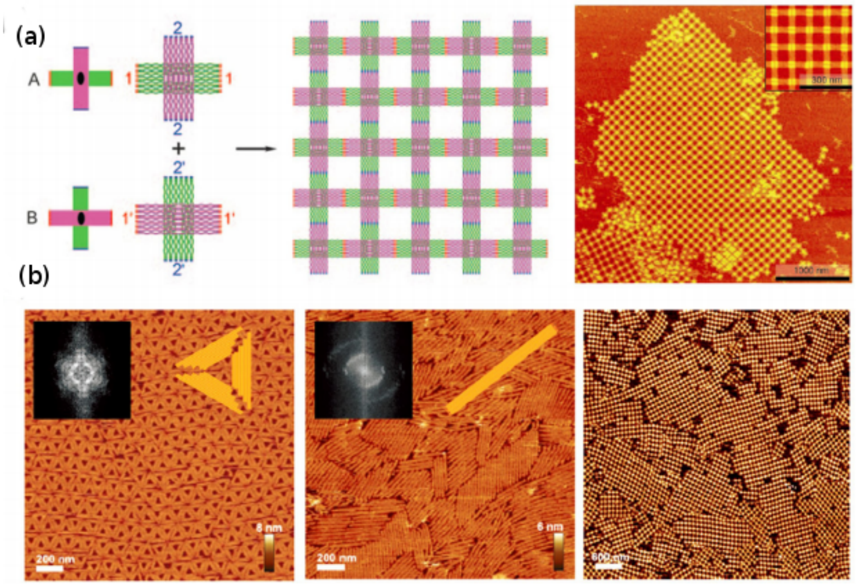

Figure 2.4: Scaling up DNA origami structures via hierarchical self-assembly. (a) Two cross-shaped DNA origami tiles designed to form a crystalline 2D array by sticky end cohesion. Image adapted from [28]. (b) Surface assisted stacking of DNA origami tiles of different shapes: a sharp triangle, a DNA rod and cross-shaped tiles shown in (a). Image adapted from [29].

2.1.3 DNA origami: applications

The DNA origami nanotechnology has provided a way to precisely manipulate objects in the nanometer scale, thus leading to interesting applications in different fields, such as molecular robotics, optics and nanomedicine, and allowing studies of the interactions of proteins and nucleid acids on a molecular level.

In the field of molecular engineering, for example, the DNA origami nanotechnology has been exploited to create dynamic robots such as molecular walkers and tweezers. In 2010, Seeman and his group reported a system that consisted of a tensegrity triangle walker and a DNA origami platform [30]. They provided the system with a track and stations with cargoes (gold nanoparticles) to load. Upon the addition of fuel (DNA strands), the tensegrity triangle walker would move along the track and load the intended cargoes at the stations. All movements were processed through strand displacement reactions (see Figure 2.5a). Catalytic reactions by enzymes can drive the DNA walker to move on the DNA origami platform as well.

In 2014, Castro and coworkers built a set of DNA origami robots that were capable of performing complex 1D, 2D and 3D motions, by combining linear displacements and rotations [31]. Their DNA origami joints (a hinge, a slider and a crank-slider, see Figure 2.5b-c) were incorporated into controllable mechanisms that were actuated in a reversible fashion using DNA strand inputs on minute timescales.

Another interesting application is the use of DNA origami structures to guide the organization of nanomaterials such as metal nanoparticles (NPs), quantum dots and carbon nanotubes with nanometer-scale precision. Yan and coworkers were the first to demonstrate that they could precisely control the number and position of nanoparticles on a discrete architecture: they used DNA origami to arrange gold nanoparticles in a linear fashion on a triangular DNA origami [32]. In a following work, they also proved encapsulation of AuNPs in a DNA origami cage [33]. The origami-nanoparticle architectures since then have been expanded and have been used to study new optical properties of plasmonic nanostructures, such as chiral plasmonics (when the metal nanostructure assembly is asymmetric) or plasmonic hotspots (when a fluorophere is placed at the specific local spot where the impinging electric field is highly enhanced). [4]. In fact, Mie and Prodan et al. predicted that metal nanoparticles can absorb light and that a plasmonic coupling between nanoparticles can occur if the distance between them is short enough (in general the edge-to-edge distance between NPs needs to be less than 2.5 times the particle diameter) [34] [35]. To experimentally achieve plasmonic coupling, DNA origami structures can be profitably used as platforms to place the metal (gold or silver) NPs in a specific geometry.

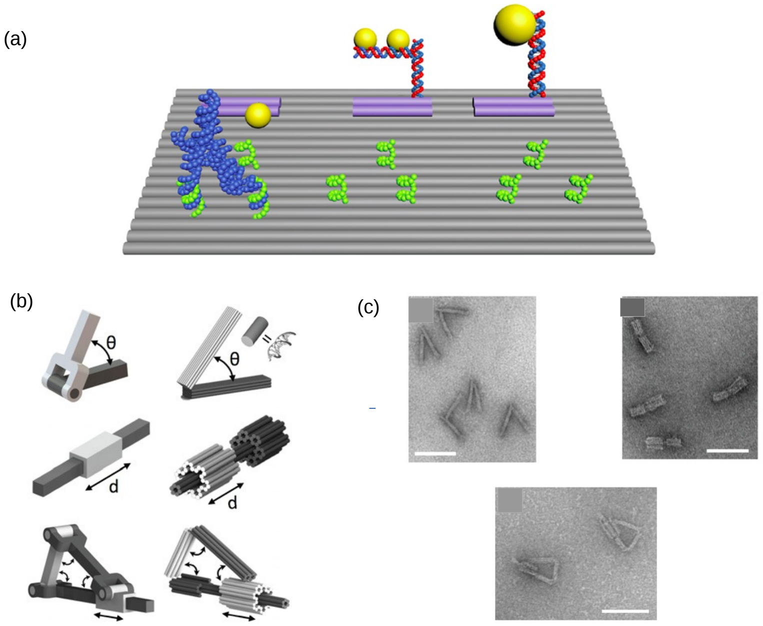

Figure 2.5: Examples of DNA origami structures with applications in molecular engineering. (a) The Seeman walker is a DNA triangle able to walk along tracks on DNA origami and to pick up a cargo at each station along an assembly line with DNA strand guidance [30]. (b) Schematic representation and (c) Transmission Electron Microscopy (TEM) images of the reconfigurable DNA origami devices designed by Castro et al. and able to combine linear and rotational motion [31].

Moreover, applications that address basic problems in biophysics have emerged. DNA structures can serve as tools for determining the functions of proteins - as in the before-mentioned work of Iwaki et al. [7] - or of proteins structures, as originally proposed by Seeman. Cryo-electron microscopy has indeed emerged as a powerful method for determining protein structures to near-atomic resolution, even without crystallization, but it is still difficult to determine the structure of proteins that are smaller than 200 kDa, because it is difficult to identify the individual protein particles from the background noise in the electron transmission images. The problem may be overcome if the proteins are tethered to a DNA origami structure because the DNA origami particle has a relatively large size and known structure and thus serve as an index to help locate the much smaller protein molecules[4].

Regarding the applications in nanomedicine, DNA origami is considered one of the most promising technology for drug delivery, because of its biocompatibility, minimal cytotoxicity and programmability for targeted and controlled release. For example, Ding and co-workers published an article on the use of variously shaped DNA origami structures that could kill cancer cells via the transportation of doxorubicin, a chemotherapy drug that intercalates DNA to inhibit cell biosynthesis, inside those cells [36].

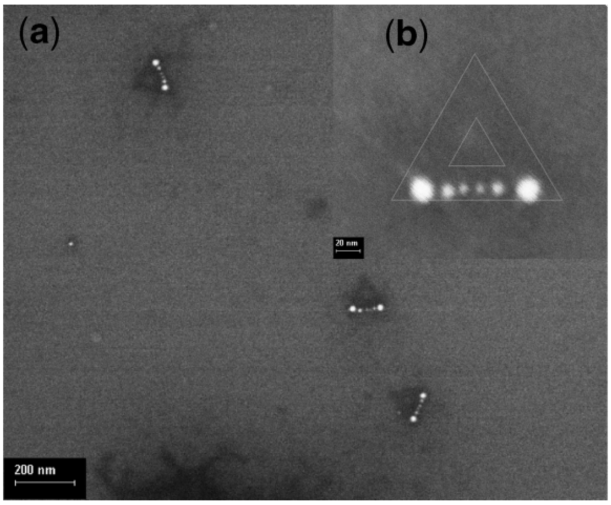

Figure 2.6: (a) Scanning Electron Microscopy (SEM) images of the six-AuNPs linear structures organized by triangular DNA origami created by Yan and his group [32]. The triangular shape of the DNA origami templates is visible as darker color. (b) Zoom-in image of one assembled origami-AuNP structure.

2.2 The DNA molecule

In the following paragraphs, I will briefly summarize the fundamental chemical and physical properties of the DNA molecule that were useful for the sample preparation and the experimental applications of the DNA origami nanotechnology.

2.2.1 The DNA structure

DNA is a central molecule in biology, as it stores and transmits genetic information from one generation to another and is hence essential for the development and function of life. The structure of DNA was presented by J. D. Watson and F. H. C. Crick in 1953 in their paper *Molecular structure of nucleid acids* [37], based also on the experimental work of M. H. F. Wilkins and R. E. Franklin.

The DNA molecule is a polymer whose repeating unit - called nucleotide - is composed of three elements: a monosaccharide deoxyribose sugar, a phosphate group and a nucleobase (see Figure 2.7). There are four different nucleobases: adenine (A), guanine (G), cytosine (C) and thymine (T). A and G are made of one hexagon linked to a pentagon ring and are called purines, while C and T only include one hexagon and are named pyrimidines. Because the electrons in the five- and six-membered rings are not localized, each base has a planar shape with a thickness of 0.34 nm.

Monophosphate nucleotides can bind to each other by linking the phosphate to the 3′ carbon of another nucleotide deoxyribose ring, thus making long polymers that are called polynucleotides or single-stranded DNA (ssDNA). A direction can be assigned to a ssDNA molecule due to the asymmetric phosphodiester bond between the two adjacent deoxyribose rings. One end of the ssDNA molecule terminates with a phosphate group at the 5′ carbon (the 5′-end), while the opposite end terminates with a hydroxyl group at the 3′ carbon (the 3′-end). Enzymes are sensitive to the directionality of the filament and usually process DNA from the 5′-end to the 3′-end. The double-stranded DNA (dsDNA) molecule is made of two antiparallel helical chains each coiled round the same axis. The two chains are related by a dyad perpendicular to the fibre axis. Both chains follow right-handed helices, but owing to the dyad the sequences of the atoms in the two chains run in opposite directions. The bases are on the inside of the helix and the phosphate on the outside (see Figure 2.8).

There is a residue on each chain every 0.34 nm in the $z-$direction and, since the angle between adjacent residues in the same chain is $\theta = 36°$, the structure repeats after 10 bases on each chain. As the phosphates are on the outside, cations have easy access to them. The two chains are held together by specific hydrogen bonds between the purine and the pyrimidine bases, *i. e.* bonds between adenine and thymine and between guanine and cytosine. The planes of the bases are perpendicular to the fibre axis, therefore the $\pi-$orbitals of the aromatic ring of one base overlap with the $\pi-$orbitals of the aromatic ring of adjacent base. The alignment of the aromatic rings - called stacking - has the role to expel water from the space between the nucleobases and stabilizes the double helix.

Under physiological conditions, the DNA double helix usually adopts the right-handed B-form, characterized by grooves of different length (a major groove and a minor groove) and a diameter of 2 nm. Under special buffer conditions, the dsDNA molecule also exhibits the A-form (right-handed, characterized by a diameter of 2.3 nm and a helix pitch of 11 bp) and the Z-form (left-handed, with 12 bp per turn and a diameter of 1.8 nm).

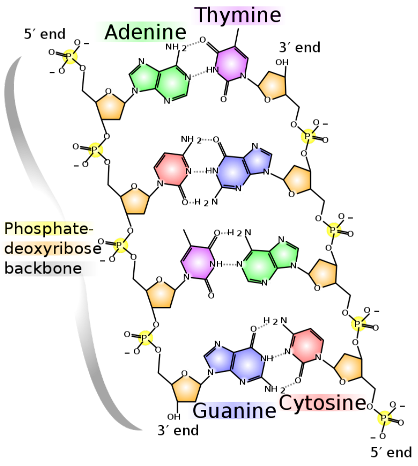

Figure 2.7: Schematic illustration of the molecular structure of the dsDNA: Adenine pairs with Thymine through two hydrogen bonds, while Guanine pairs with Cytosine through three hydrogen bonds; the DNA backbone consists of the phosphate group and the sugar molecule.

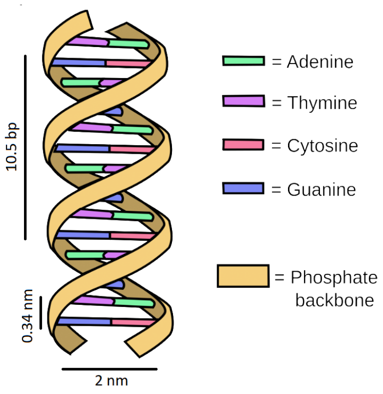

Figure 2.8: Schematic illustration of the double-helix structure of dsDNA. The two sugar-phosphate backbones twist about on the outside with the flat hydrogen-bonded base pairs forming the core. The characteristic distances in the dsDNA structure are also indicated.

2.2.2 Chemical properties of DNA

The four nucleotides A, T, G and C, have an absorption peak at a wavelength $\lambda = 260\,\text{nm}$. The total absorbance of a ssDNA strand depends on the sum of the absorbance of the single nucleotides plus the effect of the interactions between the nucleotides. This means that a single strand absorbs less than the sum of its nucleotides and a double strand less than the sum of its two-component single strands.

The optical properties of the dsDNA are used to estimate the concentration of DNA origami in solution. By measuring the amount of ultraviolet radiation absorbed by the DNA nanostructures with a spectrophotometer and by exploiting the fact that for a 1 cm pathlength, the optical density at 260 nm (OD260) of a $50\,\mu\text{g}\,\text{mL}^{-1}$ solution of dsDNA equals 1, the mass of DNA per unit of volume can be determined. By assuming that the absorption is completely due to the dsDNA nanostructures - whose length and mass correspond to those of the DNA origami scaffold - it is finally possible to determine the molar concentration of DNA origami nanostructures.

In pH physiological conditions the phosphates groups of the dsDNA present a localized negatively charge on the free oxygen that makes the single filament a negative charged polyelectrolyte. The distribution of associated ions can be approximated by the Debye-Huckel theory. The discretely charged polymer is idealized as a chain with linear charge density and two layers of ions around the DNA strand can be identified. The first one consists of a stratum of condensed counterions that are free to translate along the fibre axis but that remain within a short distance d with respect to the filament. In water at room temperature $d = 7\,\text{Å}$. The second layer is made up of weakly interacting anions and cations.

The negative charge on dsDNA is largely exploited in gel electrophoresis analysis, as will be described in chapter 3.

2.2.3 Mechanical properties of ssDNA: the freely-jointed chain model

The elasticity in tension of the ssDNA molecule can be described with the freely-jointed chain (FJC) model [71], [39]. This model approximates the polymer as a chain of infinitely rigid segments of length l_K - the Kuhn length - with completely free joints; segments do not have thickness, mass or charge, and are free to pass through each other.

The response of a FJC of N segments of length l_K and contour length $L_0 = Nl_K$ to an external force can be calculated with the Linear response theory. In the low-force regime ($f \to 0$), the theory predicts that

$$\langle x \rangle = \frac{\langle x^2 \rangle_{f=0} f}{k_B T}. \tag{2.1}$$

A self-crossing FJC can be described with the random walk model, hence its fluctuations at null force are:

$$\langle x^2 \rangle_{f=0} = \langle R^2 \rangle / 3 = N l_K^2 / 3. \tag{2.2}$$

By combining equations 2.1 and 2.2, it is possible to write the polymer extension as a function of the external force:

$$\langle x \rangle = \frac{N l_K^2}{3 k_B T} f, \tag{2.3}$$

thus obtaining the classic *entropic spring* result: the ssDNA is hence modelled as a purely entropic system which resists elongation due to an external force to maximize the number of accessible microstates.

The *entropic spring* model works under the fundamental assumption of the Linear Response theory that $f \to 0$, *i.e.* when the force is not large enough to align individual Kuhn segments against thermal fluctuations ($f l_K << k_B T$). Since the Kuhn length of ssDNA is $l_K \approx 1.5\,\text{nm}$, the force needs to be $f < 4pN$ to allow a description as a random coil. For dsDNA $l_K \approx 100\,\mathrm{nm}$, so the low force limit is applicable only for $f < 0.04\,\mathrm{pN}$, which is well below the force regime that can be accessed with most single-molecule manipulation instruments.

The high force regime of the FJC model can be computed by considering that in a polymer of N independent monomers with orientation $\mathbf{l}$, the energy of a single monomer with applied force $\mathbf{f}$ is $\epsilon = -\mathbf{l} \cdot \mathbf{f} = -fl\cos\theta$. By calculating the partition function, the relation between the two conjugate thermodynamic variables f and $\langle x \rangle$ can be obtained. The analytical dependence of the extension on the force for the FJC is then given by the Langevin function:

$$\langle x(F) \rangle = L_0 \left[\coth\left(\frac{fl_K}{k_B T} \right) - \frac{k_B T}{fl_K} \right]. \tag{2.4}$$

2.2.4 Mechanical properties of dsDNA: the worm-like chain model

The worm-like chain (WLC) model is the standard physical model for semiflexible polymers and allows interpreting single-molecule experiments on a wide range of biological filaments, such as dsDNA, chromatin and muscular fibres [40]. The WLC model treats the polymer as an isotropic rod that is can be thermally bent, but not sheared, stretched or twisted, and is characterized by the persistence length l_P. The persistence length is the characteristic distance along the WLC over which the tangent vector correlations between two points at distance l decay as $1/e$:

$$\langle \mathbf{t}(l) \cdot \mathbf{t}(0) \rangle = \exp -(l/l_P). \tag{2.5}$$

The energy E of a stretched DNA molecule is given in the WLC by a line integral of two terms: the first one describes the resistance of the chain to bending; the second one gives the stretching energy resulting from the application of a force f to the end of the molecular chain. The expression of E is then [59]:

$$E = \int_0^{L_0} dl \left(\frac{k_B T l_P}{2} \left| \frac{d\mathbf{t}(l)}{ds} \right|^2 - f\cos\theta(l) \right). \tag{2.6}$$

The partition function of the WLC Z_{WLC} is then given by:

$$Z_{WLC}(L_0, f, \mathbf{t}_0, \mathbf{t}_1) = \int d\mathbf{t} \exp -E_{WLC}/k_B T = \langle \mathbf{t}_1 \left| \exp -(L_0/L_p) E_{WLC} \right| \mathbf{t}_1 \rangle, \tag{2.7}$$

where $d\mathbf{t}$ is the integration measure in functional space of the paths drawn on the unit sphere starting at the point $\mathbf{t}_0 = \mathbf{t}(l = 0)$ and ending at $\mathbf{t}_1 = \mathbf{t}(l = L_0)$.

The relation between the two conjugate thermodynamical variables (the extension $\langle x \rangle$ and the force f) can be written in terms of the partition function as:

$$\langle x \rangle = k_B T \frac{\partial ln Z_{WLC}}{\partial f}. \tag{2.8}$$

Equation 2.8 needs to be solved numerically. An analytical interpolation of the force-extension points obtained by computer calculations has been proposed by Marko and Siggia [41] and is equal to:

$$f = \frac{k_B T}{l_P} \left[\frac{1}{4(1 - x/l_0)^2} - \frac{1}{4} + \frac{x}{l_0} \right]. \tag{2.9}$$

This formula is a useful approximation to the WLC model and reduces to the exact solution as either $\langle x \rangle \to 0$ and $\langle x \rangle \to L_0$. In between, it reproduces the general behaviour of the exact solution with a relative error of approximately 10 %.

Some deviations from the Marko-Siggia formula are observed in experimental data at high forces, where the dsDNA polymer gets longer than the prediction (stretch deformation). In fact, in the high-force regime, the quadratic energy assumption breaks down: this happens when the energy per unit length deriving from the applied force approaches the stacking energy per unit length. Since the stacking bonds have an energy $\epsilon = 2 - 3\, k_B\, T$ per base-pair, *i.e* $\epsilon \approx 40\,\mathrm{pN}$. Indeed, stretching at force $f > 40\,\mathrm{pN}$ leads to a sudden increase in DNA length (overstretching transition).

Chapter 3

Design, synthesis and characterization of a 4-helix bundle DNA origami

3.1 Design of DNA origami structures with *cadnano*

DNA origami structures can be designed by using *cadnano*, a specific software developed by W. Shih's laboratory at the Dana Farber Cancer Institute and released under the MIT license [43]. More recently, the development of *cadnano2* has been supported under the same open-source license by the Wyss Institute for Biologically Inspired Engineering at Harvard University. For the structures presented in this work, I used the *cadnano* version available online.
An example of the *cadnano* file for the design of a 4-helix bundle DNA origami is illustrated in Figure 3.1. On the left side, the origami nanostructure is shown from its top view and each helix is represented as a circle. On the right side, the 2-dimensional version of the lateral view of the DNA origami is displayed. The long blue line represents the circular scaffold; the short coloured lines are the staples, used to connect the different parts of the scaffold to build the structure. The numbers from 0 to 3 on the left label the four helices of the nanostructure, where each helix is made up of some oligos from the scaffold and some of the staples. The red crosses indicate bases that have been skipped to diminish the global twisting artificially introduced with the design and to equate it to the natural one. B-form double helices are indeed characterized by an average twist of 33.75° per base pair (bp), *i.e.* by a twist density of 10.5 bp/turn, while in the square-lattice structures, the initially imposed double-helical twist density is set as 10.67 bp/turn [44] [45]. The difference in twist density between the two configurations is then $\Delta\tau = 0.17$ bp/turn, which corresponds to 1 bp every 6 turns. Since it takes 63 bp to the B-form dsDNA to complete 6 turns and 64 bp to the 4-helix bundle with a square-lattice geometry, a simple way to equate the two twist densities is to remove a single base pair from all helices in a cross-section of the structure every 64 bp.

Once the DNA origami design is complete, the staple sequences - complementary to the corresponding regions of the scaffold - are calculated by *cadnano*. Staples typically supply the majority of crossovers that connect adjacent double-helical domains in DNA origami objects. Staples crossovers can be assigned between adjacent double-helical domains at all positions where the staple backbone orientations of the neighbouring double-helical domains coincide. Staples can undergo multiple crossovers and thus connect multiple double-helical domains, but they must obey specific constraints, *e.g.* their length should be $l \sim 24 - 32$bp to enable binding. In the case of the most common circular M13 phage scaffold the available length is 7249 nucleotides, but synthetic scaffolds with different length can be also used depending on the requirements.
The origami synthesis is accomplished by mixing the scaffold and 10× excess staples in a one-pot reaction and by subjecting the mixture to a thermal denaturation and annealing procedure [46]. The goal of the assembly reaction is to reach a minimum energy state at conditions where the minimum corresponds to the target structure. The commonly used buffer ($1\times$ TAE- Mg^{2+}) is made of 40 mM Tris, 20 mM acetic acid, 2 mM EDTA and 11 mM $MgCl_2$. The magnesium cations are essential to ensure the correct folding of multiple crossovers because they neutralize and stabilize the negatively-charged phosphodiesters by bridging them together.
In this work, I will describe the synthesis protocol, the imaging procedure and the analysis of different DNA origami structures. The first two structures presented in this chapter, a 4-helix

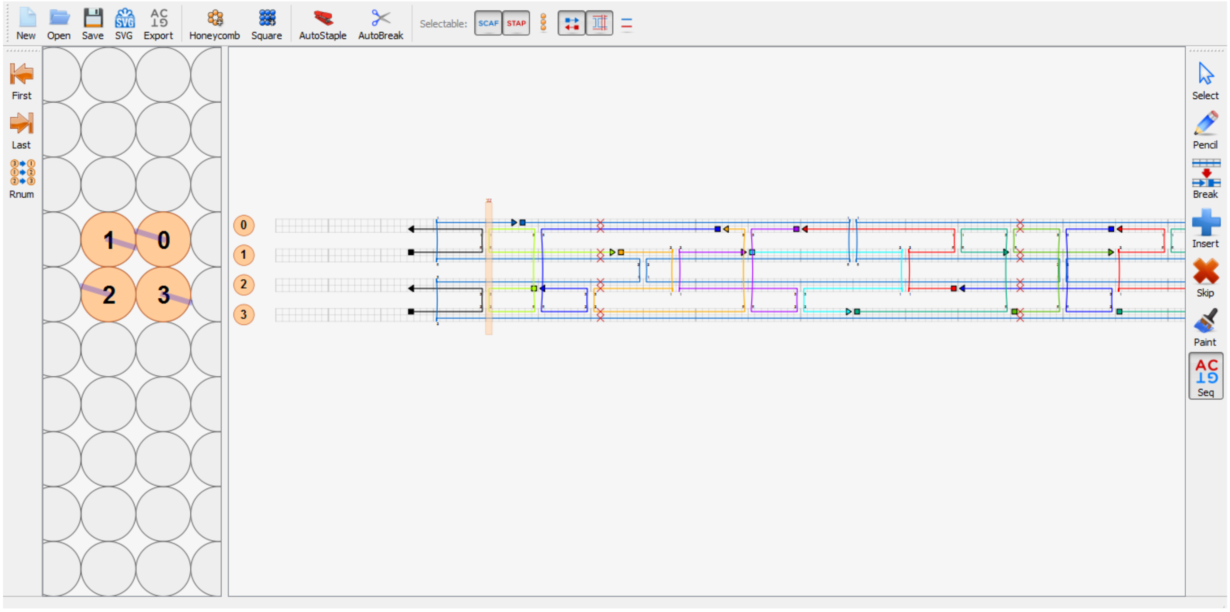

Figure 3.1: Example of the *cadnano* of a 4-helix bundle DNA origami.

bundle and a 4-helix bundle folded from a linearized scaffold and characterized by a single-stranded region, were then measured with the magnetic tweezer, as the main interest was the study of their mechanical properties. The other origami structures, a force clamp nanodevice and a sliding DNA origami, described respectively in Chapters 5 and 7, have a more complex design that allowed us to study forces and motion at the nanoscale.

Before describing in details the design and the synthesis protocols of the different DNA origami nanostructures used in our work, I will introduce the basic principles of Transmission Electron Microscopy (TEM). TEM imaging represents indeed the most common method for characterizing DNA origami samples.

3.2 TEM imaging of DNA origami nanostructures

Transmission Electron Microscopy (TEM) is a widely established tool for atomic resolution studies of nano-structured objects. In particular, single-particle TEM experiments are suited for determining the morphology and the structural properties of nano-materials composed of light elements, such as those of pharmaceutical and biological interest.

In a transmission electron microscope, an electron beam characterized by an energy between 50 and 200 keV is focused onto a specimen. The electrons pass through the sample and are scattered in different directions depending on the internal structure of the object of interest; they are then collected and magnified with electromagnetic lenses and finally recorded on a fluorescent screen or a charge-couple device (CCD). The specimen, with a thickness ranging from few to hundred nanometers, lays on a specific carbon-coated TEM grid. In general, samples for TEM imaging need to be stable under vacuum, so they are traditionally prepared in the solid state. The water content of biological sample (cells, matrix, or proteins) requires particular strategies for TEM visualization.

Materials with electron densities that are significantly higher than amorphous carbon are easily imaged. These materials include most metals (e.g. silver, gold, copper, aluminum) characterized by heavier atoms which scatter more electrons and therefore have a smaller electron mean free path than lighter atoms. On the contrary, biological materials, which essentially consist of H, C and O atoms with low atomic numbers, are characterized by a poor contrast with respect to

the carbon layer of the TEM grid and they are difficult to image. To increase the contrast of the biomolecules, uranyl acetate and uranyl formate staining are commonly used.
TEM imaging has been largely used for the characterization of DNA origami and of gold nanoparticles-modified origami structures. For these samples, copper grids covered with a thin carbon layer are activated with a plasma cleaning treatment for 5 min at 20 W. A drop of origami solution is then deposited on the surface and after 5 min it is removed with absorbent paper and stained with a uranyl formate solution. When it is completely dried, it is ready to be imaged with the TEM. Several representative TEM images are shown in the following sections (see for instance Figure 3.5).

3.3 A 4-helix bundle DNA origami for mechanical measurements on a target biomolecule

In a typical single-molecule mechanical assay, the molecule of interest is attached to the probe through molecular linkers such as dsDNA, to avoid non-specific interactions with the surface of the probe. The mechanical stiffness of those linkers is critical for the signal-to-noise ratio of the measurement. In their work of 2013 [55], Pfitzer et al. showed that DNA helix bundles can be profitably used as linker system for single-molecule mechanical assays, since they enable single-molecule force spectroscopy with higher resolution in the low force regime. In particular they constructed a 10-helix bundle DNA origami linker and they employed it to study the dynamics of a 20 base-pair (bp) long DNA hairpin in an optical tweezer setup characterized by two trapped beads.
We did realize a similar configuration in which a 4-helix bundle DNA origami was used as a tether to study the dynamics of a 24 bp long DNA hairpin in a magnetic tweezer configuration. To this purpose, we first designed a 685 nm 4-helix bundle (4HB) DNA origami consisting of a 8064 nucleotide long scaffold and hundreds of short staples and we studied its mechanical properties. To support magnetic tweezer measurements, the two extremities of the 4HB were modified with digoxigenin and biotin molecules, to allow binding respectively to the anti-digoxigenin coated surface of the flow cell and to the 1 µm-diameter streptavidin coated magnetic beads. After characterizing the mechanical properties of the 4HB and measuring its stiffness, we designed a new 4HB DNA origami and we modified it in order to place a 24 bp hairpin - which is naturally present in the scaffold - in its centre. The circular scaffold used for the folding had been previously linearized by using restriction enzymes so that the final DNA origami structure was characterized by two 341 nm long 4HBs connected by a 24 bp long hairpin. The two extremities of the origami were again modified with digoxigenin and biotin molecules to support mechanical measurements, as illustrated in Figure 3.2. In this case, we used both 1 µm-diameter streptavidin coated magnetic beads and 2.8 µm-diameter streptavidin coated magnetic beads in order to apply the required forces.

3.3.1 Synthesis of the 4-helix bundle DNA origami

To fold the 4-helix bundle DNA origami, we set up the following folding reaction:

Reagent	**Final concentration**
Scaffold (p8064)	10 nM
Staples	100 nM
$MgCl_2$	16 mM
50× TAE	1×
H_2O	

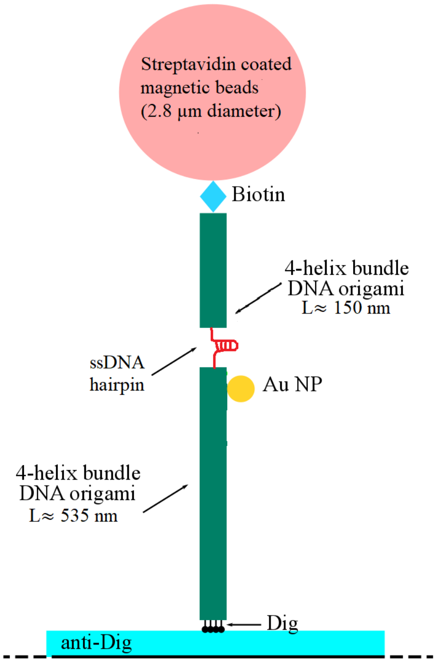

Figure 3.2: Schematic representation of the experimental configuration: a 4HB DNA origami is linked to the surface of the flow cell via the anti-Digoxigenin/Digoxigenin bond and to the magnetic bead via the Biotin/Streptavidin bond. The origami is composed of two 4HBs elements (respectively ≈150 nm and 535 nm long) linked with a ssDNA hairpin.

The 50× TAE buffer is made up of 2M Tris-Acetate and 50 mM EDTA.

Biotin-modified and digoxigenin-modified staples were used in order to allow binding of the structures respectively to the streptavidin-coated magnetic beads and to the anti-digoxigenin-passivated surface of the MT flow cell. The chemical structures of the modified dideoxynucleotide triphosphates (ddNTP) including biotin- and digoxigenin-labels are illustrated in Figure 3.3. Biotin-modified staples were provided by Eurofins. Digoxigenin-modified staples were obtained by exploiting an enzimatic technique that relies on DNA nucleotidylexotransferase (terminal transferase) to attach modified ddNTP to the 3'-end of an arbitrary subset of oligonucleotides to be incorporated at specific positions in the DNA origami. The use of dideoxynucleotides ensures that only a single modified nucleotide is attached [47].
Terminal transferase and digoxigenin-dideoxy-uridine-triphosphate (DIG-ddUTP) were purchased from Jena Bioscience. Under standard conditions, 100 pmol oligonucleotide in total and 1 nmol of modified ddNTP were mixed in 20 µL with the reaction buffer provided by Jena Bioscience and $CoCl_2$ (5 mM), and incubated with terminal transferase (20 units in 1 µL) for 15 min at 37 °C. The reaction was stopped by adding EDTA (20 mM final concentration). Strands used for subsequent origami formation were precipitated with NaOAc (0.3 M, pH=5.2) and 2.5 volumes of EtOH (−20 °C, 96%) for 15 min on dry ice, followed by centrifugation for 30 min at 20 000 g.The pellet was washed once with EtOH (−20 °C, 70%). Depending on the lenght of the oligonucleotides, up to 90% yield was obtained.

The solution for folding the origami was first heated up to 65 °C to denaturate the scaffold, then it progressively reached a final temperature of 25 °C in 16 h. Each step of this thermal ramp helps to overcome the energy barrier of the hybridization reaction between the scaffold and each staple, thus allowing the origami formation. To confirm the correct assembly of the origami, gel electrophoresis analysis and Transmission Electron Microscopy (TEM) characterization were

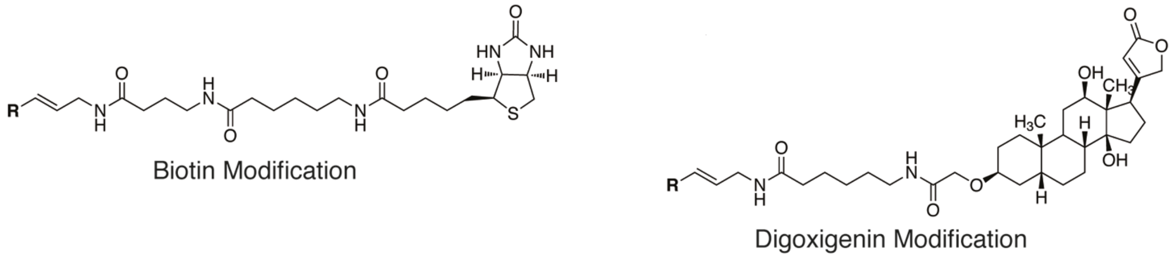
Biotin Modification
Digoxigenin Modification

Figure 3.3: Overview of the chemical structures of the modified dideoxynucleotide triphosphates including biotin- and digoxigenin-labels.

performed.
The magnesium screening test was carried on with a 1% agarose gel running at 75 V for 2 h 30 min. The optimal magnesium concentration is the maximum concentration at which the origami can fold without aggregating. In Figure 3.4), it is possible to see that for a $MgCl_2$ concentration higher than 16 mM, the sample migration is slower, thus indicating clustering. This value has then been used for folding the 4HBs.

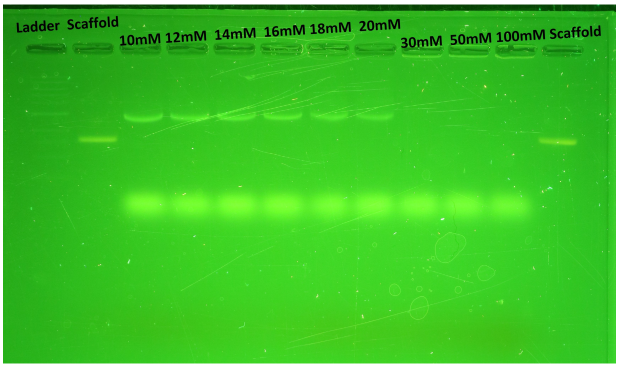

Figure 3.4: Gel electrophoresis analysis to check correct assembly of the origami at different magnesium concentrations. Thin lanes correspond to correctly folded origami. Broad lanes correspond to excess staples or unfolded origami.

The 4HB DNA origami were purified from excess staples by centrifugation for 5 times with Amicon filters (Amicon Utra 0.5 mL 100 kDa (Millipore, Massachusetts) at 8000 g for 10 min. The purified sample (typical concentration of 1 nM) was then absorbed for 2 min on a copper grid (TedPella Inc.) previously treated with oxygen plasma. The sample was then washed to remove salt crystals and stained for 1 min with a Uranyl Formate solution for TEM characterization. A representative TEM image of the 4HBs is illustrated in Figure 3.5.

3.3.2 Synthesis of the 4-helix bundle DNA origami with a 20 nm Au nanoparticle

We slightly modified the previous design of the 4HB DNA origami to include handles for binding ssDNA functionalized Au nanoparticles (AuNPs). 20 nm AuNPs were previously functionalized with short DNA strands according to the 'Freeze and Thaw method' [58]. This procedure exploits the concentrating effect of freezing and the steric stabilization of biopolymers to attach thiolated ssDNA oligos to AuNPs; compared to previous functionalization methods (*e. g.* salt aging), it is faster and it assures a higher DNA loading density. 20 nm AuNPs from stock solution were incubated with excess of thiolated oligos and frozen at −20 °C for 2 h. The DNA/AuNP

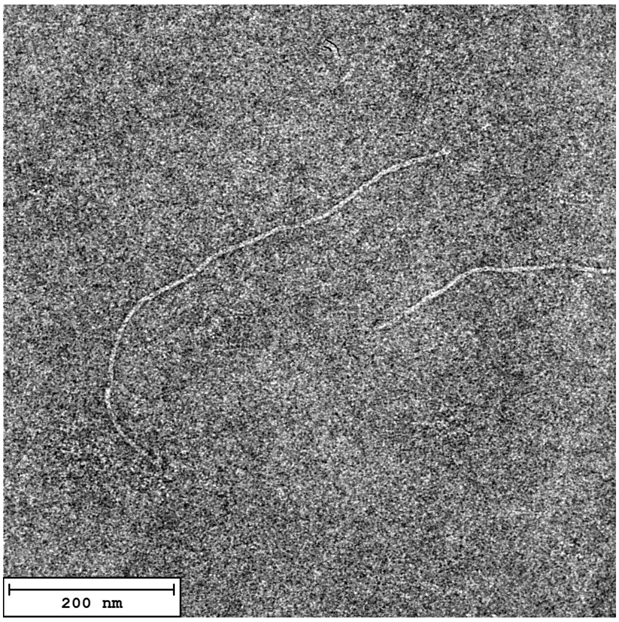

Figure 3.5: A 4HB DNA origami imaged with TEM at 80 kV. The 4HB DNA origami were previously stained with Uranyl Formate.

conjugates solution was then left to unfreeze in the sonicator at room temperature and concentrated by centrifugation with 100 kDa Amicon filters. It was purified from excess oligos with gel electrophoresis: when loaded in a 1.5 % agarose gel, functionalized AuNPs run at different speed with respect to ssDNA oligos. The AuNPs band is easily recognizable for its red color: it can be then cut and squeezed to extract DNA/AuNPs conjugates. Finally, the so-prepared solution was concentrated and incubated with the origami overnight at room temperature in a ratio of 20: 1 for the AuNPs with respect to the 4HBs. After a further gel electrophoresis purification step to remove excess AuNPs, TEM analysis was performed to check correct binding of the 20 nm AuNPs to the 4HB structures (see Figure 3.6). Before imaging, samples were stained with Uranyl Formate.

3.3.3 Determination of the persistence length of the 4-helix bundle DNA origami

The persistence length l_P is a basic mechanical property of polymers: it provides a measure of the distance along which the polymer's direction persists before changing its course and it is formally defined as the length over which the angular correlation in the tangent direction decreases by e times. There are two main methods to calculate the persistence length, based on the tangent-tangent correlation function and on the mean squared end-to-end distance.

The first approach [62] shows that the correlation between the tangent vectors to two points separated by a distance l is equal to the cosine of the angle defined by those vectors, averaged over all the points at the fixed distance l. The tangent-tangent correlation function for a 3D object decays exponentially as $\frac{1}{l_P}$:

$$\langle \mathbf{t}(l) \cdot \mathbf{t}(0) \rangle = \langle \cos(\theta(l)) \rangle = e^{-\frac{l}{l_P}} \tag{3.1}$$

In the second method, the mean squared end-to-end distance is related to the persistence length *via* the following relation:

$$\langle R^2 \rangle = 2l_P l + 2l_P^2 (e^{-\frac{l}{l_P}} - 1), \tag{3.2}$$

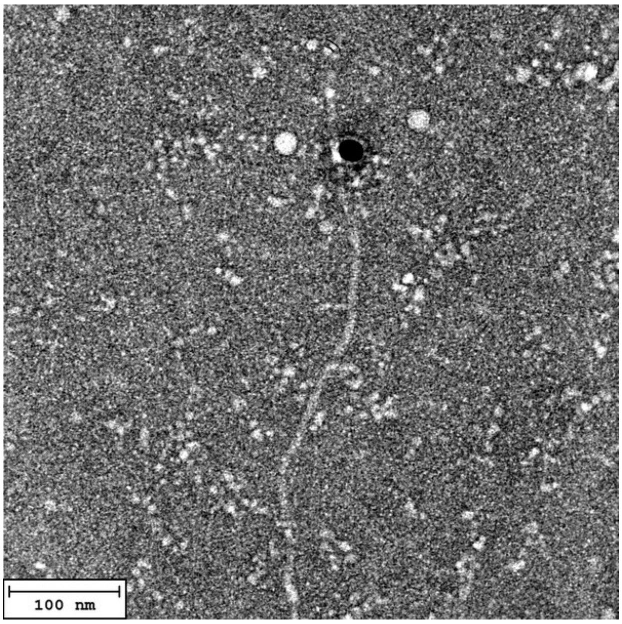

Figure 3.6: TEM image of a 4HB DNA origami decorated with a 20 nm AuNP. The 4HB DNA origami were previously stained with Uranyl Formate.

where l is the distance between two points of the 3D polymer.
To calculate the persistence length of the 4HB DNA origami, we analyzed several TEM images of the polymers by using the software FiberApp [65]. With the FiberApp script, it was possible to fit the profiles of the 4HBs - as illustrated in Figure 3.7 - and get the coordinates of the "monomers" forming the structures. We then used the xy positions to calculate the tangent-tangent correlation function and the mean squared end-to-end distance of each polymer and we fit the data respectively with the following formulas, that refer to a two-dimensional polymer:

$$\langle \cos(\theta(l)) \rangle = e^{-\frac{l}{2l_P}} \tag{3.3}$$

and

$$\langle R^2 \rangle = 4l_P l + 4l_P^2 (e^{-\frac{l}{2l_P}} - 1), \tag{3.4}$$

Equations 3.3 and 3.4 differ by a factor 2 with respect to equations 3.1 and 3.2 to take into account the dimensionality of the problem.

Two representative fits - relative to the 4HBs in Figure 3.7 - are displayed in Figures 3.8 and 3.9.

The analysis was repeated for different bundles. By applying the tangent-tangent correlation method, we got an average persistence length of $\langle l_P \rangle = 471 \pm 49$ nm; with the mean squared end-to-end distance the obtained value was $\langle l_P \rangle = 499 \pm 45$ nm.
In conclusion, the value for the persistence length calculated with optical methods is $\langle l_P \rangle = 485 \pm 66$ nm, which is consistent with other values reported in the literature for similar 4-helix bundles and 6-helix bundles [24] [66].

The theoretical value of the persistence length of a biopolymer can be calculated on the basis of its bending stiffness $B = EI$ with the following equation [68]:

$$l_P = \frac{EI}{k_B T}, \tag{3.5}$$

where E is the elastic modulus, I is the second area moment of inertia and $k_B T$ is the thermal

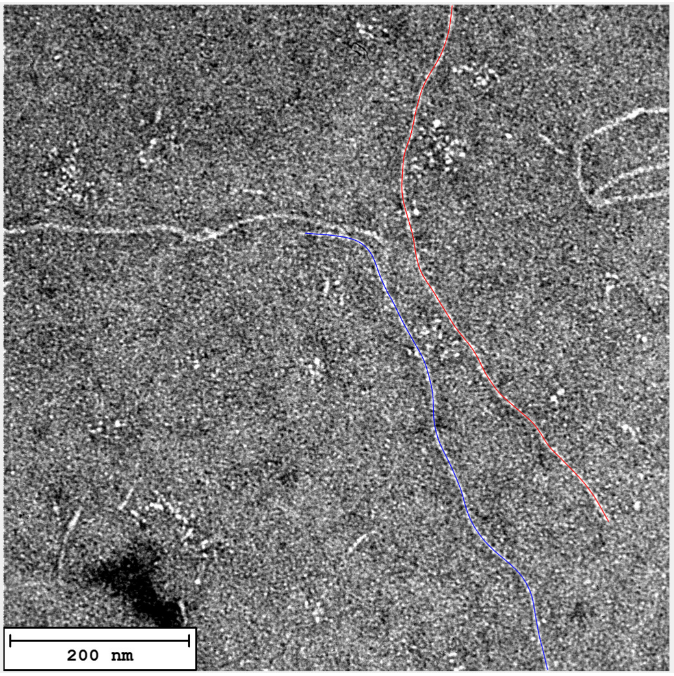

Figure 3.7: 4HB DNA origami imaged with TEM at 80 kV after staining with Uranyl Formate. The image has been analyzed with FiberApp.

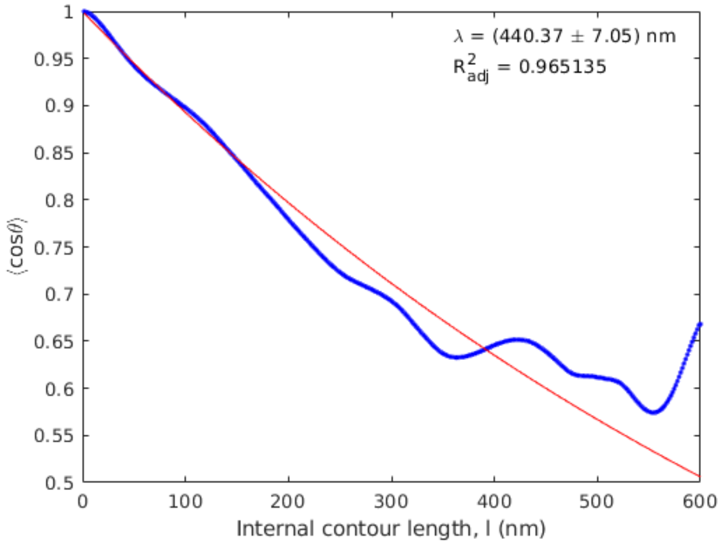

Figure 3.8: Fit of the tangent-tangent correlation function calculated for the 4HBs shown in Figure 3.7. The value obtained for the persistence length is indicated at the top of the plot.

energy at room temperature. For a 4-helix bundle with a cross-section as the one represented in Figure 3.10, the second area moment of inertia is given by:

$$I = \sum_{i=1}^{4}(I_{dsDNA} + \pi r^2 d_i^2) = 5\pi r^2 d^2, \tag{3.6}$$

where $r = 1\,\text{nm}$ is the radius of a dsDNA helix and $d = 1\,\text{nm}$ is the distance from the centroid of the i-th helix to the neutral bending axis - in this case, the axis passing through the centre of symmetry of the structure. By assuming that the elastic modulus is $E = 261\,\text{MPa}$, the resulting

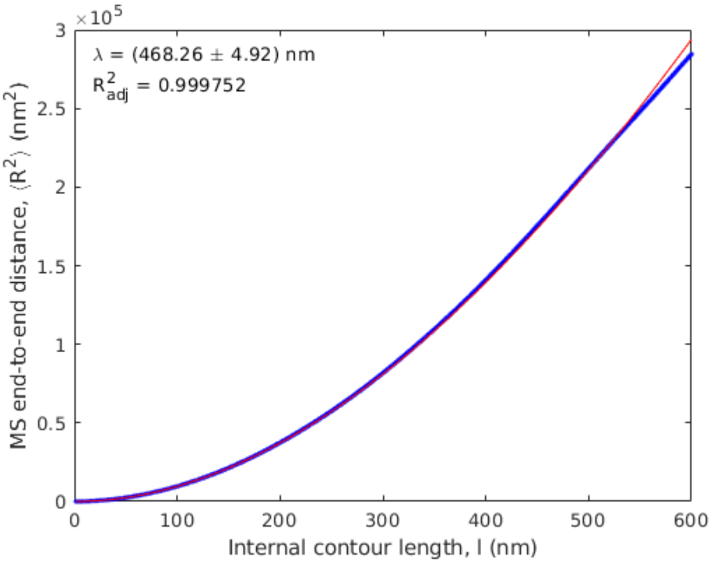

Figure 3.9: Fit of the mean squared end-to-end distance calculated for the 4HBs shown in Figure 3.7. The value obtained for the persistence length is indicated at the top of the plot.

persistence length is $l_P = 1\,\mu\text{m}$. This value gives an upper limit of the persistence length for a 4-helix bundle, but it does not take into account the fact that the cross-overs between the DNA origami helices do not assure complete immobility of the structure and the helices can then slide over each other. Moreover, the purification protocol slightly damages the structures. For these reasons, it is reasonable that the experimental value of the persistence length is smaller then the theoretical one.

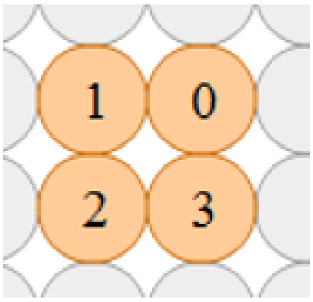

Figure 3.10: Cross-section of a 4-helix bundle DNA origami, obtained with the software *cadnano*.

Since our analysis confirmed that the 4HB DNA origami nanostructures are much stiffer then the dsDNA filaments, we expected them to be good tethers for target biomolecules in MT experiments and to reduce the noise in the measurements. We investigated further the mechanical properties of the 4HBs by recording force-extension curves of these polymers, as it will be discussed in Chapter 4.

3.4 Design and synthesis of the 4-helix bundle DNA origami with a ssDNA hairpin

As described in the previous chapter, the scaffolds used for DNA origami folding are variants of bacteriophage M13mp18 genomic DNA. The circular scaffold p8064 employed for the synthesis of the 4HB is naturally characterized by secondary structures stabilized by hydrogen bonds between complementary bases.

We modified the previous design of the 4HB so that a 24 bp long ssDNA hairpin (see Figure 3.11), freely forming in the scaffold, was placed in the centre of the origami structure. The staples in proximity to the hairpin were not added to the folding reaction so that this single-stranded region could form its natural secondary structure. By assuming a distance between two consecutive bases in a ssDNA filament of 0.5 nm [59], [60], the resulting difference in length between the folded and the unfolded state of the hairpin was $\Delta z = 24$ nm, a variation detectable with the magnetic tweezer experiments.

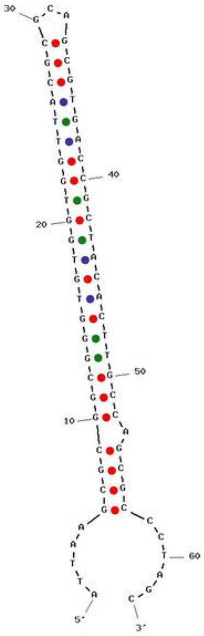

Figure 3.11: A 24 bp long ssDNA hairpin present in the scaffold.

The scaffold used for the folding of the modified 4HB was preliminarily linearized by using the restriction enzyme BglII, to form a final structure made up of two 4HBs elements (respectively ≈150 nm and 535 nm long) connected with a single hairpin. In fact, as already specified, DNA origami are folded out of a circular filament. If a single secondary structure is required, the scaffold needs to be linear and the design has to be adapted so that the region of interest does not include crossovers with other parts of the nanostructure. A detail of the *cadnano* file of the 4HB with the hairpin is shown in Figure 3.12.

Restriction enzymes recognize short DNA sequences and cut double-stranded DNA at specific sites within or adjacent to the recognition sequence; cleavage is accomplished simply by incubating the enzyme with the DNA in appropriate reaction conditions [70]. The scaffold was thus first incubated with the oligonucleotide complementary to the sequence to be cleaved at 65 °C for 1 h to obtain a double-stranded region. The restriction enzyme BglII (New England Biolab) was then added to the scaffold and left in incubation at 37 °C for 30 min to let the cutting process take place. The so-linearized scaffold was finally included in the synthesis reaction together with the staples in TAE buffer with 20 mM $MgCl_2$. The samples were purified from residual enzymes and excess staples by Amicon filtering and imaged with TEM to assess correct folding (see Figure 3.13).

Before setting up the folding for the 4HB DNA origami with the linearized scaffold, a preliminary test had been done to optimize the reaction conditions for the digestion of dsDNA with

Figure 3.12: Detail of the *cadnano* file for the design of the 4HB with the hairpin. The region of the scaffold (coloured in light blue) naturally forming the hairpin is indicated with an arrow. The part scaffold in front of the hairpin needs to be cleaved so that only a single DNA hairpin will form. To this purpose, the scaffold used for the synthesis of the structure has to be preliminarily linearized.

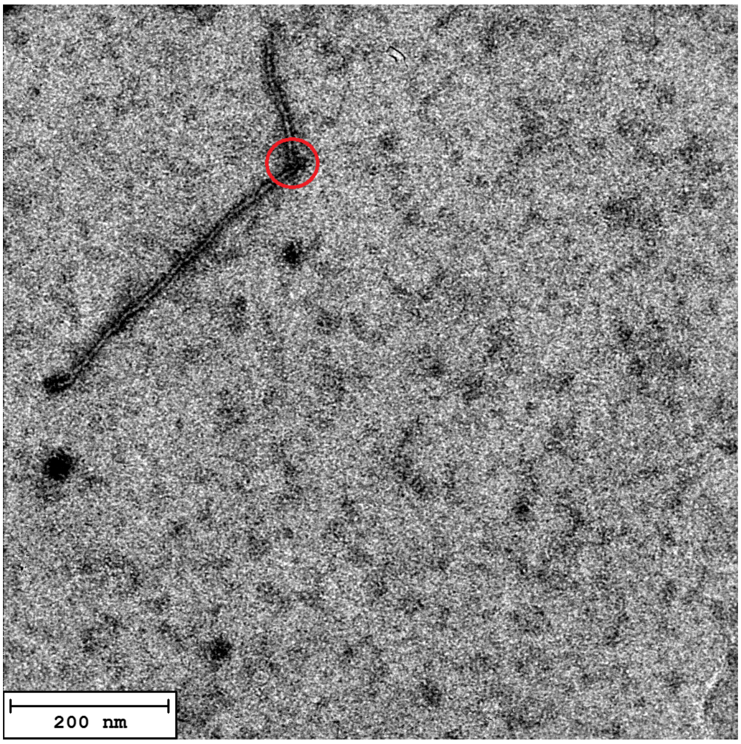

Figure 3.13: TEM image of a 4HB DNA origami folded out of a linearized scaffold. The 4HB DNA origami were previously stained with Uranyl Formate. The nick (marked in red) that is visible at the centre is due to the presence of the single-stranded region that leads to hairpin formation.

restriction enzymes. The p8064 scaffold had been incubated at 65 °C for 1 h with 10× excess of two oligonucleotides complementary to the recognition sequences respectively of BglII and BamHI endonucleases. After adding restriction enzymes (1 unit of each enzyme to 1 µg of DNA) in the appropriate buffer (NEB 3.1), the reaction mixture was incubated again at 37 °C for 60 min to let BglII and BamHI cleave the DNA. Heat inactivation was not required with these particular enzymes. Electrophoresis analysis was then performed to confirm that cutting had actually occurred (see the 1.2 % agarose gel shown in Figure 3.14). In fact, if a single restriction enzyme is added to the scaffold, only one band appears in the gel and the sample migrates with the same speed as the circular scaffold, because they are characterized by the same number of nucleotides. On the other hand, if both BglII and BamHI are added to the solution, the scaffold is cleaved at two positions and the two resulting filaments -having different lengths- run at different speeds. In particular, by using restriction enzymes BglII and BamHI, the scaffold is divided into two segments whose lengths are respectively 500 bp and 1500 bp. By repeating electrophoresis analysis, we observed the formation of two bands in the gel. We compared the positions of the gel lanes with the 1 kb ladder to check if the dimensions of the resulting segments were compatible with theoretical predictions and we concluded that the addition of BglII was effectively cleaving the scaffold at the desired position.

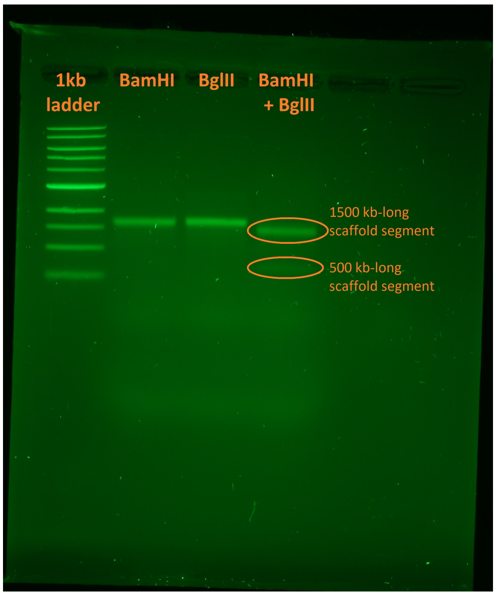

Figure 3.14: Gel electrophoresis test on digestion of p8064 scaffold with restriction enzymes BglII and BamHI. Thin lanes correspond to correctly folded origami.

3.5 Relevant results

In conclusion, we were able to design and synthesize a 4HB DNA origami having the required length ($\approx 685\,\mathrm{nm}$) to allow further magnetic tweezer measurements. Correct folding was assessed by gel electrophoresis analysis and TEM imaging.

We attached a 20 nm AuNP to the 4HB origami for further measurements in surface plasmon resonance conditions.

Finally, we designed and synthesized a new 4HB DNA origami characterized by the same configuration of the staples as the previous one - in order to assure the same stability - but modified in order to include a region with a single ssDNA hairpin. The ssDNA hairpin represented the target molecule for our magnetic tweezer experiments.

Chapter 4

Magnetic tweezer measurements on DNA origami nanostructures

4.1 Single-molecule measurements with magnetic tweezers

Magnetic tweezer (MT) experiments are based on the manipulation of a single molecule tethered on one end to a glass surface and on the other to a superparamagnetic bead. The tethered molecule is stretched by subjecting the bead to a magnetic force using an externally applied magnetic field gradient. The bead is imaged in a microscope *via* video recording, and computer analysis of the image gives the bead's three-dimensional position, and thus the end-to-end extension of the target molecule [52]. Standard magnetic tweezers track the position of beads at an acquisition frequency of approximately 50-100 Hz and can resolve the position of a surface-melted bead along the $z-$axis to $\sim$ 1 nm.

In the following paragraphs, I will briefly explain the working principles of magnetic tweezing, by referring to the book *Handbook of Single-Molecule Biophysics* by P. Hinterdofer and A. Oijen. Then I will describe the experimental setup and I will present single-molecule MT experiments in which the samples are DNA origami nanostructures with a total length $L_C \approx 700$ nm and whose extremities have been suitably modified to bind the flow cell surface and the magnetic bead.

4.1.1 Magnetic tweezing principles

In MT experiments, the molecule of interest is tethered between a surface and a superparamagnetic bead and force is applied via an external magnetic field **B**. The upward stretching force **F** on the bead is given by

$$\mathbf{F} = \frac{1}{2}\nabla(\mathbf{m}\cdot\mathbf{B}), \tag{4.1}$$

where **m** is the induced magnetic moment of the bead. Nonetheless, the bead and the linked molecule experience an effectively constant **F** because the length scale of the motion of the tethered bead (typically micrometres) is small compared to the length scale of changes in the magnetic field **B** (typically millimetres). The force **F** can be decreased or increased by moving the permanent magnets either up or down as the local magnetic field gradient is decreased or increased, respectively. The resulting range of possibly applied forces is between 10 fN and 100 pN.

The external magnetic field induces a major component of the magnetic moment to align in the direction of **B** itself. Due to a slight anisotropy in the magnetization of the bead, a minor component of the magnetic moment, $\mathbf{m}_0$, is initially not aligned with **B** . This generates a torque Γ on the bead:

$$\Gamma = \mathbf{m}_0 \times \mathbf{B}. \tag{4.2}$$

By rotating the magnets, it is then possible to rotate the bead because the torque applied by the tethered biomolecule (for instance dsDNA) on the bead is negligible compared to the torque imposed by the magnetic field.

In the most common optical configuration, the bead is illuminated by parallel light placed above the flow cell and the magnet. The interference of the illuminating light with the light scattered by the bead produces concentric diffraction rings in the focal plane of the objective placed below the flow cell. The image of the diffraction pattern is recorded through an objective with a complementary metal-oxide-semiconductor (CMOS) camera and analyzed with a computer.

The magnetic force $\mathbf{F} = F\hat{z}$ is not the only force acting on the superparamagnetic bead; since it is linked to the surface *via* the sample, the bead also experiences the restoring force of the biomolecule. The total potential energy of the system E_P thus equals

$$E_P = E_{tether} + E_{magnet}, \tag{4.3}$$

where the E_{tether} is the mechanical energy stored in the tethering molecule - *e. g.* the energy of a worm-like chain for a dsDNA filament - and E_{magnet} is equal to Fh (h being the measured extension of the tether).
At the position of equilibrium $\mathbf{r}_0 = (0, 0, l)$, where l is the extension of the tether, all partial derivatives of the total potential energy are equal to zero. We can then write that

$$\frac{\partial E_P}{\partial z} = \frac{\partial E_{tether}}{\partial z} - F = 0, \tag{4.4}$$

resulting in $\frac{\partial E_{tether}}{\partial z} = F$.
The bead is constantly moved away from its equilibrium position by the thermal noise due to the Brownian motion, so large fluctuations in the directions orthogonal to the force are observed. In particular, in the direction parallel to the magnetic field (we will assume $\mathbf{B} = B\hat{x}$) the orientation of the magnetic bead is constrained by its alignment with the magnetic field, thus preventing rotation about this axis. In the $y-$direction, conversely, the bead is free to move and to align itself with the biomolecule tether, making l appear longer by an amount equal to the radius of the bead R. A schematic illustration if the bead oscillations is illustrated in Figure 4.1, adapted from the work of Velthuis et al. [53].
On the basis of these observations, we can then write the Taylor expansion of the potential energy around the equilibrium position, taking into account second derivatives [53]:

$$\begin{aligned} E_P(\mathbf{r}) &\approx E_P(\mathbf{r}_0) + \frac{1}{2}\frac{\partial^2 E_P}{\partial^2 x}\delta x^2 + \frac{1}{2}\frac{\partial^2 E_P}{\partial^2 y}\delta y^2 + \frac{1}{2}\frac{\partial^2 E_P}{\partial^2 z}\delta z^2 \\ &= \frac{1}{2}\left(\frac{F}{l}\right)\delta x^2 + \frac{1}{2}\left(\frac{F}{l+R}\right)\delta y^2 + \frac{1}{2}\left(\frac{\partial F}{\partial z}\right)\delta z^2, \end{aligned} \tag{4.5}$$

where the approximations $\frac{\partial^2 E_P}{\partial^2 x} = \frac{F}{l}$ and $\frac{\partial^2 E_P}{\partial^2 y} = \frac{F}{l+R}$ have been used.
By considering the $x-$ and $y-$directions perpendicular to the magnetic force, we can then relate the average potential energy of the system to the horizontal fluctuations of the beads (respectively $\langle \delta x^2 \rangle$ and $\langle \delta y^2 \rangle$), thus obtaining the following harmonic approximations:

$$\begin{aligned} \langle E_P \rangle_x &= \frac{1}{2}\frac{F}{l}\langle \delta x^2 \rangle = \frac{1}{2}k_x \langle \delta x^2 \rangle \\ \langle E_P \rangle_y &= \frac{1}{2}\frac{F}{l+R}\langle \delta y^2 \rangle = \frac{1}{2}k_y \langle \delta y^2 \rangle, \end{aligned} \tag{4.6}$$

with constants k_x and k_y being effective trap stiffness in the orthogonal directions with respect to the tether.

The equipartition theorem states that, for each axis,

$$\langle E_P \rangle = \frac{1}{2} k_B T, \tag{4.7}$$

so the magnetic force applied to the bead can be written in terms of the bead fluctuations in the direction parallel to the magnetic field as

$$F = \frac{k_B T l}{\langle \delta x^2 \rangle}. \tag{4.8}$$

By measuring the length of the biomolecule and the horizontal fluctuations of the bead, it is then possible to estimate the force acting on the bead itself. According to the Nyquist theorem, the correct sampling frequency in order to avoid systematic biases in the acquisition of the bead variance is half of the natural frequency of the target molecule.

Another important aspect to be considered in a MT experiment is the resolution in time and in length. The spatiotemporal resolution of the MT is quantified by calculating the Allan deviation (AD), which is defined as one-half the average difference in position between adjacent intervals of length τ averaged over all integrals of length τ. This provides a measure of the spatial resolution for measurements of duration τ. The main factors that affect the experimental resolution are the illumination source used for tracking the bead (laser or light emission diode), the bead dimensions and the characteristics of the tether. In their work of 2015 [54], D. Dulin et al. demonstrated that a coherent laser illumination source is compatible with high-spatiotemporal resolution measurements, because it substantially reduces the tracking noise. They also proved that a short and stiff tether together with small magnetic beads - the bead diameter and the sample length need to be comparable in size - provides the best conditions for the highest spatiotemporal resolution, as predicted by a simple model of Brownian motion in the MT. Nevertheless, when considering surface-melted beads, the best spatial resolution for a given measurement duration and light intensity is observed for larger beads and the resolution improves approximately as R_{bead}, consistent with predictions from basic Mie theory for the scattered light intensity. For example, for 2.8 µm-diameter M270 beads the AD equals 0.02 nm over measurements time of 1 s, while for 1 µm-diameter MyOne beads the corresponding AD is limited to 0.04 nm.

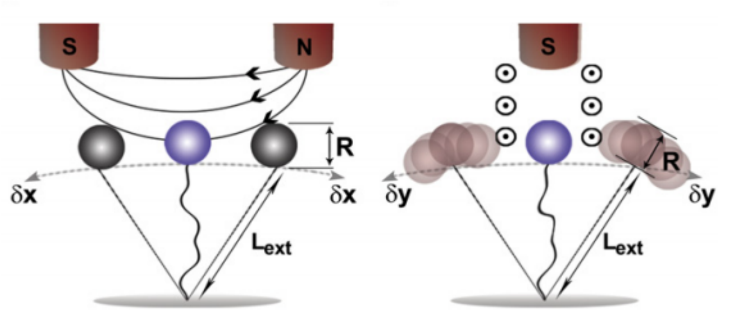

Figure 4.1: Schematic representation of the configuration of the magnetic bead and the tethering biomolecule in a MT setup. If the external magnetic field is $\mathbf{B} = B\hat{x}$, then the magnetic moment of the bead will align itself in this direction, so the bead oscillations will be reduced along this axis. On the contrary, in the $y-$direction the bead is free to move and to rotate, so the fluctuations in this direction will be larger.

4.1.2 MT setup and flow cell

Magnetic Tweezer (MT) measurements were performed with the state-of-the-art home-built setup illustrated in Figure 4.2. The design and the assembly of the mechanical components of the home-built MT, as well as the force calibration procedure, are presented in detail in the PhD thesis of P. Walker [48].

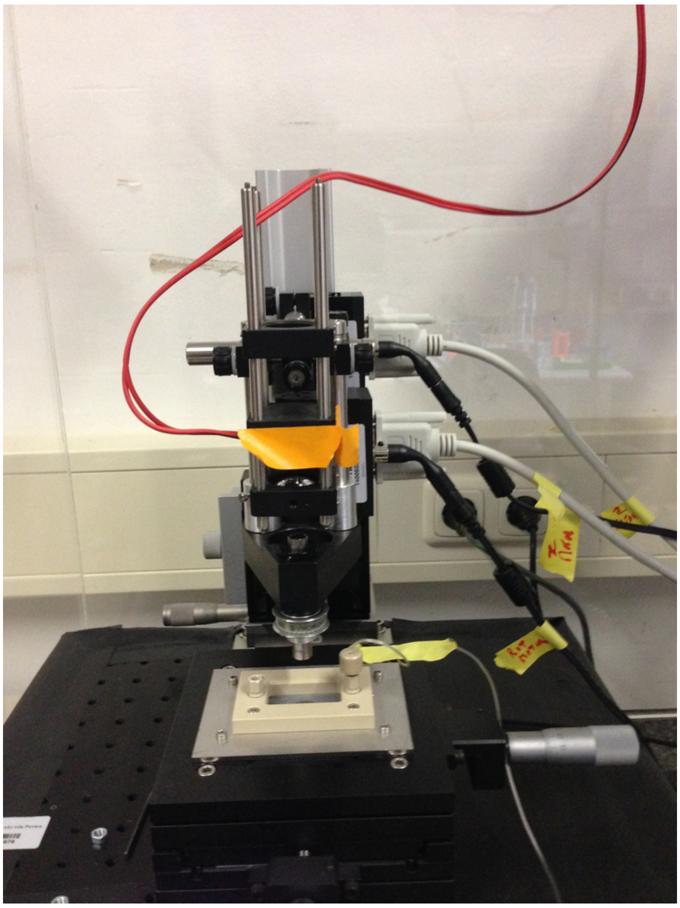

Figure 4.2: Home-built MT setup including, from top to bottom, a light-emitting diode, a pair of permanent magnets located in an aluminum holder and a flow cell.

From top to bottom, the instrument includes the following parts:

- a light-emitting diode (Osram Oslon SSL, red, 165lm) to illuminate the sample;
- a pair of permanent magnets oriented in a horizontal configuration, that can be rotated or moved vertically by controlling two DC-motors (respectively M-126.PD2 and C-150.PD, Physik Instrumente, Germany));
- a flow cell whose outlet is connected to a pump (ISM832C, Ismatec) for fluid handling;
- an oil immersion objective (60 × Plan Fluorite with correction collar, NA 0.9 or 40 × Plan Fluorite, NA 0.75, Olympus) placed on a piezo (Pifoc, P-726.1CD and controller, E-753.1CD, Physik Instrumente) stage underneath the flow cell holder.

The setup is controlled by using a computer (DELL Precision T3600) equipped with a frame grabber (PCIe-1433, National Instruments) and using software written in LabVIEW (National Instruments) described by Cnossen et al.[57]. When the monochromatic LED illuminates the sample and the beads, the resulting diffraction rings of the beads are captured by a CMOS camera. The objective between the flow cell and the camera is mounted on a piezo stage and thus the focal plane can be changed. The diffraction pattern of the bead changes with the distance to the focal plane and therefore allows to generate a Look-Up-Table (LUT) to extract height information of the bead [49]. To this end, reference pictures at known positions are taken before the actual measurements are performed. Hence, in addition to the lateral (x and y) position also the horizontal (z) information can be determined while applying a constant force.

A top view and a side view of the pair of permanent magnets placed in the aluminum magnet holder are illustrated in Figure 4.3. Each magnet consists of a cube whose edge is 5 mm. The distance between the two magnets is 1 mm and they are placed so that the nord pole of one magnet and the south pole of the other magnet are facing upwards. The two cubic magnets thus produce a horizontal magnetic field at the location of the magnetic bead, which is schematically illustrated in Figure 4.4. The value of the magnetic field as a function of distance from the center of magnet pairs (in z direction) for our particular magnet configuration is illustread in Figure 4.5.

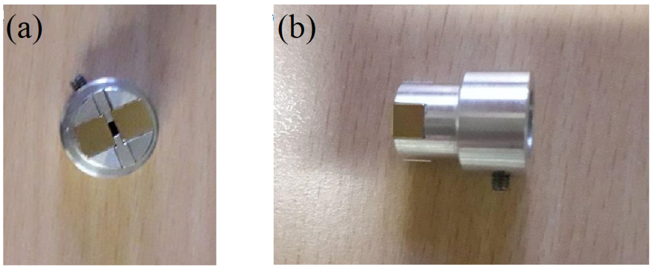

Figure 4.3: (a) Top view and (b) side view of the pair of permanent magnets placed in a suitable aluminum magnet holder for MT measurements.

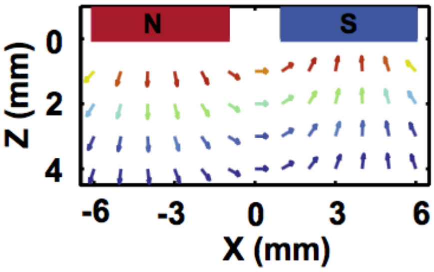

Figure 4.4: Conventional MT consists of two cubic, permanent magnets that produce a horizontal magnetic field at the location of the magnetic bead,

The flow cell was built from two coverslips (24 × 60 mm^2, Carl Roth, Germany) stuck together with a Parafilm (Carl Roth, Germany) layer, precut to form a flow channel. Two holes were made on the upper coverslip to allow fluid injection via the pump. The lower coverslip was previously coated with Epoxy Silane to let anti-digoxigenin molecules bind to the flow cell. For the experiments on the hairpin unzipping and on the sliding of the origami, we coated the bottom layer of the flow cell also with a solution of polystyrene beads (Polysciences, USA) 2000 times diluted in ethanol. An aliquot of 200 µL of this solution was poured on the coverslip and left to dry in air for approximately 1 h; after putting on top the Parafilm layer and the second coverslip, the flow cell was baked at 100 °C for 2 min to let the Parafilm melt and the polystyrene beads glue to the surface. In this way, these bead are fixed and can be used as reference beads for the measurements where small transitions need to be detected.

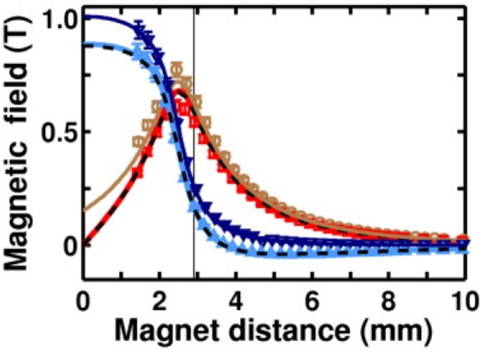

Figure 4.5: Magnetic fields (in x direction) as a function of distance from the center of magnet pairs (in z direction) in the vertical (brown and red) and horizontal (light and dark blue) configuration with a gap size of 1 mm. Data points are from measurements with a Hall probe in the absence (red and light blue) and presence (brown and dark blue) of an iron yoke. Solid lines show the results of corresponding calculations using a three-dimensional finite element solver while black dashed lines show the results of the semianalytical calculations presented in [**?**]. The thin vertical lines indicate the position of the flow cell surface in our current setup. Image adapted from [50].

The final flow cell was then placed in a plastic holder (see Figure 4.6) in the MT setup. Before starting experiments, the flow cell was passivated with 100 µg mL^{-1} anti-digoxigenin (Roche, Switzerland) in 1× PBS for 6 h, rinsed with 1× PBS, passivated again with the commercial mix BlockAid Blocking Solution (Thermoscientific solution) for 1 h to minimize nonspecific interactions and finally flushed with the buffer solution. As will be discussed in the following sections, we tried different buffer solutions to overcome nonspecific interactions between the sample and the surface or between the beads and the surface. The best mixture was composed of Tris-Acetic Acid-EDTA (TAE), 5 mMMgCl$_2$, 0.1 mg mL^{-1} bovine serum albumin (BSA) and 0.1% Tween20. Measurements used either 1 µm-diameter MyOne or 2.8 µm-diameter M270 superparamagnetic beads (Thermofisher Scientific, USA). The DNA origami nanostructures were first coupled to the streptavidin-coated beads by incubating overnight 10 µg of DNA construct and 2 mg of MyOne or M270 beads. The DNA origami-bead solution was then incubated in the flow cell for 1 h to let the DNA nanostructures bind to the surface. After incubation, a 1 pN force was applied to the sample and the flow cell was extensively flushed with buffer solution to remove unbound beads.

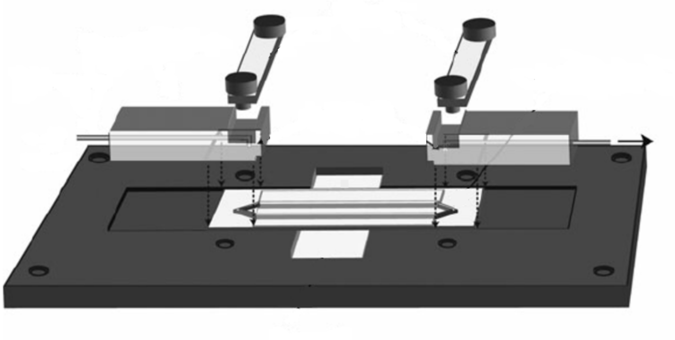

Figure 4.6: Schematic representation of the MT flow cell.

4.1.3 MT experiments

A picture of the field of view (FOV) imaged with the camera, during a MT experiment, is illustrated in Figure 4.7. The dark dots corresponds to the magnetic beads attached to the flow cell with the origami or unspecifically stuck to the surface. Beads that appear clusterized in the FOV are excluded from further experiments, while single beads that are far enough from each other to be resolved with the camera are analyzed. Before each MT measurement, a preliminary test is done in order to establish which are the beads of interest for a certain experiment. It is thus fundamental to optimize the incubation protocol in order to find the best origami concentration so that a high number of isolated beads are visible in the FOV.

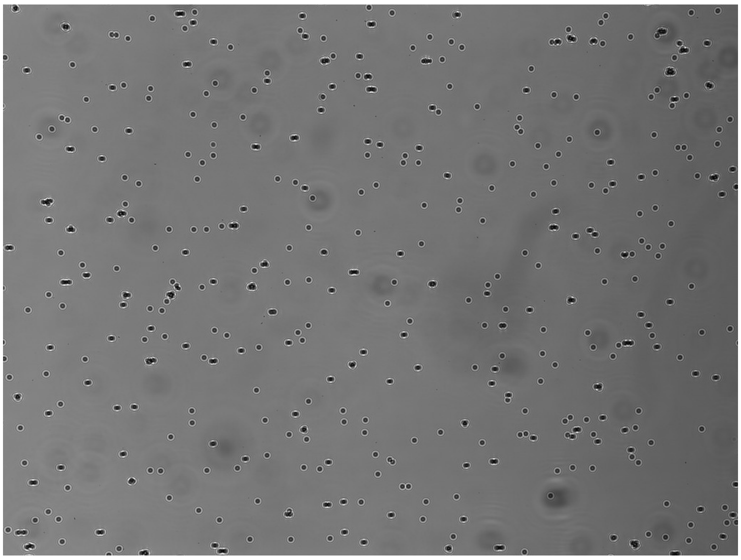

Figure 4.7: Image of the field of view obtained with a 60X magnification lens. The black spots represent the magnetic beads tethered to the surface of the flow cell.

A look-up table along the z-direction (ZLUT) of the diffraction pattern of each bead is produced by displacing the piezo connected to the objective lens and thus changing the distance between the sample and the objective in a controlled way; the ZLUT needs to be recorded before each measurement and is used to calibrate the bead position along the z-axis with an accuracy of 10 nm.

Before starting experiments, beads of interest are identified by moving the permanent magnets vertically to exert alternating forces of 1 pN (to fully stretch the molecule) and of 0.01 pN (close to zero force) in order to test the contour length of the tethers. The measured change in extension Δz is expected to be approximately the contour length L_C of the DNA origami. If $\Delta z \approx L_C$, the bead is probably attached to a single DNA origami structure and is kept for further measurements. If the tethering length does not change when varying the force, then the bead is likely to be stuck to the surface and so is used as a reference bead (see Figure 4.9). It is important to find stable reference beads before each experiment, because, in each recorded trajectory, the signal of the reference bead has to be subtracted to the signal measured for the other beads to reduce the influence of the mechanical drift. Conventionally, the *zero position* of each bead correspond to the position recorded at 1 pN force in order to reduce thermal noise; in this way, the $z-$coordinates measured at lower forces assume negative values.

For evaluating the force corresponding to a certain magnet position, we relied on the work of P. Walker [48]. The data relative to the magnet height h and the applied force F were interpolated with a poly-exponential function, thus leading to the following expressions, respectively for MyOne (diameter $d = 1\,\mu\text{m}$) and M270 ($d = 1\,\mu\text{m}$) beads:

$$F = -0.03 + 9.00\, e^{-0.78h} + 0.09\, e^{-0.04h},$$

and

$$F = \begin{cases} 0.32 + 73.72\, e^{-h/1.38}, & \text{if h} < 4 \text{ mm} \\ -0.96 + 69.41\, e^{-0.71h} + 1.64\, e^{-0.05h}, & \text{if h} \geq 4 \text{ mm.} \end{cases}$$

In Figure 4.8, the magnetic force corresponding to the magnets height with respect to the flow cell is illustrated for MyOne magnetic beads.

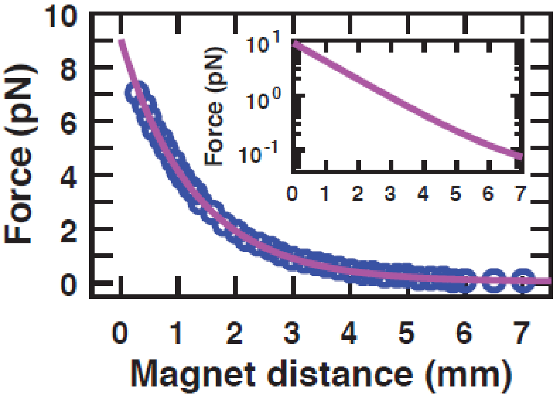

Figure 4.8: Force calibration for MyOne beads. Over the whole magnet position range, all measurement points recorded at 58 Hz (blue circle) are fitted with a double exponential fit (magenta solid line) with a $\chi^2 = 0.01$. Imaged adapted from [48].

When performing measurements in parallel, the unavoidable polydispersity of the magnetic beads has to be taken into account for evaluating the force. MyOne beads, for example, have a mean diameter of 1.05 µm and a relative variation in diameter of 3%. Since the magnetic moment increases linearly with the volume, a 3% variation in diameter leads to a 9% variation in the magnetic moment and consequently in the experienced force. N. Ribeck and O. Saleh showed that [52], in a MT experiment when several beads are manipulated in parallel, the applied force typically varies by 7%-10%. Bead polydispersity represents then the limiting factor in applying constant forces.

4.2 Mechanical characterization of the 4-helix bundle DNA origami

In this section, I will present the data relative to the characterization of the mechanical properties of the 4HB DNA origami described in the previous chapter.

The aim of this work was the study of the dynamics of a ssDNA hairpin when exposed to local temperature variations. Using a 4HB DNA origami as a tether for the hairpin in MT experiments offers two main advantages with respect to standard dsDNA: first of all, DNA origami structures can be decorated with AuNPs at specific positions (see paragraph 3.3.2), thus allowing the creation of local temperature variations; in the second place, they offer major stability due to their higher stiffness. We then performed preliminary MT experiments to characterize the mechanical properties of the 4HBs and to confirm this assessment.

After folding the 4HBs as described in section 3.3.1, we incubated 2 µL of 1 µm-diameter MyOne beads from the stock solution (c=10 mg mL^{-1}) with 1 µL of a 1 nM solution of 4HBs in TAE, 11 mM MgCl$_2$ buffer for 15 min. We diluted the sample in 300 µL of buffer solution and incubated 100 µL in the flow cell for 1 h. After incubation, we applied a 1 pN force and washed extensively with buffer solution to get rid of unspecifically attached beads. We selected the reference bead and the beads of interest (see for instance the bead in Figure 4.10) as explained in the previous paragraph and then started experiments.

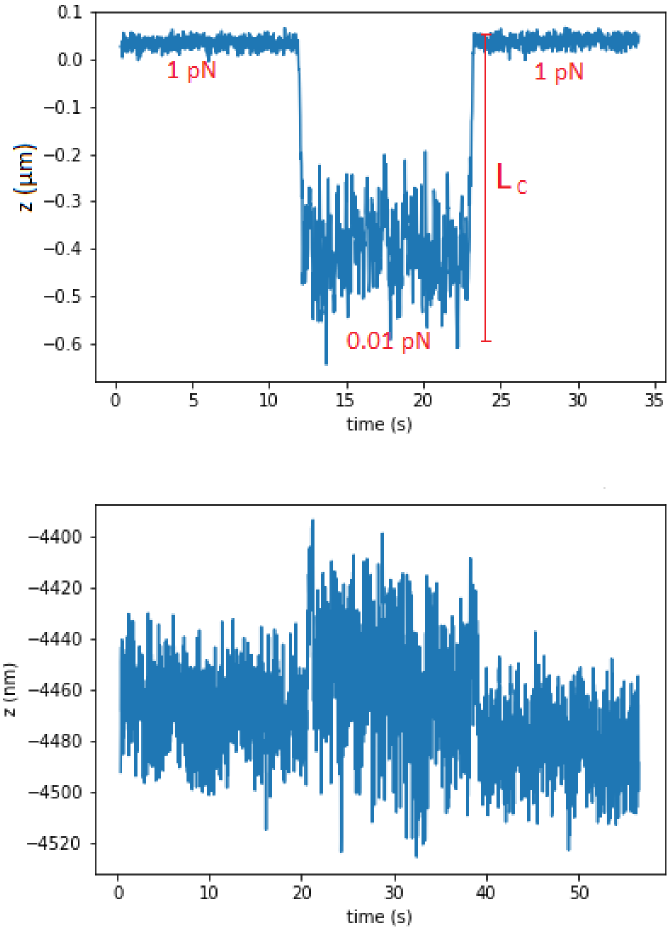

Figure 4.9: Measurements of the tethering length to select beads of interest and reference beads. In the first picture, the z-position of the bead changes with varying the force and the difference Δz is compatible with the contour length of the 4HB DNA origami ($L_C \approx 680\,\text{nm}$, thus indicating that a single origami structure is attached. In the second plot, the z-position remains almost constant at different forces, so the bead is used as a reference bead for further measurements.

The first measurements were aimed at characterizing the behaviour of the 4HBs at low forces: we successively applied constant forces of 0.02 pN, 0.2 pN and 0.5 pN for a time interval of 5 min while recording bead trajectories. The x, y and z positions for a representative bead are illustrated in Figure 4.11. From these plots, it is possible to see that fluctuations are asymmetric in the yx plane because of the anisotropy introduced by the external magnetic field $\mathbf{B}$ in the system. In fact, the bead tends to align to the external magnetic field and is free to rotate around the axis parallel to it ($\mathbf{B} = B_x$ in this case), while rotations around the perpendicularly oriented y axis are suppressed. As a consequence, fluctuations are more suppressed in the x direction compared to the y direction.
In the yz plane, the bead positions describe a sort of arch, as the bead is anchored to the surface of the flow cell through the 4HB and its maximal lateral excursion is limited by the length of the tether. This behaviour is more evident at lower forces when the interaction with the external field is weaker and does not limit the possible configurations of the bead.

For the beads that were showing the correct behaviour at low forces, force-extension curves were recorded. The permanent magnets were moved in steps of 0.5 mm in order to apply increasing forces of 0.08 pN, 0.12 pN, 0.16 pN, 0.22 pN, 0.31 pN, 0.44 pN, 0.63 pN, 0.91 pN, 1.32

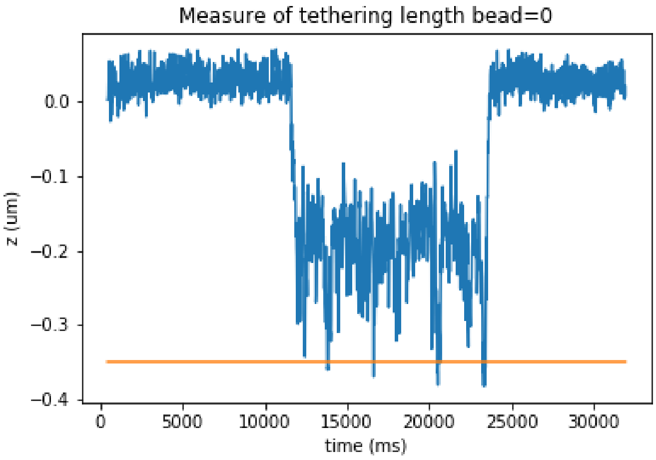

Figure 4.10: Measure of the tethering length at 1 pN force. The orange line represents the offset of the bead which needs to be subtracted to the extensions measured at higher forces to obtain positive values in the end-to-end distances of the DNA origami. It is calculated as the minimum of the $z-$positions at 0 pN force, after smoothing of the data.

pN, 1.93 pN, 2.83 pN and 4.17 pN for 1 min while recording the beads trajectories. The positions occupied by each bead during the time interval at constant force were averaged and plotted with the corresponding applied force, thus obtaining a force-extension curve like the one represented in Figure 4.12. As expected, the length of the 4HB continuously increases until the total extension of 680 nm is reached. The force-extension curve mediated over several measurements is represented in Figure 4.13.

We performed Monte Carlo simulations to compute the force-extension curve of a polymer characterized by the same contour length as our 4HB DNA origami and by a variable persistence length that could be set as an input parameter. For running Monte Carlo simulations, we considered a linear polymer made up of N+1=1000 beads connected by N rigid bonds of equal bond length b which was calculated by setting the total length equal to the contour length of the 4HBs. The energy of the chain, in temperature units $k_B T = 1$, is given by the Hamiltonian:

$$H = H_s + H_b. \tag{4.9}$$

H_s models the stiffness of the fibre and is given by

$$H_s = -k_s \sum_{i=1}^{N-1} \mathbf{t}_i \cdot \mathbf{t}_{i+1}, \tag{4.10}$$

where $\mathbf{t}_i = \mathbf{r}_i - \mathbf{r}_{i-1}$ is the $i-$th bond vector and $\mathbf{r}_i$ is the $i-$th bead position in three dimensions. The stiffness constant k_s determines the persistence length l_P of the polymer chain. In fact, from the calculation of the bond-bond correlation function, it can be shown that[40]

$$l_p = \frac{1}{\log(\coth k_s - 1/k_s)} \simeq k_s, \quad \text{if}\, k_s \gg 1. \tag{4.11}$$

The auxiliary term

$$H_b = k_b(\mathbf{r}_N - \mathbf{r}_0)^2 \tag{4.12}$$

is a biasing term introduced for increasing the probability to reproduce conformations of the polymer overstretched ($k_b < 0$) or looped ($k_b > 0$), thus sampling all the possible configurations

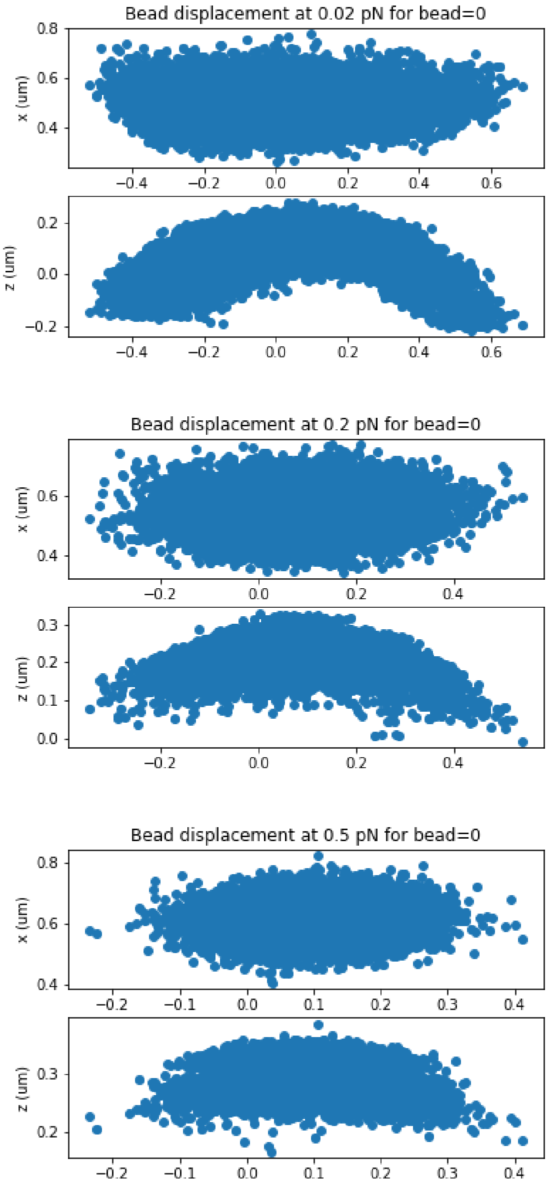

Figure 4.11: Bead fluctuations at different forces (0.02 pN, 0.2 pN and 0.5 pN).

of the macromolecules.
We compared the experimental data with the theoretical ones to test the rigidity of the structures. From TEM images analysis, we expected the 4HBs to be characterized by a persistence length of $485 \pm 66\,\mathrm{nm}$, a value consistent with other results presented in literature and with theoretical models (see Chapter 3). We then simulated force-extension curves of polymers with different persistence lengths between 50 nm (the theoretical value for dsDNA) and 500 nm and we found out that the experimental MT data are in agreement with simulated data for structures with a lower l_P than expected from the optical analysis. In Figure 4.14, the average force-extension curves for the 4HBs is plotted together with the simulated data for a polymer with $l_P = 68\,\mathrm{nm}$.

The fact that the two methods for estimating the persistence length (TEM imaging and MT measurements) do not agree between themselves confirms that the attachment of the origami to the surface is crucial for the rigidity of the whole structure, as already shown in the work of Kauert et al.[66]. In Figure 4.15, the force-extension curve measured for our 4HBs is plotted

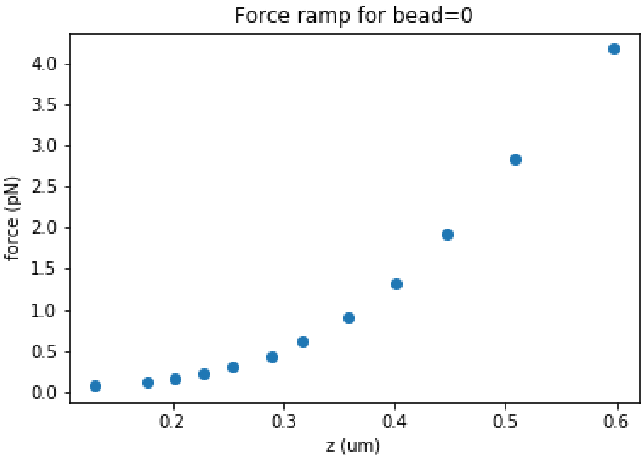

Figure 4.12: Force-extension curve of the 4HB DNA origami tethered between the surface of a MT flow cell passivated with anti-digoxigenin molecules and streptavidin-coated magnetic beads.

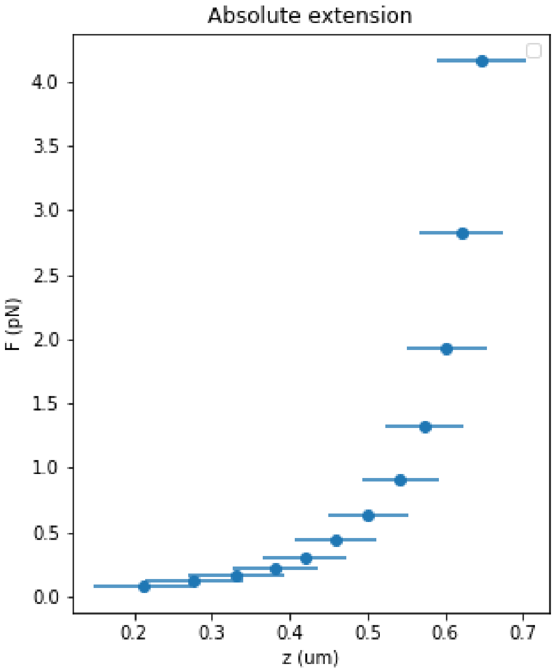

Figure 4.13: Force-extension curve of the 4HB DNA origami mediated over several measurements.

together with the curve shown in the paper of Kauert, that refers to a 4HB with a bigger anchor to the surface, made up of 20 helices (see Figure 4.16).

By comparing the two graphs, it is possible to see that the 4HB with a 20-helices-anchor behaves as a rigid rod and shows a long extension even at low forces; on the contrary, the 4HB without anchor seems to be a flexible polymer (worm-like chain with small persistence length). Since the analysis of the TEM images revealed that the 4HB is characterized by a persistence length comparable to its contour length, the apparent flexibility of these origami has to be caused by the particular experimental configuration. In fact, the system made up of the two digoxigenin-modified staples for binding the anti-digoxigenin coated surface and the 4HB itself can be modelled as a series of two springs, whose elastic constants - respectively k_{dig} and $k_{4\text{HB}}$ -

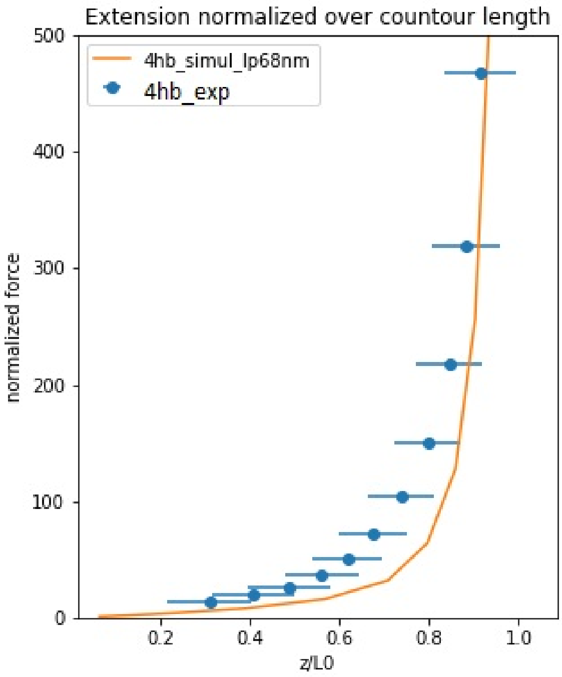

Figure 4.14: Comparison between the average force-extension curve for the 4HB DNA origami and the simulated force-extension curve for a polymer with persistence length $_p = 68\,\text{nm}$.

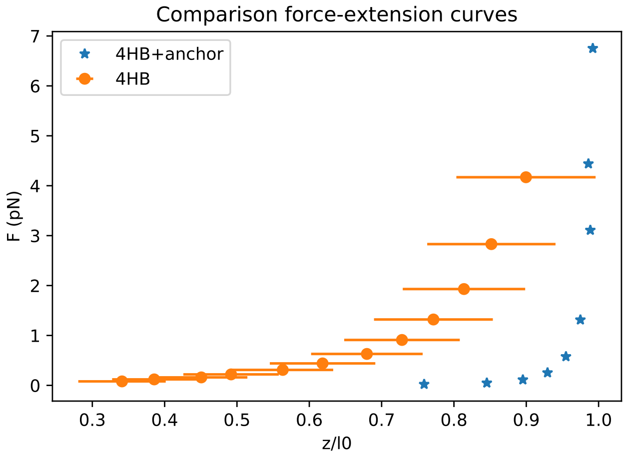

Figure 4.15: Comparison between the force-extension curves measured for the 4HB DNA origami without anchor and the data presented in the work of Kauert et. al [66] for the 4HB DNA origami with anchor.

combine according to the following law:

$$\frac{1}{k_{\text{TOT}}} = \frac{1}{k_{\text{dig}}} + \frac{1}{k_{\text{4HB}}}. \tag{4.13}$$

Since we expect the elastic constant of the digoxigenin-molecules bound to the surface to be smaller than the elastic constant of the DNA origami, the term due to the digoxigenin contribution is dominant and does not allow a proper estimation of the persistence length of the 4HBs. From this analysis, we concluded that a stronger attachment to the surface was needed in order to obtain a multi-helix bundle that behaves like a rigid-rod. For further MT measurements, we

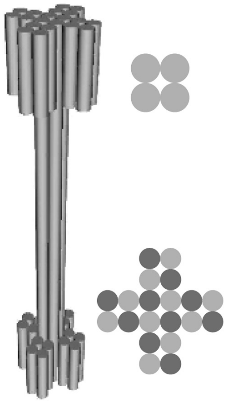

Figure 4.16: Scheme of the origami analyzed in the paper of Kauert et al. [66], which consists of a 4-helix bundle structure with both extremities made up of 20 helices, in order to assure a stronger attachment to the surface of the MT flow-cell.

then designed a 4HB with a base made up of 20 helices (similar to the one designed by Kauert and illustrated in Figure 4.16) with the ssDNA hairpin inserted inside the origami. Since only the 3′-end of the staples could be modified with a digoxigenin molecule for binding the surface, this scheme determined a 10-molecules anchor to the flow cell. A detail of the bond between the digoxigen and the anti-digoxigenin molecules is illustrated in Figure 4.17. In this way, we expected to reduce artefacts and to get clear access to the dynamics of the target hairpin included in the 4HB.

G. Neuert et al. investigated the rupture probability of the digoxigenin/anti-digoxigenin complex over a wide range of loading rates in force spectroscopy experiments with the intention of estimating its stability for biophysical applications under force load [?]. In their work, Neuert and his collaborators shows that the dissociation constant k_{off} of the digoxigenin/anti-digoxigenin binding increases as the force load increases, thus causing a higher probability to observe artifacts. Nonetheless, in the range of forces used for our magnetic tweezer experiments (1-20 pN), the dissociation constant does not undergo significant variations and is $k_{off} = 0.015\,\mathrm{s}^{-1}$. It is then reasonable to exploit the digoxigenin/anti-digoxigenin bond for our purposes.

4.3 Mechanical characterization of the 4-helix bundle DNA origami with hairpin

After determining the stiffness of the 4HBs, we performed MT experiments on the 4HBs modified with the introduction of the hairpin to detect the hairpin zipping and unzipping mechanism. A schematic representation of the experimental configuration is represented in Figure 4.18.

Each MT experiment included measurements of the tethering length of the beads to assess the correct attachment of the origami and to identify beads of interests, as described in the previous sections, and then measurements of the extension of the 4HBs at different constant forces. Force-extension experiments were performed by applying a constant force and recording the bead trajectories for 5 min, then changing the force and measuring the bead positions in the new magnet configuration. Initially, we increased the force from 6 pN to 14 pN in steps of approximately 0.5 pN in order to progressively extend the origami; later, we started from higher forces (14 pN) and gradually decreased them in order to overcome at once the coupling between the sample and the surface of the flow cell.

When the applied magnetic tweezer force F_{MT} equals the unfolding force $F_{1/2}$, the hairpin has a 50% probability to be unfolded [60], so the system is expected to rapidly switch between the

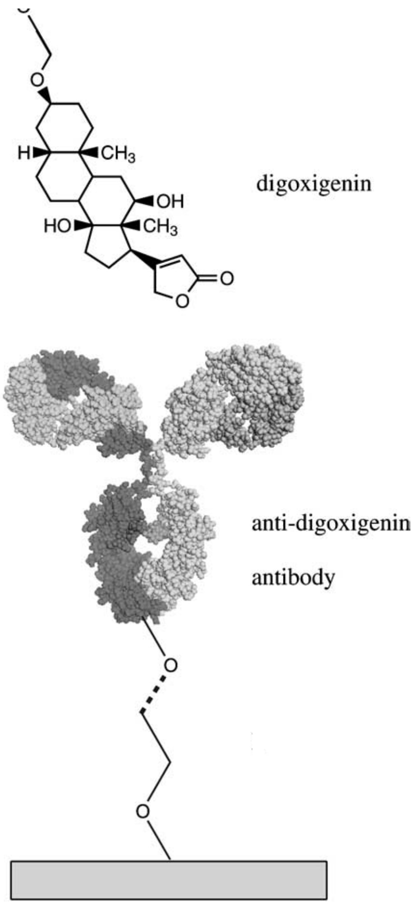

Figure 4.17: Scheme of the bond between the digoxigenin and the anti-digoxigenin molecules used for attaching the 4HB origami to the MT flow cell. A digoxigenin molecule was attached to each 3′-end of the helices forming the anchor of the 4HB, thus resulting in a 10-bonds attachment. Each digoxigenin molecule was bound to an anti-digoxigenin molecule attached to the surface of the MT flow cell.

zipped to the unzipped state and this phenomenon should lead to a clear two-states pattern in the force-extension curve. When $F_{\mathrm{MT}} < F_{1/2}$, the hairpin should mainly be in its closed state, but, as the force increases, some transitions to the open state should also be visible in the plot; similarly, for $F_{\mathrm{MT}} > F_{1/2}$, the system is assumed to be mostly in its unfolded state, but the probability that it also populates the folded state is nonzero. We thus expect to observe an increasing number of spikes in the bead trajectory as approaching the unzipping force and frequent transitions from the open to the closed state and vice-versa when $F_{\mathrm{MT}} = F_{1/2}$. By considering a length per single-base in ssDNA of $l_B = 0.63 \pm 0.08\,\mathrm{nm}$[17], we expected a length variation of approximately 30 ± 4nm in the origami structure as a consequence of the unzipping of a 24 bp long-hairpin and hence a fluctuation of the bead height $\Delta z \approx 30$ nm.

According to Woodside et al. [60], the force required to unzip a 24 bp long ssDNA hairpin is $F_{unzip} \approx 10$ pN. Magnetic beads with a diameter of 2.8 µm are required to apply forces in this order of magnitude because they are characterized by a higher magnetic moment. Nonetheless, 2.8 µm-diameter M270 magnetic beads tend to have more nonspecific interactions with the surface of the flow cell with respect to 1 µm-diameter Myone beads, because of their bigger contact surface, so we slightly modified the experimental protocol optimized in the previous months to adapt it to the new measuring conditions. Regarding the buffer solution used to fill the flow cell, we employed a TAE solution with a lower magnesium concentration (from 11 mM, the standard concentration for gel electrophoresis analysis and purification, to 5 mM) to reduce interactions

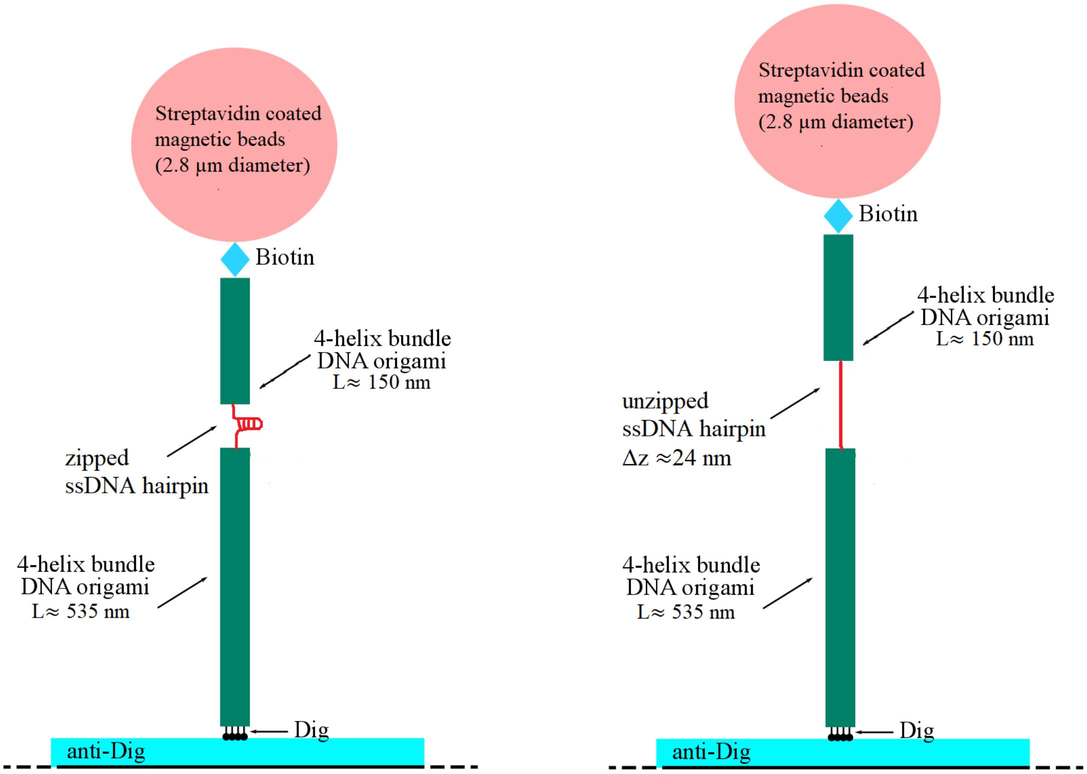

Figure 4.18: Schematic representation of the experimental configuration: a 4HB DNA origami is linked to the surface of the flow cell via the anti-Digoxigenin/Digoxigenin bond and to the magnetic bead via the Biotin/Streptavidin bond. The origami is composed of two 4HBs elements (respectively ≈150 nm and 535 nm long) linked with a ssDNA hairpin. When the magnetic bead is pulled with a magnetic force corresponding to the unzipping force of the hairpin, a variation in the bead position $\Delta z \approx 24$ nm is recorded by the camera.

between the bead and the surface. As shown in the work of Bosco et al. [72], a lower magnesium concentration does also reduce the force necessary to unfold secondary structures (see Figure 4.19).

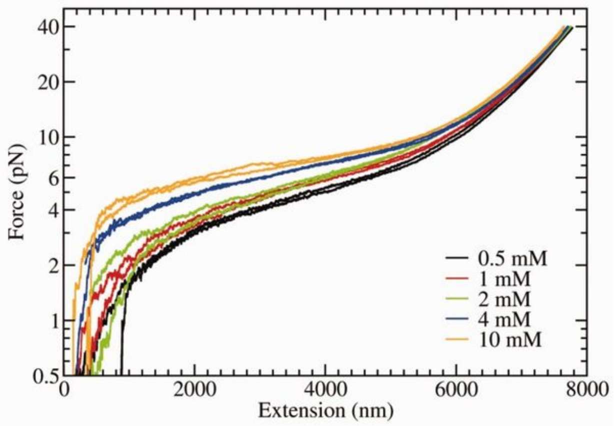

Figure 4.19: Force-extension curve of a 13 kilobases ssDNA at varying $MgCl_2$ concentration. The lower is the magnesium concentration, the lower is the force required to denature the secondary structures [72].

We added 0.1% in volume of Tween20 and $0.1\,\mathrm{mg\,mL^{-1}}$ of Bovine Serum Albumin (BSA) to prevent interactions between the bead and the surface and/or between the hairpin and the surface. After several tests, we also figured out that the addition of Sodium Chloride in a concentration of 500 mM makes the origami structures even more compact, thus reducing nonspecific binding. We used the same protocol as for 4HBs for the flow cell preparation and passivation.

Some representative images of the MT experiments performed on the 4HB DNA origami including the ssDNA hairpin are illustrated in the figures below. The acquired data proved that the protocol of preparation of the beads and the origami was successful, as more than 25% of the beads were correctly bound to the surface of the flow cell through molecules showing the correct tethering length. Force-extension curves were recorded and the attachment to the surface was stable even at forces $F > 13\,\mathrm{pN}$, thus confirming the strength of the multi-helix anchor with digoxigenin-modified staples. In many samples, fluctuations in the $z-$position of the beads compatible with the zipping of the 24 bp hairpin were observed, so we demonstrated that this experimental configuration was efficient in investigating the dynamic of the hairpin. Nonetheless, a great limitation of MT experiments derives from the fact that the polymers of interest are linked to the surface and so they can interact with the substrate. Despite testing different protocols, we could not fully eliminate the non-specific bonds between the 2.8 µm bead and the surface of the flow cell. The most significant data, as well as the main difficulties of this experimental approach, are discussed in detail in the remainder of this paragraph.
The bead in Figure 4.20 shows the expected behaviour: its tethering length is compatible with the total length of the 4HB and the extension of the origami increases as the force grows from 5 pN to 14 pN. These observations indicate that the sample is correctly attached to the bead and that it does not interact with the surface. When analyzing the force-extension data more in detail, it is possible to see some jumps in the z-coordinate of the bead corresponding to $\Delta z \approx 15\,\mathrm{nm}$ (see Fig.4.20c), that can be explained with a partial opening/closing of the hairpin included in the 4HB. Since in our design, the ssDNA hairpin directly belongs to the origami, it is also possible that the hairpin does not unzip entirely because of the steric hindrance. The jumps in the $z-$position only appear when the pulling force is $F_{\mathrm{MT}} \approx 13\,\mathrm{pN}$, thus indicating that this value is close to that of the unfolding force $F_{1/2}$. Nonetheless, we do not observe a clear two-state system pattern in this range of forces.

The same behaviour is observed for the bead in Figure 4.21: the tethering length is compatible with the contour length of the origami, thus indicating that the 4HB is correctly assembled with the MT bead. The plot of the trajectory at different forces shows the expected response: as the force increases, the DNA origami is progressively elongated and the z-position of the bead increases till the value of 680 nm, that corresponds to the total extension of the 4HB. When the applied force is around 12 pN, some spikes of $\Delta z \approx 20\,\mathrm{nm}$ can be observed in the bead trajectory: they can be explained by assuming a hairpin transition from the zipped to the unzipped state, but their frequency remains constant as the force approaches the unfolding force, contrary to what we would expect from theoretical predictions.

Similarly, the 4HB illustrated in Figure 4.22 is well attached to the bead and to the surface of the flow cell, but no transitions between the folded and the unfolded configuration are observed at these forces.

In Figure 4.23, the tethering length of the bead ($L_C \approx 250\,\mathrm{nm}$) is shorter than expected for the 4HBs. Nonetheless, when applying forces $F_{\mathrm{MT}} \approx 13\,\mathrm{pN}$, the bead position along the z-axis

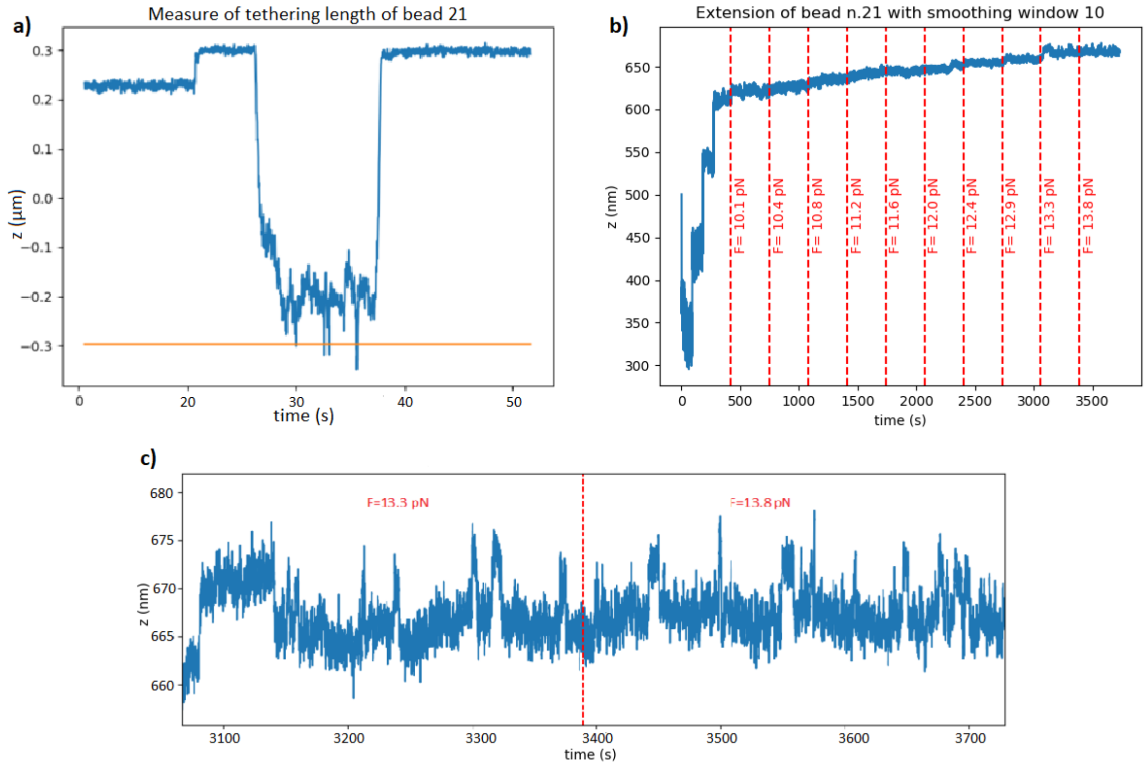

Figure 4.20: Measurement of the tethering length (a) and of the bead trajectory (b, c) at different constant forces for a 4HB DNA origami including a 24 bp long hairpin. The red vertical lines in b) mark time intervals during which the force is constant.

suddenly reaches a value $z \approx 680\,\text{nm}$, *i.e.* the total length of the 4HB origami. For forces in the range between 11 pN and 13 pN, the bead trajectory shows several spikes, whose frequency increases as the applied force increases (see Figure 4.24): this behaviour is in accordance with what expected for a ssDNA hairpin transition between the zipped and the unzipped state and the length variations $\Delta z \approx 24\,\text{nm}$ are consistent with a 24 bp long hairpin, as in the case of our design. The fact that the origami is not fully extended when these transitions occur can be explained by assuming a nonspecific binding between the sample and the surface of the flow cell: if we describe the 4HB modified with the hairpin as two short 4HBs connected with a ssDNA hairpin, then we can suppose that the lower part of the 4HB is stuck to the surface, while the hairpin and the upper part are free to move. As F_{MT} approaches $F_{1/2}$, the hairpin unzips, but at the same time, the increased force overcomes the interaction with the surface and makes the origami elongate. In Figure 4.25, the time interval during which the hairpin transitions occur is highlighted and the corresponding bead fluctuations in the xy plane are represented; for the region of interest, a histogram counting the positions of the bead has been made. In the histogram two peaks separated by a distance of 20 nm are clearly visible: they correspond to the zipped and the unzipped state and the closed state is more populated, as at low forces the hairpin is mostly zipped. On the basis of these data, the measured unfolding force is $F_{1/2} = (12.4 \pm 1.0)\,\text{pN}$, where the error of 1 pN takes into account the bead polydispersity and thus the variability in the evaluated applied forces.

Since we encountered several times the problem of the nonspecific binding between the sample and the surface of the flow cell, we also recorded the bead trajectories by starting with a

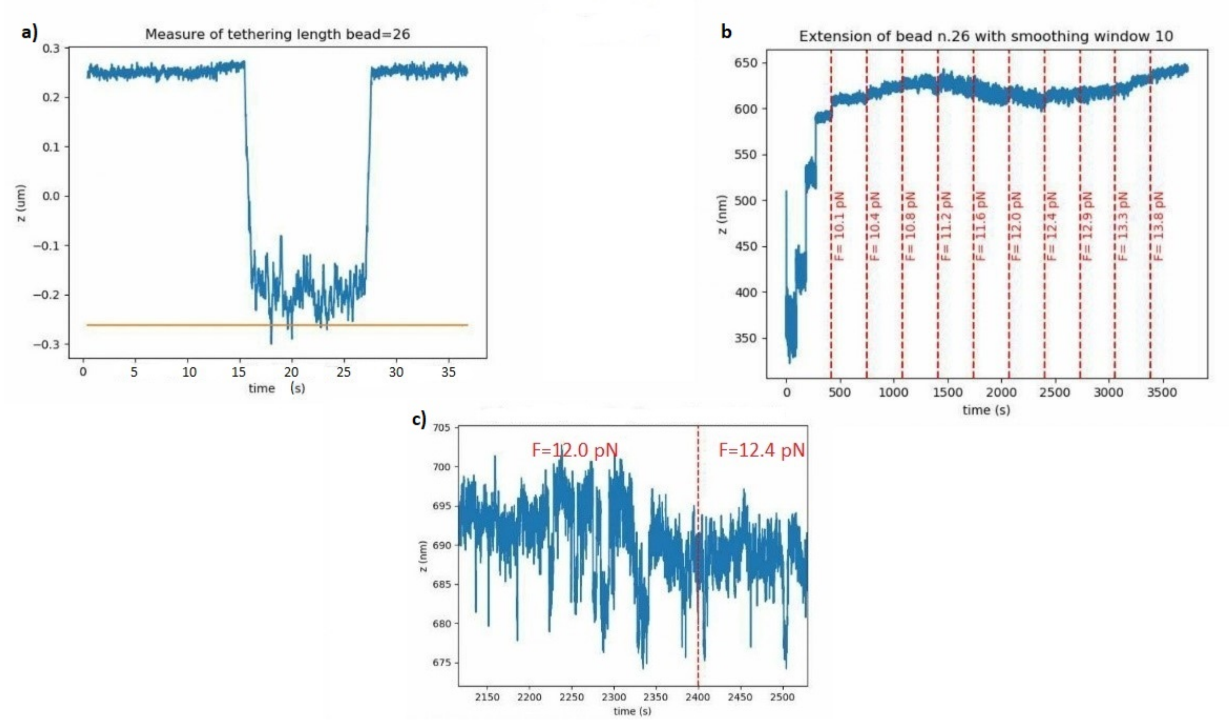

Figure 4.21: Measurement of the tethering length (a) and of the bead trajectory (b, c) at different constant forces for a 4HB DNA origami including a 24 bp long hairpin. The red vertical lines in b) mark time intervals during which the force is constant.

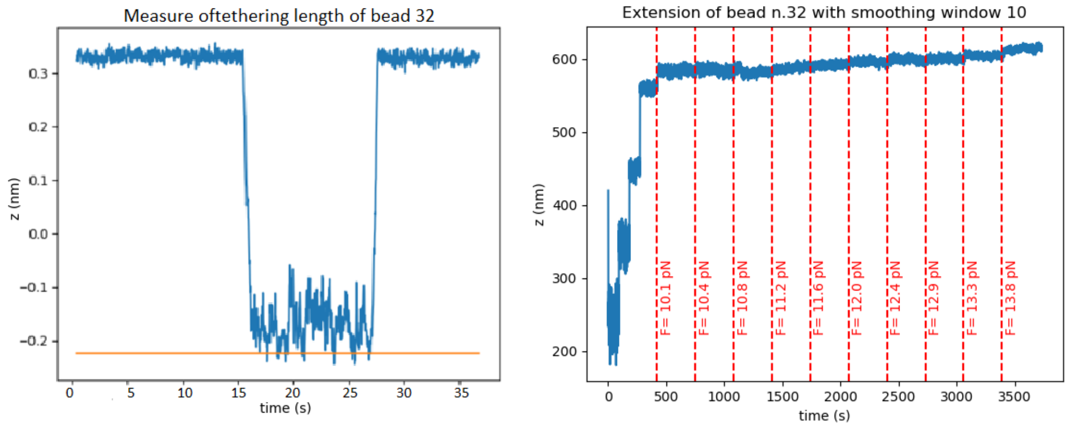

Figure 4.22: Measurement of the tethering length and of the bead trajectory at different constant forces for a 4HB DNA origami including a 24 bp long hairpin. The red vertical lines in b) mark time intervals during which the force is constant.

higher force and then progressively decreasing it: in this way we expected the origami to immediately reach its full extension and then to bend and shorten at lower forces. Representative plots of this set of measurements are illustrated in Figure 4.26 and 4.28. In Figure 4.26 the tethering length of the bead is $L \approx 500\,\mathrm{nm}$, so it indicates a correct attachment to the origami. When a force of 14 pN is applied, the 4HB is further elongated and stretched and then the extension remains constant for forces in the range of 14-10 pN. The force-extension data have been analyzed in detail and a histogram of the bead positions collected in a time interval at constant force has been realized (see plots in Figure 4.27). The analysis did not reveal any hairpin transition for this range of forces.

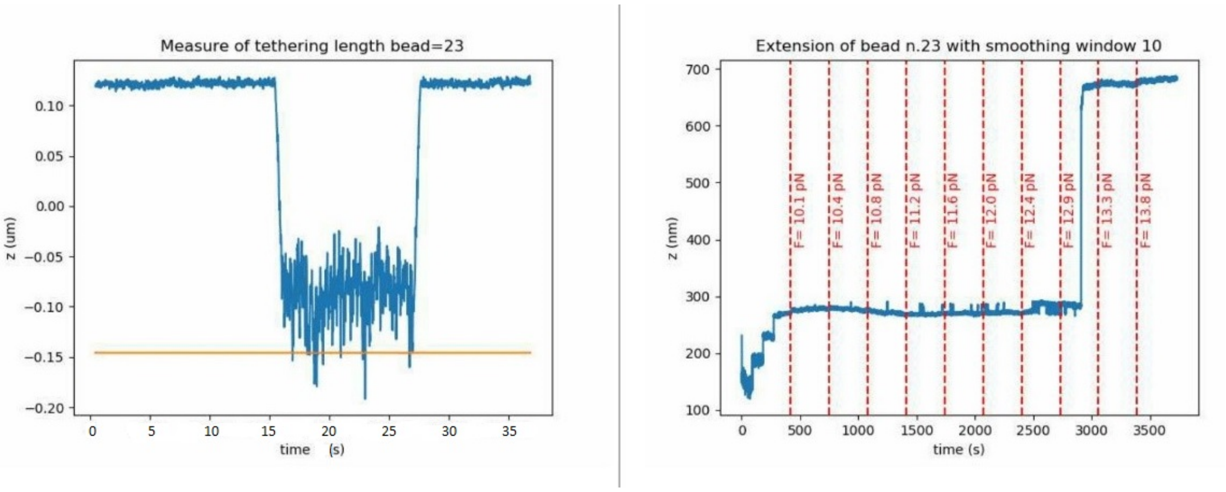

Figure 4.23: Measurement of the tethering length and of the bead trajectory at different constant forces for a 4HB DNA origami including a 24 bp long hairpin. The red vertical lines mark time intervals during which the force is constant. A detail of the bead position at forces of 12 pN and 12.4 pN is also illustrated.

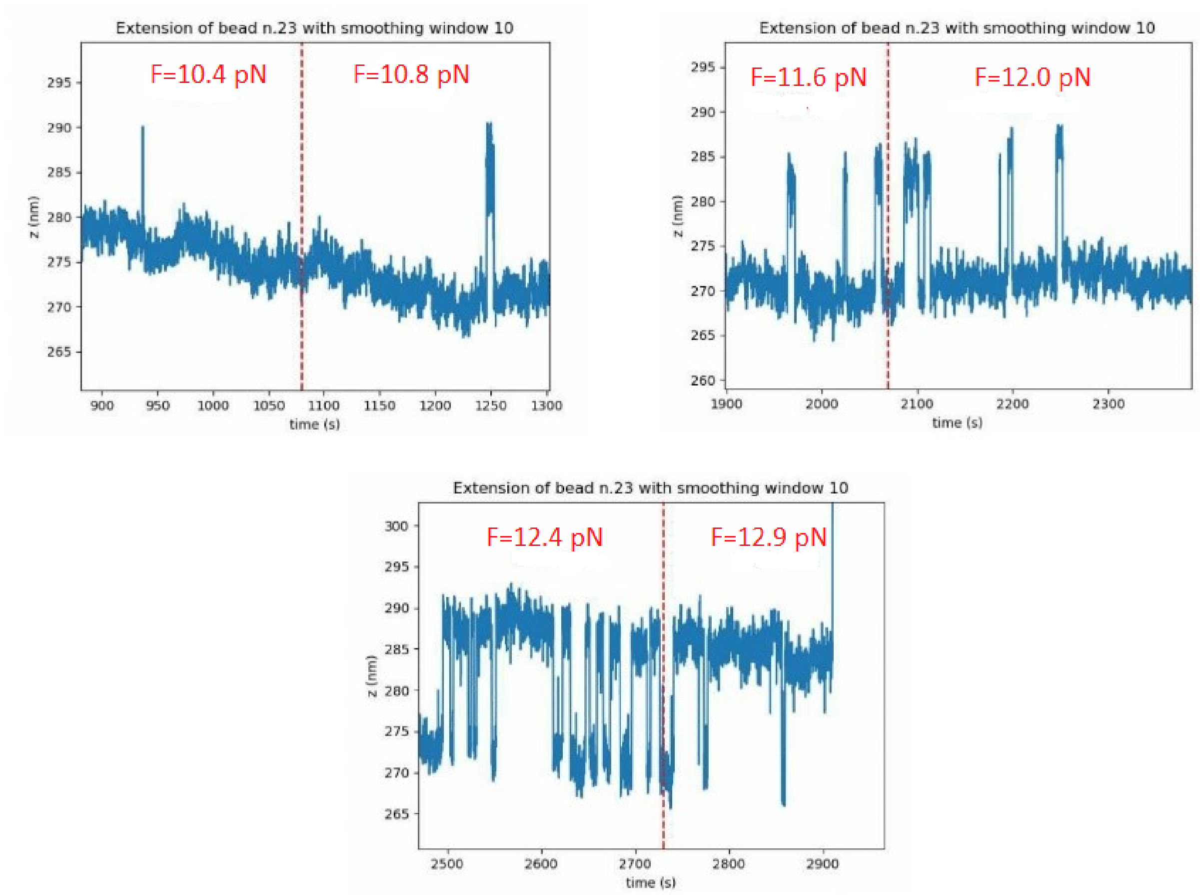

Figure 4.24: Detail of the bead trajectory plot in Figure 4.23: representation of bead trajectories corresponding to forces at which the hairpin unzipping/zipping process occurs.

In Figure 4.26, the measured tethering length is shorter than the total length of the 4HB, probably because of a nonspecific binding between the sample and the surface of the flow cell;

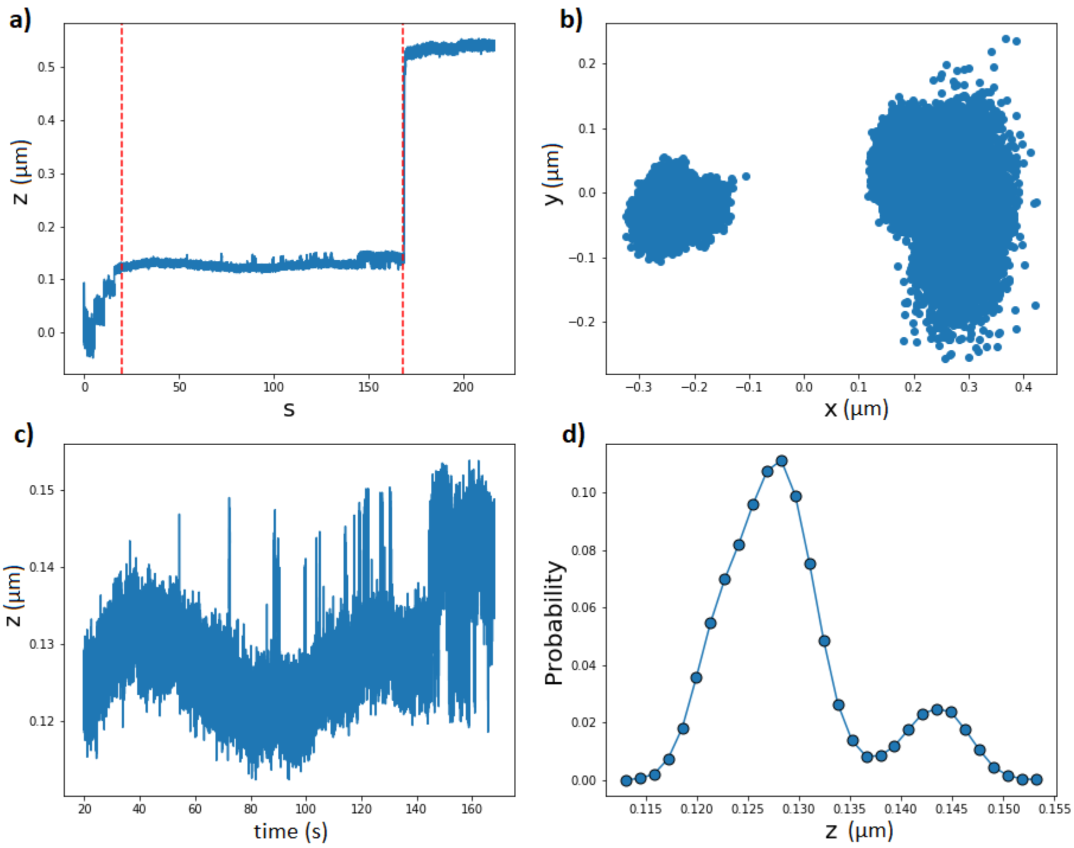

Figure 4.25: a) Plot of the bead trajectory while applying a force ramp; b) Bead fluctuations in the xy plane in the time interval in which the hairpin transitions have been observed; c) Detail of the bead trajectory plot in a) to show the spikes in the bead positions that can be explained with the hairpin unzipping; d) Histogram of the bead positions occupied during the time interval highlighted in c).

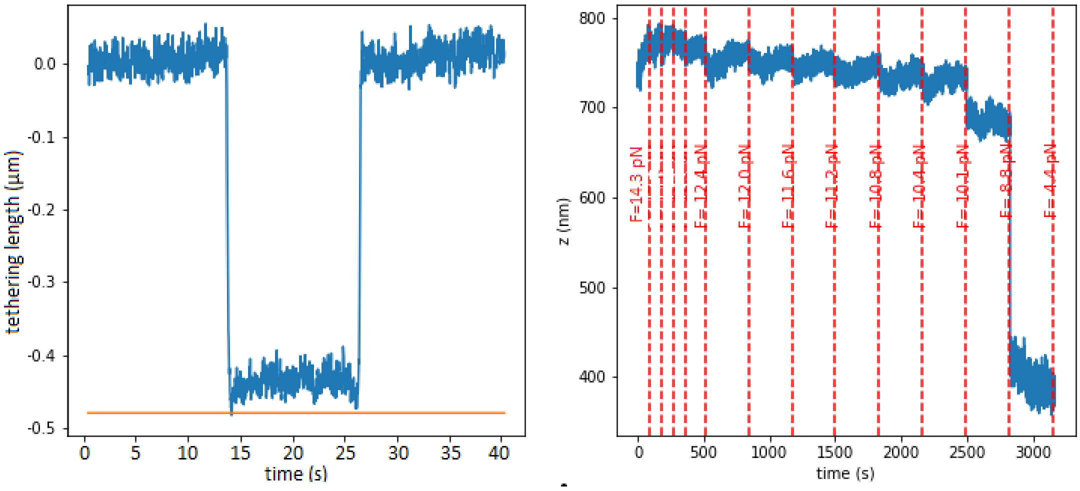

Figure 4.26: Measurement of the tethering length and of the bead trajectory at different constant forces for a 4HB DNA origami including a 24 bp long hairpin. The red vertical lines mark time intervals during which the force is constant.

anyway, when a 14 pN force is applied, the interaction is overcome and the origami reaches an extension of $\approx$ 600 nm, that remains constant even when the force is decreased. Since this z-value is still slightly smaller than 680 nm, the origami is probably not in the optimal binding

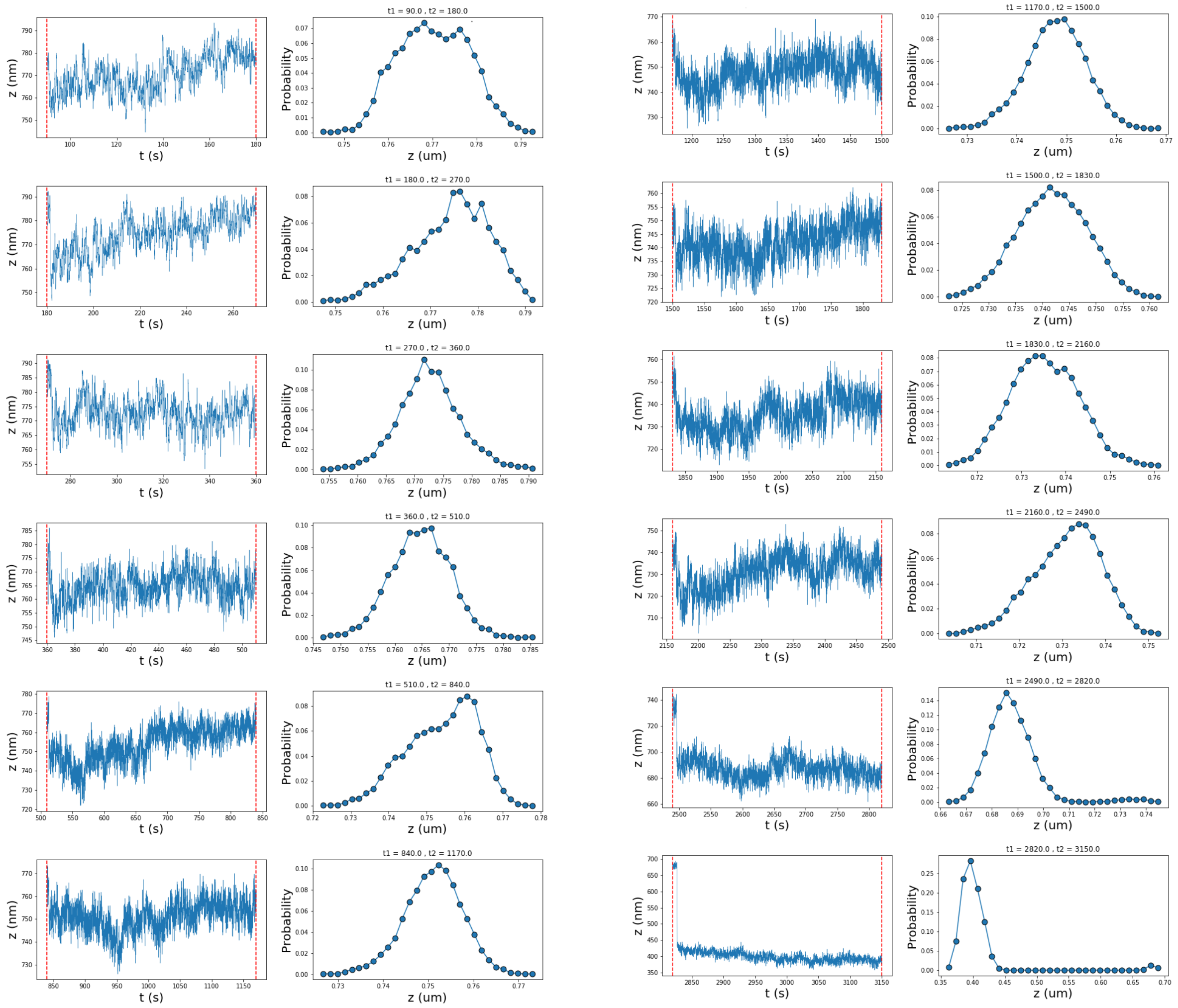

Figure 4.27: Detail of the bead trajectory plot in Figure 4.26: the bead trajectories are represented separately for each time interval in which the force is kept constant, together with the histograms of the occupied positions during the same period.

configuration with the bead, but the hairpin should be free to unzip. Anyway, also in this case, no hairpin transitions are observed.

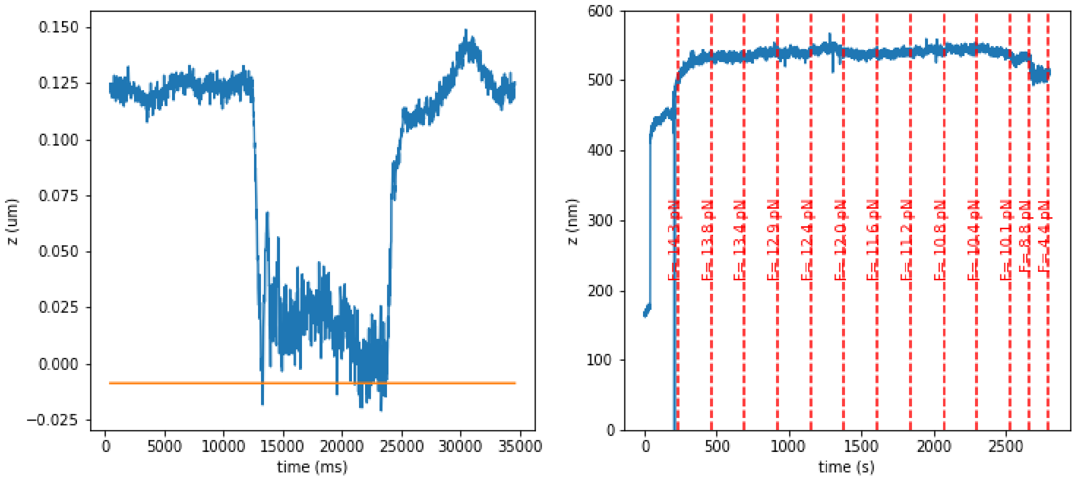

Figure 4.28: Measurement of the tethering length and of the bead trajectory at different constant forces for a 4HB DNA origami including a 24 bp long hairpin. The red vertical lines mark time intervals during which the force is constant.

4.4 Relevant results

In this chapter, I presented several results related to the MT measurements performed on the 4HB DNA origami.

We exploited the biotin/streptavidin bond and the digoxigenin/anti-digoxigenin bond to allow binding of the DNA origami respectively to the magnetic beads and the surface of the flow cell for MT experiments. In particular, the structure of the 4HB DNA origami was suitably designed in order to firmly binding to the surface of the flow cell and avoid artefacts in the measurements. We then identified beads of interest and we measured their extensions at different forces in order to investigate the dynamics of the target ssDNA-hairpin included in the origami. After repeating several MT experiments, we were able to clearly detect the zipping/unzipping mechanism of the 24 bp hairpin introduced in the DNA origami structure at F=12 ± 1 pN. Anyway, the short length of the tether caused many unspecific interactions between the surface and the origami itself that are difficult to be avoided. In order to overcome this main limitation of surface force spectroscopy, we performed experiments to characterize the dynamics of the hairpin by using a force-sensor device based on a DNA origami nanostructure [17]. By comparing the results obtained with the two approaches, we also provided a method to confirm the values of forces calculated for the nanosensor.

Chapter 5

DNA origami force spectroscopy

5.1 DNA origami force spectroscopy

Single-molecule force spectroscopy techniques, such as magnetic tweezing, optical tweezing and atomic force microscopy, are widely used to study minute forces and mechanical properties of biomolecules and they are based on the attachment of the target molecule of interest to a micro-sized object. One of the main limitations of force spectroscopy is low data throughput, which is due to the serial nature of the technique itself. This problem has been solved by parallelizing the data acquisition step, as in magnetic tweezer experiments. Another limitation of force spectroscopy is the need for a tethering molecule between the sample and the micrometric object used to measure: this physical connector can cause drift and noise, thus affecting the measurements.

To overcome these shortcomings, Nickels et al. constructed a nanoscopic force clamp via DNA origami nanotechnology to study molecular interactions under mechanical forces [17]. The force clamp DNA origami is a nanodevice characterized by a rigid structure that supports a ssDNA filament behaving as an entropic spring (see paragraph 2.2.3 for the description of the mechanical properties of ssDNA). By adjusting the number of bases between the fixed anchor points of the rigid part, the contour length of the ssDNA can be changed, directly affecting the entropic force acting on the system under study.

The fixed distance between the two extremities of the ssDNA filament is imparted by the DNA origami and the given length of the ssDNA - which is prearranged in the origami design - provides an approximately constant force to the target molecule over time. The conformation change of the target molecule under mechanical forces was monitored with single-molecule Förster Resonance Energy Transfer (FRET). In their work, Nickels et al. applied the DNA origami nanoscopic force clamp to study the conformational exchange of a Holliday junction and the binding of a protein to a dsDNA under various mechanical forces. The results revealed that the DNA Holliday junctions had a preferential conformation when it is under a relatively strong force. The protein binding to the dsDNA was inhibited if a strong force was applied to stretch the dsDNA substrate, which indicated that the protein/DNA binding caused a mechanical force to bend the DNA.

To the purpose of measuring the unzipping force of a target hairpin directly inserted in a DNA origami nanostructure, we modified the original design by Nickels and coworkers in order to place the 24 bp long hairpin of the scaffold in the middle of the ssDNA spring region, as schematically illustrated in Figure 5.2. This was done with the aim of overcoming the problem of the unspecific interactions between the sample and the surface of the MT flow-cell, presented in paragraph 4.2. In the following paragraphs, I will describe the sample design and synthesis, with particular focus on the method to estimate the force applied on the target biomolecule. I will then summarize the basic principles of FRET necessary to understand the experimental data. The theoretical introduction is based on the book *Single-Molecule Technique: a Laboratory Manual* [18].

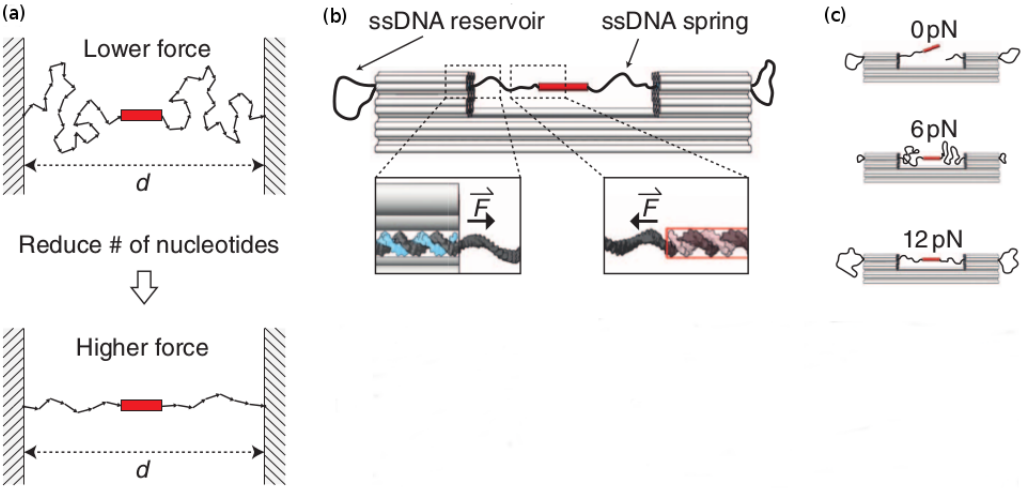

Figure 5.1: (a) Schematic representation of the entropic behaviour of ssDNA: if the number of nucleotides in the filament is reduced and the distance *d* between its extremities is kept constant, the entropic force to the target molecule (marked in red) increases. (b) A model of the force clamp DNA origami. The grey part represents the rigid origami structure, the black line the ssDNA filament and the red rectangle the target molecule. In a fixed design, the number of nucleotides in the ssDNA spring and thus the applied force are constant. (c) Three different variants of the force clamp origami applying forces of 0 pN, 6 pN and 12 pN. Image adapted from the work of Nickels et al. [17].

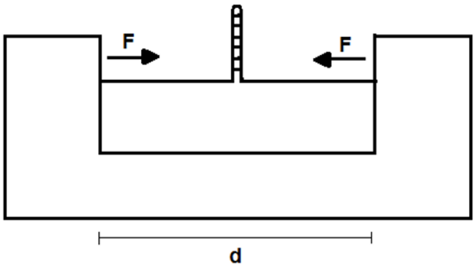

Figure 5.2: Schematic representation of the force clamp DNA origami with the ssDNA hairpin placed in the single-stranded region. The hairpin undergoes a force of respectively 1 pN, 12 pN or 20 pN depending on the length of the ssDNA filament. Image adapted from the paper of Nickels et al. [17].

5.2 Principles of Förster Resonance Energy Transfer

Single-molecule Förster Resonance Energy Transfer (smFRET) has been widely adopted by many laboratories around the world to study a variety of biological systems, including DNA, RNA, proteins and large macromolecular complexes.

FRET is a spectroscopic technique based on the mechanism of energy transfer from a light-sensitive molecule (or chromophore) which emits at short wavelengths - called donor- and a second chromophore which emits at longer wavelength - called acceptor. After light irradiation, the donor molecule is raised to its excited electronic state and normally it returns in its non-excited state with a radiative process that involves the emission of photons with less energy than the incoming ones. If the acceptor molecule is placed close to the excited donor, a transfer of energy from the donor to the acceptor through a non-radiative dipole-dipole coupling may occur. The subsequent return to the non-excited state causes the acceptor emission after the relaxation effect. If the two fluorophores are very close, all the energy is transferred from the

donor to the acceptor and the first is actually quenched. A schematic representation of this phenomenon is illustrated in Figure 5.3.
Apparent FRET efficiency is calculated as

$$E_{app} = \frac{I_A}{I_A + I_D}, \tag{5.1}$$

where I_A and I_D represent acceptor and donor intensities, respectively. E_{app} provides only an approximate indicator of the inter-dye distance because of uncertainty in the orientation factor between the two fluorophores and the required instrumental corrections. In order to determine actual FRET efficiency, the correction factor γ has to be estimated: γ accounts for the differences in quantum yield and detection efficiency between the donor and the acceptor and is calculated as the ratio of change in the acceptor intensity to change in the donor intensity upon acceptor photobleaching. Corrected FRET efficiency is then calculated using the following expression [75]:

$$E = \frac{1}{1 + \gamma I_D / I_A} \tag{5.2}$$

The efficiency of energy transfer E can be also expressed in terms of the donor-acceptor distance r as

$$E = \frac{1}{1 + (r/R_0)^6}, \tag{5.3}$$

where R_0 is called the Förster radius and is defined as the distance at which the FRET efficiency is 50%, *i.e.* both the donor and the acceptor emit light with the same intensity (see Figure 5.4). Since E is inversely proportional to the sixth power of the distance between donor and acceptor, FRET is highly sensitive to subnanometre distance modulations: for this reason, this technique is widely used in biology for measuring distances in the $30\,\text{Å} - 80\,\text{Å}$ range.
The Förster radius depends on the particular pair of chromophores: for our experiments, we used the FRET pair with cyanine dyes Cy3 and Cy5 characterized by $R_0 \approx 60\,\text{Å}$. The modulation of energy transfer is limited to a few nanometre around R_0, thus, FRET is not suitable for applications that demand to detect changes over long distances.
Ideal dyes for single-molecule fluorescence studies should possess as many as possible of the following characteristics:

- photostability, so that they emit millions of photons before photobleaching;
- brightness, *i.e.* they need to have a high extinction coefficient and quantum yield;
- little intensity fluctuation, at least in the timescale of interesting biological events under study;
- excitation and emission in the visible wavelengths;
- relatively small dimensions, so that they introduce minimum perturbation to the host molecule;
- commercial availability in a form that can be conjugated to biomolecules;
- appreciable overlap between donor emission and acceptor absorption, while large spectral separation in donor and acceptor emission, in order to minimize donor emission leakage into the spectral range of acceptor emission and to reduce the amount of direct excitation of the acceptor by the laser;
- comparable emission quantum yield for donor and acceptor, in order to guarantee clearly anticorrelated intensity changes of donor and acceptor.

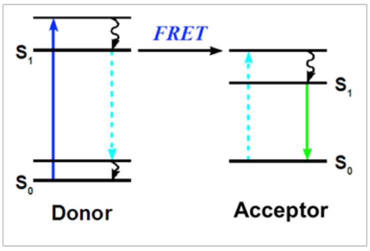

Figure 5.3: Representation of the electronic states of the donor and the acceptor molecules in a FRET configuration. S_0 is the non-excited state and S_1 is the excited state of the molecules. The continue and dotted arrows represent radiative and non-radiative emission phenomena, while the black curved arrows represent the relaxation effect.

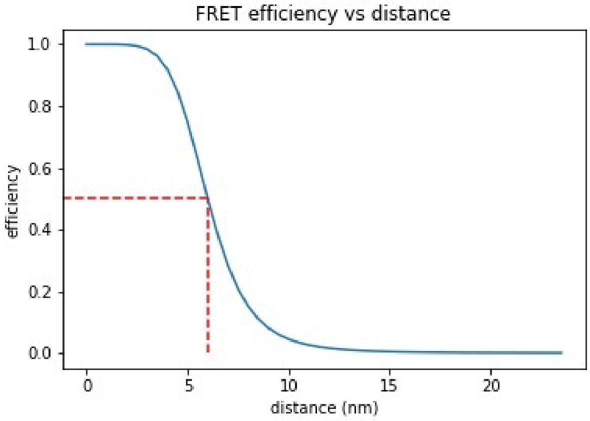

Figure 5.4: FRET efficiency *versus* gap distance in nanometers for the fluorophores pair Cyanine 3 and Cyanine 5 with $R_0 = 6\,\text{nm}$. The Förster radius R_0 is defined as the distance corresponding to a transfer efficiency of 50%.

5.2.1 Fluorophores optical properties

In our configuration, cyanine dyes Cy3 and Cy5 were respectively used as donor and acceptor. They were placed on the force clamp DNA origami in such a way that their distance alternated between 2 nm (zipped hairpin) and 24 nm (unzipped hairpin). Since the Förster radius of the cyanine dyes Cy3-Cy5 is $R_0 \approx 6\,\text{nm}$ [73], they could be profitably used to perform FRET experiments to detect the hairpin transition between the open and the closed states. The main optical properties of the Cy3 and Cy5 dyes are listed in table 5.1 below [77]:

Dye	**Excitation λ_{max}**	**Emission λ_{max}**	**Photostability**	**Quantum Yield**
Cy3 (donor)	550 nm	565 nm	91 s	4%
Cy5 (acceptor)	655 nm	667 nm	82 s	27%

Table 5.1: Optical properties of Cy3 and Cy5 dyes.

The photostability has been measured in Trolox, an antioxidant that was added to the buffer solution to reduce photobleaching during FRET experiments. The quantum yield has been measured in PBS.

The absorption and emission spectra of the fluorophores are shown in Figure 5.5.

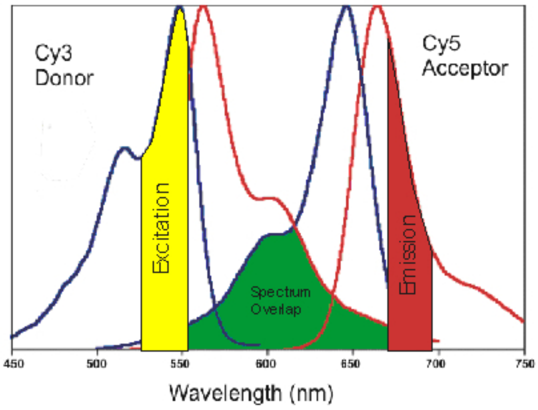

Figure 5.5: Absorption and emission spectra of the Cy3 and Cy5 dyes.

5.3 The force clamp DNA origami

5.3.1 Design and calculation of the force

From MT measurements, we expected the unzipping force of the ssDNA hairpin to be approximately 12 pN ± 1 pN. We then folded three distinct force clamps that differed for the contour length L_C of the ssDNA filament and thus for the resulting force, respectively of 1 pN, 12 pN and 20 pN. In the configuration where the entropic force is $F_{ssDNA} \approx 1\,\text{pN}$, the hairpin is supposed to be in its zipped state, because the force exerted by the ssDNA spring is not high enough to open it. On the contrary, when $F_{ssDNA} \approx 20\,\text{pN}$, we expect the hairpin to be in its unzipped configuration, because the entropic force is higher than the unzipping force. The system with $F_{ssDNA} \approx 12\,\text{pN}$ should be the intermediate case in which transitions between the zipped and the unzipped state are observed, because $F_{ssDNA} \approx F_{unzip}$. By placing two fluorophores at the neck of the target molecule, it is possible to detect the different hairpin conformations by measuring the FRET signal. In fact, when the two fluorophores are separated by $r \approx 2\,\text{nm}$ (*i.e.* the diametre of a dsDNA helix), the donor excitation results in an emission signal from the acceptor. On the opposite, when the hairpin is unzipped and the distance between the two fluorophores is $r \approx 24\,\text{nm}$, no transfer of energy from the donor to the acceptor should occur after donor excitation (for the dependence of the FRET efficiency on the interparticle distance see Figure 5.4 in the following section). The two different configurations - in which the hairpin is zipped or unzipped and the fluorophores are respectively at distances $r \approx 2\,\text{nm}$ and $r \approx 24\,\text{nm}$ - are schematically illustrated in Figure 5.6.
The novelty - but also the main difficulty - of our FRET measurements depends on the fact that, in the limiting cases in which the hairpin is either permanently zipped or unzipped, the corresponding FRET efficiency is constant and respectively equal to 1 or 0. Unlike standard FRET experiments, in which an external perturbation induces conformational changes within the same sample and hence variations in the position of the fluorophores, in our system, it was crucial to compare the resulting FRET signal in different versions of the force clamp origami. In this way, it was then possible to identify the correct unzipping force.

The force applied by the force clamp origami to the target molecule was evaluated on the basis of the modified freely-jointed chain (mFJC) model with stretchable Kuhn lengths for the force-extension behaviour of ssDNA [71]:

$$x(F) = L_C \left[\coth\left(\frac{Fl_K}{k_B T}\right) - \left(\frac{k_B T}{Fl_K}\right) \right] \left(1 + \frac{F}{S}\right),$$

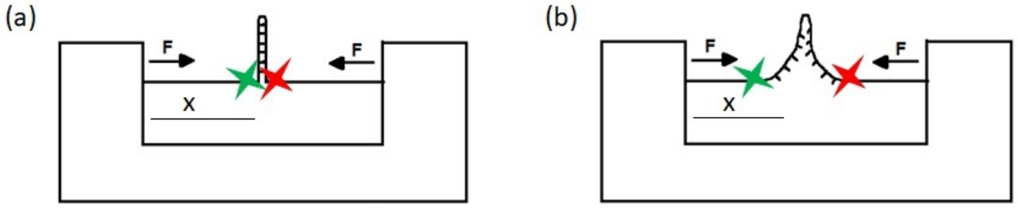

Figure 5.6: Schematic representation of the force clamp DNA origami with the addition of the two fluorophores for FRET signalling. (a) When the hairpin is closed, the distance between the two fluorophores approximately equals the diameter of a dsDNA helix ($r \approx 2\,\text{nm}$), so FRET can be observed. (b) When the hairpin is open, the distance between the two fluorophores is too large to allow any transfer of energy between the donor and the acceptor after excitation of the donor.

where $L_C = Nl_B$ is the contour length of the ssDNA, F the applied force, l_K the Kuhn length, k_BT the thermal energy at room temperature and S is the stretch modulus and x is the end-to-end distance between the two extremities of the ssDNA filament. We calculated the end-to-end distance as

$$x = \frac{d}{2} - l_{fluorophores},$$

where d is the fixed distance between the two anchor points of the ssDNA string, determined by the origami design, and $l_{fluorophores} = 20$ bp is the length of the fluorophores-modified staples (see Figure 5.6). In fact, the binding of the Cy3- and Cy5-staples to the ssDNA region of the force clamp results in the formation of two dsDNA filaments on both sides of the hairpin: we can then consider each single-stranded part independently and approximate them with two different entropic springs, each applying the same force to the target hairpin. On the basis of this model, the length of the ssDNA filament L_C necessary to apply the desired forces was evaluated by using the values listed in the following table:

Parameter	**Value**
x	14.62 nm
l_B	6.3 ± 0.8 nm
l_K	1.5 nm
k_BT	4.11 pN nm
S	800 pN

Table 5.2: List of the parameters used to estimate the force exerted by the force clamp DNA origami by referring to the modified Freely Jointed Chain model for the ssDNA spring.

The trend of the force applied by the force clamp as a function of the number of nucleotides $N = L_C/l_B$ is represented in Figure 5.7. The dashed-lines refer to the force calculated for values of l_B within one standard deviation from the average (see parameters listed in Table 5.2). By propagating the error on the ssDNA-base-length, we can calculate the uncertainty in the estimation of the force. The relative error of the force is plotted in Figure 5.8 as a function of N: the graph shows that the relative error is non-linear with respect to N and that the mFJC model is more accurate to predict the behaviour of low-force DNA origami structures.

5.3.2 Synthesis and TEM characterization

To fold the force clamp DNA origami, we set up a synthesis reaction with the reagents listed in Table 5.3:

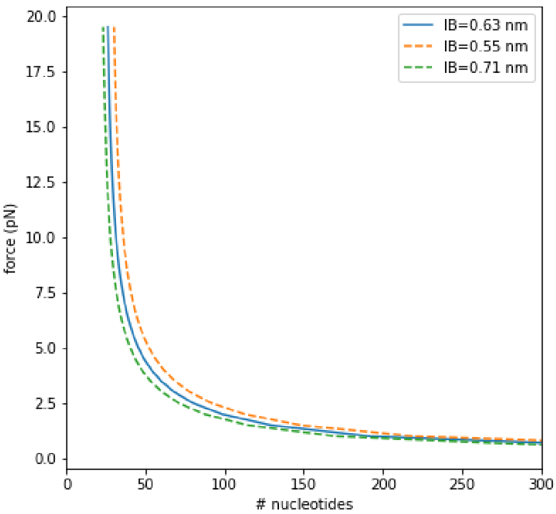

Figure 5.7: Plot of the force applied by the force clamp DNA origami as a function of the number of nucleotides in the ssDNA semi-filament. The force has been estimated by using Eq. (5.3.1) and the function has been calculated for different values of l_B, within one standard deviation from the average value.

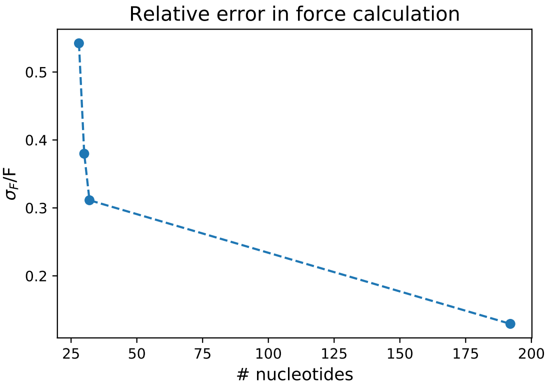

Figure 5.8: Determination of the force relative error as a function of the number of nucleotides in the ssDNA region.

Reagent	**Final concentration**
Scaffold (p7249)	10 nM
Staples	100 nM
$MgCl_2$	20 mM
50× TAE	1×
H_2O	

Table 5.3: Synthesis reaction for the force clamp DNA origami.

The solution was first heated up to 65 °C to denature the scaffold, then it was progressively led to a final temperature of 25 °C in 16 h to allow the staples to bind to the scaffold. After synthesis, gel electrophoresis was used to get rid of excess staples: when loaded in a 1.5% agarose gel, folded samples migrate more slowly than free staples, so they can be easily separated. After running the gel at 70 V for 2 h, the band corresponding to the folded origami was cut out.

The origami were extracted by squeezing the band with a glass slide coated with Parafilm, in order to induce a transition from the gel-like to the liquid configuration of the band itself. Gel electrophoresis analysis also confirmed the correct synthesis of a statistically relevant amount of origami (see Figure 5.9).

In order to perform FRET experiments, 50 × excess of fluorophores (Cyanine 3 and Cyanine 5) was added to the unpurified sample at room temperature and left in incubation overnight. A not-stained 0.7% agarose gel was then run at 70 V for 2h to get rid of excess staples and fluorophores. The sample was then imaged with a camera with suitable visible-filters to detect the Cyanine 3 (Cy3) and the Cyanine 5 (Cy5) dyes and to confirm effective binding to the structures. The bands were finally cut and squeezed to extract the force clamp origami. The purified solution was stained for 1 min with Uranyl Formate on a TedPella copper grid and then imaged with the TEM (see Figure 5.10). The different variants of the force clamps did not show any significant difference between themselves when observed at the TEM.

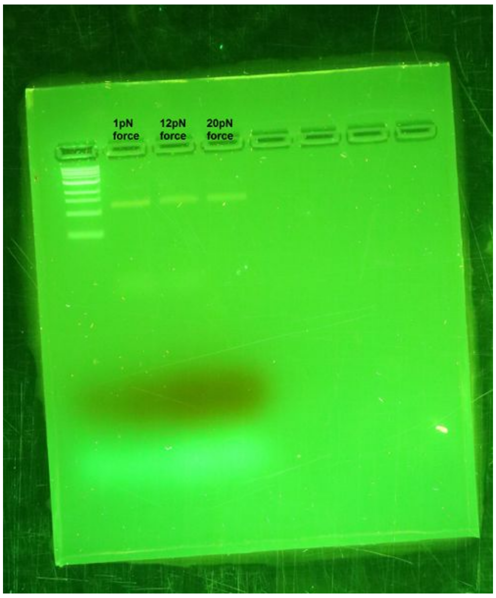

Figure 5.9: 1.5 % agarose gel for purification of the force clamp DNA origami. Thin lanes correspond to correctly folded origami. Broad lanes correspond to excess staples or unfolded origami.

5.4 FRET experimental setup

smFRET time trajectories are most commonly acquired by imaging surface-immobilized molecules with the aid of total internal reflection (TIR) microscopy that allows high throughput data sampling. In TIR microscopy, an evanescent field of excitation light with a penetration depth of $d \approx 100 - 200\,\text{nm}$ is created, so that the background fluorescence is greatly reduced. There are two types of TIR, prism type (PTIR) and objective type (OTIR).

In PTIR, an inverted microscope is adapted to hold a fused silica prism on top of the sample channel and the fluorescence is collected from the objective below. After the incident laser beam is focused using a long focal length lens, it enters the prism, passes through refractive index matching oil and is internally reflected at the quartz-water interface. The fluorescence signal is collected using a long working distance water immersion objective. A PTIR is necessary for fluid injection experiments because its imaging surface - a 1 quartz slide - does not bow upon pressure change during flow.

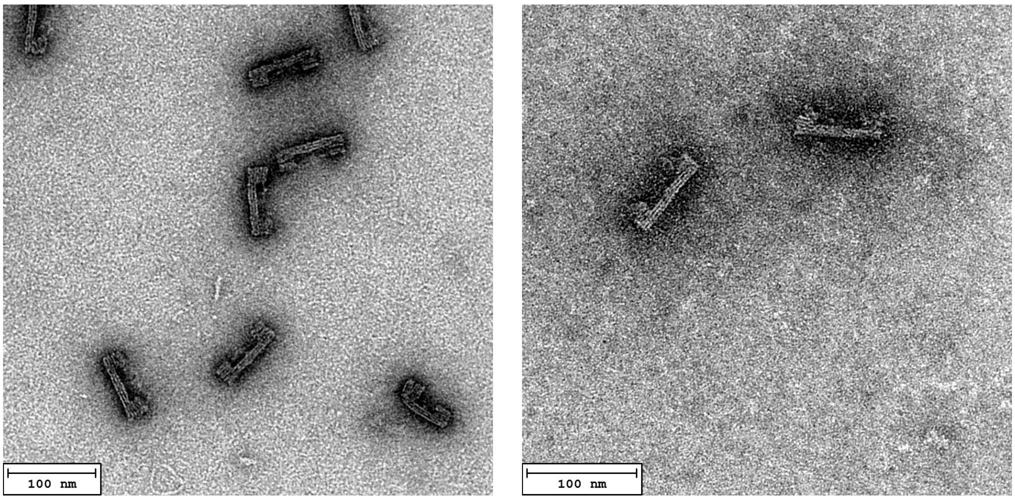

(a) 1 pN force clamp DNA origami **(b)** 12 pN force clamp DNA origami

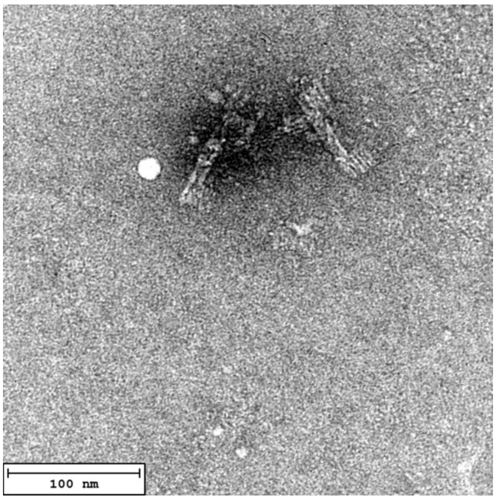

(c) 20 pN force clamp DNA origami

Figure 5.10: Representative TEM images of force clamp DNA origami apt to apply forces of 1 pN, 12 pN and 20 pN respectively. The force clamp DNA origami were previously stained with Uranyl Formate.

OTIR relies on using a high numerical aperture oil objective to create an evanescent field. Focusing the beam at the back focal plane generates a parallel beam exiting the objective and then translating it to the periphery of the objective produces TIR at the glass/water interface. Fluorescence from the molecules tethered to the coverslip surface is collected using the same objective. OTIR has higher photon collection efficiency with respect to PTIR. In our setup, we used a 100 × magnification objective lens.

The setup used for our FRET experiments is illustrated in Figure 5.11. A green (512 nm) and a red laser (660 nm) were focused on a small area of the sample (A $\approx$ 82 $\times$ 82 µm). Donor and acceptor fluorescence emission were split using a dichroic mirror. By adjusting an offset with the dichroic and an additional mirror, both donor and acceptor emission can be imaged side by side on the CCD camera. A fast frame transfer electron-multiplying charged coupled device (EM-CCD) camera was used for imaging: EM-CCDs are characterized by high quantum efficiency (85-95%) in the visible range, low effective readout noise (< 1 electron rms) even at the fastest readout speed ($\geq$ 10 MHz), fast vertical shift speeds ($\leq$ 1 µs row^{-1}, to achieve faster frame rates) and a low multiplication noise. Using a 512 $\times$ 512 px EM-CCD, we could acquire data at 10 Hz at full frame.

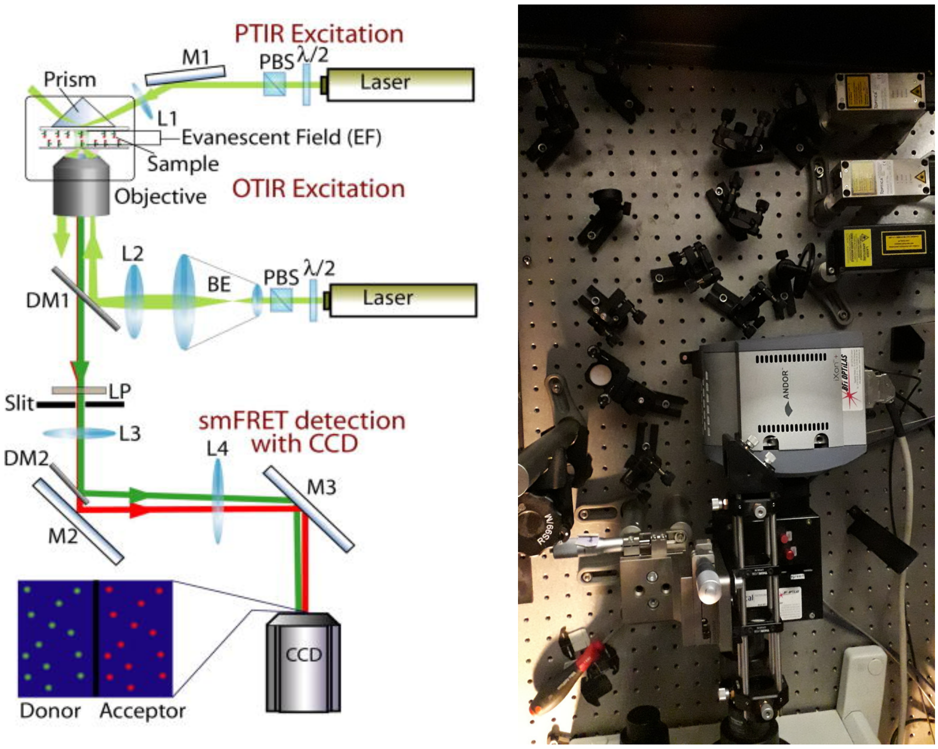

(a) Schematic representation of the FRET setup, adapted from [73]

(b) Picture of the experimental FRET setup employed for our measurements.

Figure 5.11: Schematic for TIR single-molecule FRET setup.

5.4.1 Sample chamber preparation and data acquisition

The sample chamber was created by attaching a pre-cleaned channel slide to a coverslip with double-sided tape 5.12. Simple pipetting through two holes pre-drilled in the slides allowed the exchange of solution without drying. The chamber was filled with a buffer solution made up of 5 mM Tris-HCl, 10 mM $MgCl_2$, $1\,mg\,mL^{-1}$ EDTA and 0.05 % Tween20 and then was passivated with a Streptavidin solution ($0.5\,mg\,mL^{-1}$ of Streptavidin in a 10 mM Tris-HCl, 100 mM NaCl, and 0.05 % Tween20 buffer). 100 µL of a 100 pM solution of biotinylated DNA origami was incubated for 20 min in the sample chamber. An oxygen scavenger solution containing protocatechuic acid, protocatechuate-3,4-dioxygenase and Trolox was added 1 h before measuring to improve dyes stability and reduce photobleaching.

The sample was first imaged separately with the green and the red lasers to verify fluorescence emission and detection from both donor and acceptor. An additional control test was also performed in order to confirm that the fluorescence signal observed in the red region was not caused by bleed-through from the green laser. By illuminating the sample with the green laser and by placing a green filter along the red laser path, we expected to filter out the emission signal from the acceptor and then to record only potential leakage from the green laser. Since the observed screen was black, we could confirm that the signal detected after the short-wavelength path was only due to FRET emission.

The donor and the acceptor signals were acquired while irradiating the sample with the green laser working at P=30 mW. The framerate for data acquisition was 1 ms^{-1}. Since the laser wavelength was $\lambda = 512\,\mathrm{nm}$, in this experimental configuration the donor molecule was excited in correspondence of its lowest peak (see Figure 5.5).

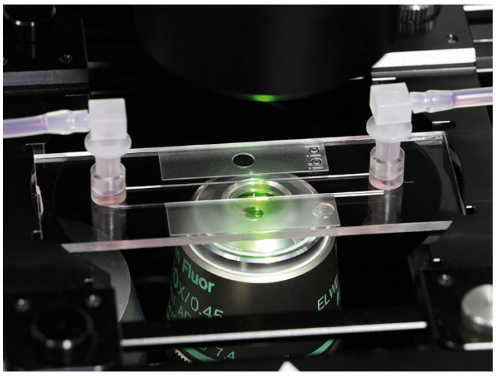

Figure 5.12: Sample chamber made up by a channel slide and a coverslip, placed above the objective lens for FRET experiments.

5.5 Data analysis

The acquired FRET traces were analyzed with the open-source iSMS software [78], based on a MATLAB script. The raw movies of the donor and the acceptor emission signals are loaded into the program and then the green and red ROIs (Region-Of-Interests, i.e. emission channels) in the raw image have to be aligned manually, by identifying overlapping peaks in both channels (see Figure 5.13). The iSMS software automatically finds the fluorophores peaks above the desired intensity threshold and then identifies FRET pairs when the donor and the acceptor signals are positioned within a certain radius (see Figure 5.14). By clicking on the corresponding icon, the donor and acceptor traces can be displayed, together with the corresponding raw efficiency (see for instance the traces in Figure 5.15).

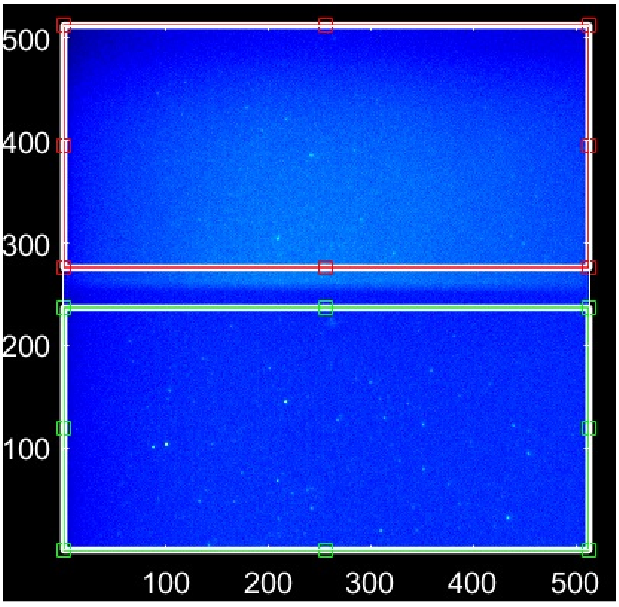

Figure 5.13: Image of the green (bottom) and the red (top) emission channels as they appear in the iSMS program. The dimensions of the ROIs can be regulated manually by identifying corresponding peaks in both regions.

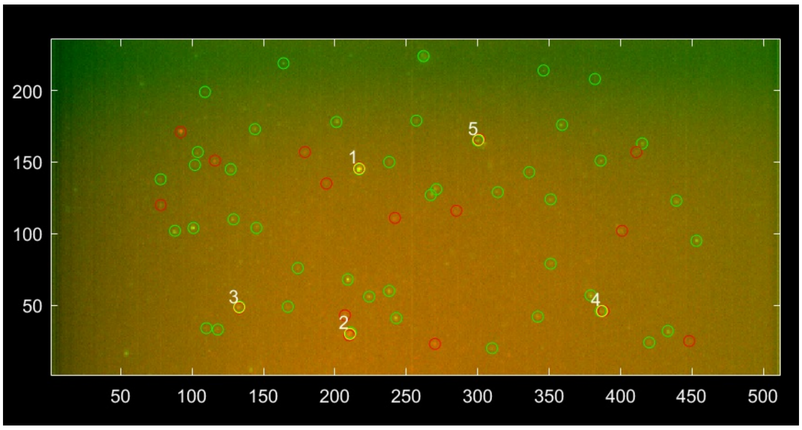

Figure 5.14: Image of the donor (green) and the acceptor (red) peaks found by the iSMS software, after setting a suitable intensity threshold. FRET pairs are automatically identified from the distance between all donor and acceptor peaks and are marked in yellow.

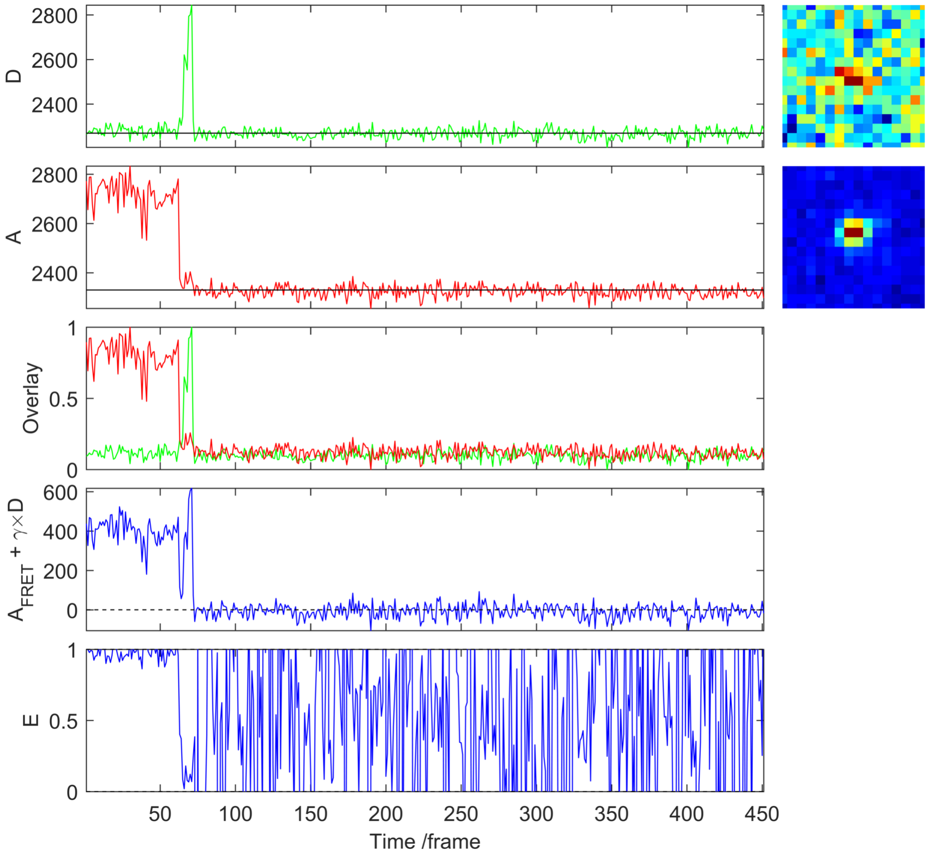

Figure 5.15: Representative image of the donor (green) and the acceptor (red) emission signals as they are calculated by the iSMS software. The program automatically computes also the stoichiometry and the efficiency of the FRET-process. In the upper right corner, the donor and the acceptor spots at time t=0 are shown. In this picture, it is possible to see that photobleaching of both the donor and the acceptor occurs after $\approx$ 80 frames.

We analyzed hundreds of donor and acceptor traces of both samples, the 1 pN force clamp and the 12 pN force clamp, and we calculated the corresponding efficiency. For the 1 pN-force DNA origami, the FRET efficiency was almost constant over time and it was $E > 50\%$. Since the relative error in the estimation of the force for the 1 pN case is $\sigma_F/F \approx 0.1$ (see σ_F/F for $N = 200$ in Figure 5.8) and since this force is not sufficient to unzip the hairpin, we can conclude that the calculated efficiency $E > 50\%$ corresponds to a closed conformation of the ssDNA hairpin. The representative plots of the donor and acceptor signals and of the corresponding efficiency are illustrated in Figure 5.16. We only showed the traces for times $t < t_{bleaching}$.

The case of the 12 pN force clamp is more complex to be analyzed as the relative error in the force calculation is $\sigma_F/F \approx 0.3$, and the forces within this range are compatible with both a zipped and an unzipped configuration of the hairpin. Moreover, since the entropic force is close to the expected unzipping force, we did expect to observe several transitions between the two states.

The large majority of samples were characterized by a FRET efficiency $E \approx 10\%$, thus indicating a large interparticle distance between the fluorophores ($r > 6\,\text{nm}$), which is compatible with an unzipped configuration of the hairpin. A representative image of the donor and acceptor signals and the corresponding FRET efficiency is reported in Figure 5.17. The donor emission is always higher than the acceptor one for times $t < t_{bleaching}$ (at $t_{bleaching} \approx 3800$ ms also the donor signal drops off to zero): this means that the donor excitation by laser illumination does not result in any transfer of energy to the acceptor.

Figures 5.18, 5.19 and 5.20 represent a few cases in which a transition between the zipped and the unzipped configurations of the hairpin is observed. The donor and the acceptor signals are indeed anti-correlated and the resulting FRET efficiency switches between 1 and 0, thus indicating a sudden change in the interparticle distance.

The results obtained from FRET experiments are consistent with those found for MT measurements. In both cases, at low forces, the hairpin is zipped and no transition between the open and the closed states are observed. When the force approaches $F = 12\,\text{pN}$, both techniques reveal a change in the end-to-end distance of the biomolecule and this observation suggests that the unzipping force for the 24-bp hairpin in the scaffold of the origami is $F = 13 \pm 1\,\text{pN}$.

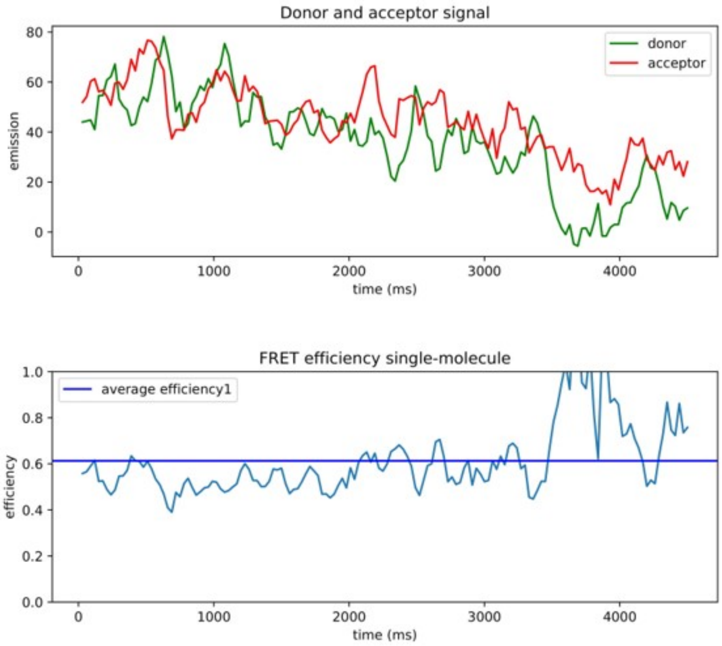

Figure 5.16: Donor and acceptor signal for the 1 pN version of the force clamp DNA origami. The corresponding FRET efficiency is nearly constant ($E \approx 60\%$), thus revealing a stable zipped configuration of the ssDNA hairpin.

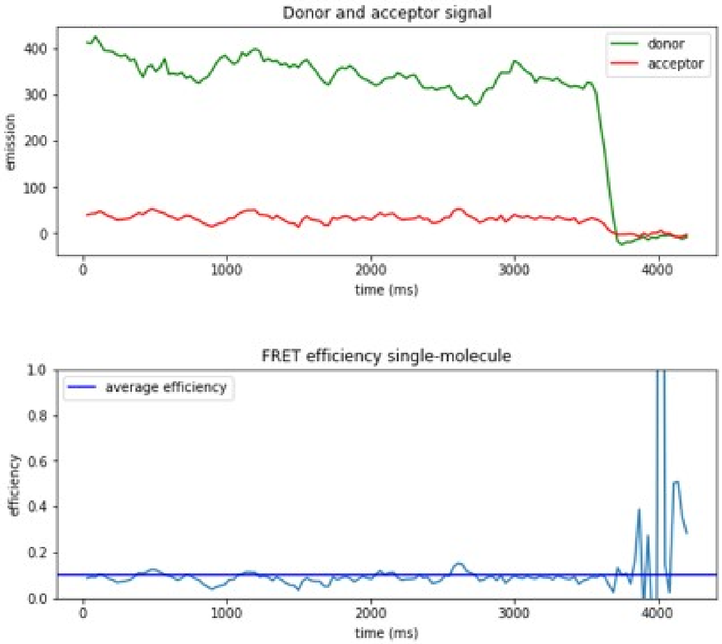

Figure 5.17: Donor and acceptor signal for the 12 pN version of the force clamp DNA origami. In this sample, the FRET efficiency is low ($E \approx 10\%$), thus indicating an unzipped configuration of the ssDNA hairpin.

Figure 5.18: FRET signal for the 12 pN force clamp switching between high and low efficiency, thus indicating a transition between the zipped and the unzipped configuration of the hairpin.

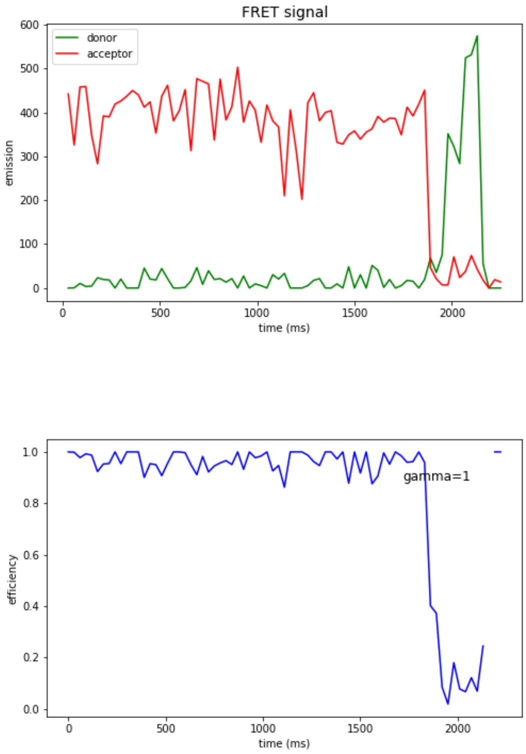

Figure 5.19: FRET signal for the 12 pN force clamp switching between high and low efficiency, thus indicating a transition between the zipped and the unzipped configuration of the hairpin.

5.6 Force clamp DNA origami with a 10 nm AuNP

FRET experiments confirmed that our new version of the force clamp DNA origami can apply controlled tensions to the target ssDNA hairpin. After validating the correct functioning of the nanodevice, we finally modified the structure by attaching a single 10 nm AuNP to the ssDNA filament in the proximity of the hairpin (see Figure 5.21). In this way, we provided our force sensor with a local heating source that could induce local temperature variations in plasmon resonance conditions.

To the purpose of folding the AuNP-modified force clamp, we synthesized the origami as explained in paragraph 5.3.2. After sample purification, we mixed the DNA origami with a 10 × excess of 10 nm AuNPs previously functionalized with the ssDNA filament complementary to the sequence of oligonucleotides located immediately before the target hairpin.
The ssDNA staples were bound to the nanoparticles by following the protocol presented in the paper of B. Liu and J. Liu [58]. According to this method, the DNA attachment to the AuNPs is driven by freezing. A mixture containing 1 mL of 10 nm AuNPs taken from Sigma stock solution (optical density OD=1) and 25 µL of 100 µM thiolated oligonucleotides was then frozen at $-20\,^{\circ}\mathrm{C}$ for 2 h. After thawing the solution, the mix was centrifuged for 10 times by using 100 kDa Amicon filters to remove excess oligos, that could prevent correct binding of the particles to the origami.
The solution containing both the origami and the functionalized AuNPs was left in incubation

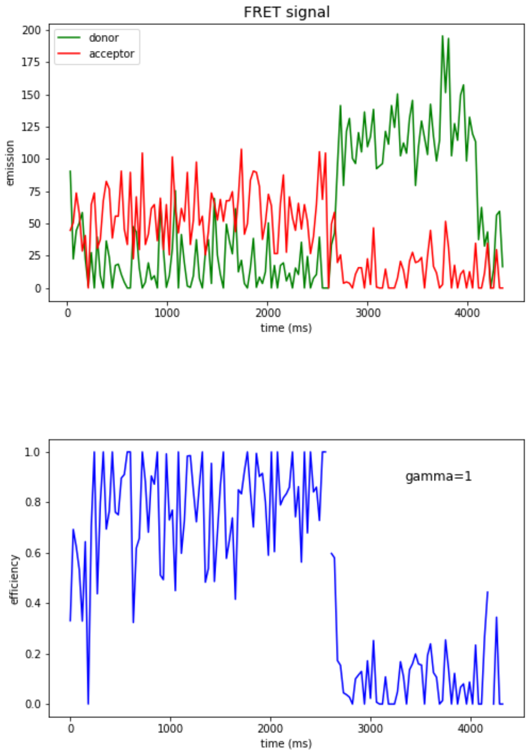

Figure 5.20: FRET signal for the 12 pN force clamp switching between high and low efficiency, thus indicating a transition between the zipped and the unzipped configuration of the hairpin.

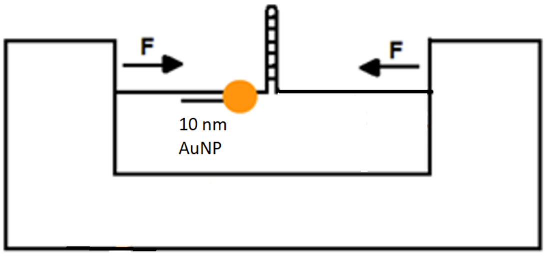

Figure 5.21: Scheme of the force clamp DNA origami with a single 10 nm AuNP.

for 2 hours at room temperature to let the AuNPs reach the corresponding binding site. After incubation, gel electrophoresis was used to separate excess particles from nanoparticles attached to the origami. A 1% agarose gel, stained with SYBR Safe solution, was imaged under a UV filter to find the band corresponding to the force clamps. The band was then cut and squeezed to extract the structures. The sample was stained with Uranyl Formate and imaged at the TEM to check the correct assembly of the particles to the origami. A representative TEM picture of the 1 pN force clamp origami decorated with a single 10 nm AuNP in the single-stranded region is illustrated in Figure 5.22. TEM analysis confirmed the successful outcome of the functionalization process.

Since gel analysis and TEM imaging confirmed the correct attachment of the 10 nm AuNPs

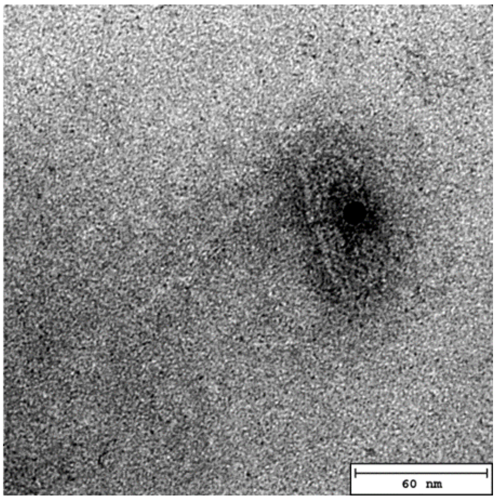

Figure 5.22: Representative TEM picture of a 1 pN force clamp DNA origami with a 10 nm AuNP attached to the single-stranded filament at the neck of the hairpin. The force clamp DNA origami were previously stained with Uranyl Formate.

to the force clamp origami, we succeeded in creating a new version of the force sensor DNA origami which is not only able to apply controlled tension to the target ssDNA hairpin formed in the scaffold, but also to induce precise temperature variations. In fact, by illuminating the AuNP with a laser characterized by the correct plasmon resonance frequency, local heating can be induced. The resulting temperature increase will then affect both the melting temperature of the hairpin (*i.e.* its unzipping force) and the entropic force of the ssDNA filament, thus changing the effective force. By combining these two effects, it will be then possible to influence the dynamical properties of the target biomolecule, as intended by our research project.

Chapter 6

Nanoscale heating of laser irradiated gold nanoparticles

6.1 Heat generation with gold nanoparticles

In recent years, the investigation on plasmons and their interactions in nanoparticle (NP) systems have emerged as a promising area of research with potential applications in spectroscopy, chemical and biological sensing and nanophotonics. Constituent nanostructures range from isolated metal nanospheres to dimers, clusters and ordered arrays. DNA origami promises a simple and cost-effective method to implement plasmonic devices with exceptional ability to control the 3D NP arrangement at nanometer-scale resolution via self-assembly. This approach has been used to generate a variety of structures ranging from DNA origami bundles to template linear NP arrays to DNA origami-NP composites with elaborate geometries. [14].
Plasmons are quasi-particles arising from strong light-matter interactions in metal: in this regime, coherent combinations of the electronic and photonic wave functions are created and they are defined as plasmons. Localized surface plasmons on metallic NPs, such as AuNPs, resonate at visible or infrared frequencies upon interaction with electromagnetic radiation. Surface plasmon resonance (SPR) creates a localized electric field near the particle surface that enhances the absorption and scattering of incident radiation. The absorption of this high energy radiation induces electron-phonon and phono-phonon lattice vibrations and the dissipation of lattice vibrations results in heating of the surrounding medium on the time-scale of micro-second. This conversion of light energy to heat energy by plasmonic NPs is known as the thermoplasmonic effect. The heat induced by the laser-irradiated metal nanoparticles leads to an increment in temperature that decays as the inverse of the distance from the nanoparticle, so the generated heating is considered to be localized near its source[90].
In this chapter, I will briefly explain the basic principles of plasmon formation and heat generation in AuNPs and then I will present the experimental data regarding the study of temperature increase on the surface of 20 nm AuNPs as a function of the light flux. The measurements were done on clusters of DNA-mediated AuNPs that were illuminated with a laser tuned at the SPR frequency and provided a calibration of the laser power and the irradiation time necessary to induce local heating. In this simple arrangement, the dsDNA dehybridization process was used as a probe of effective heating and the results were affected by the collective effect due to the presence of multiple NPs. Therefore, to the purpose of studying the thermoplasmonic effect at the single-particle level, a more complex configuration had to be designed. This different scheme exploited the unique property of the DNA origami technique to position AuNPs with nanometer precision and was intended to use the zipping/unzipping dynamics of a ssDNA hairpin as a probe. In fact, we planned to include the ssDNA hairpin in a rigid DNA origami nanostructure and to place a single 20 nm AuNP in the proximity of the target biomolecule.

6.1.1 Interaction between light and metal nanoparticles: plasmon formation

The response of metals to an incident electric field can be described with the Drude model, based on the Maxwell's equations [79], [80], [81]. In this approximation, the electrons in the metal are considered as free electrons that can move against a background of positive, fixed ions. The Drude model neglects any interactions between ion and electrons and any long-distance interactions between the electrons, and it takes into account only the instantaneous collisions between the free electrons, that are characterized by the collision frequency γ. Based on these hypothesis, the motion of a free electron of mass m and charge e exposed to an external electric field $\mathbf{E}$ is described by the following equation:

$$m\ddot{\mathbf{x}} + m\gamma\dot{\mathbf{x}} = -e\mathbf{E}. \tag{6.1}$$

The electric field associated with a light beam has an harmonic time dependence $\mathbf{E}(t) = \mathbf{E_0}e^{-i\omega t}$, so we can make the ansatz that the electron displacement is also in the form of $\mathbf{x}(t) = \mathbf{x_0}e^{-i\omega t}$. We can then solve the equation of motion to find that

$$\mathbf{x}_0 = \frac{e\mathbf{E}_0}{m\omega(\omega + i\gamma)} \tag{6.2}$$

and we can use this result to calculate the polarization generated in the medium by the electrons displacement $\mathbf{P} = -Ne\mathbf{x}$, where N is the density of free electrons. We then get that

$$\mathbf{P} = -\frac{Ne^2\mathbf{E}}{m\omega(\omega + i\gamma)}. \tag{6.3}$$

Since the dielectric displacement of charges is $\mathbf{D} = \epsilon_0\mathbf{E} + \mathbf{P} = \epsilon_0\epsilon_r\mathbf{E}$, it can be shown that the dielectric constant of the medium is

$$\epsilon_r(\omega) = 1 - \frac{Ne^2}{m\epsilon_0\omega(\omega + i\gamma)} = 1 - \frac{\omega_P^2}{\omega^2 + i\gamma\omega}, \tag{6.4}$$

where $\omega_P = \sqrt{\frac{Ne^2}{\epsilon_0 m}}$ is the plasmon frequency of the material. The dielectric function describes the metal's response to an external electric field and depends on the frequency ω of the incident field.

To understand the physical meaning of the plasmon frequency, it is necessary to consider the propagation of electromagnetic waves in metals [80], [81]. According to Maxwell's equations, in a source free region ($\rho = 0$) the gradient of the charge displacement is null: $\nabla \cdot \mathbf{D} = 0$. This condition is verified if

$$\epsilon(\omega) = 0, \tag{6.5}$$

or if

$$\nabla \cdot \mathbf{E} = \check{\ } \cdot \mathbf{E} = 0. \tag{6.6}$$

We can decompose the electric field in its longitudinal and its transversal components $\mathbf{E} = \mathbf{E}_L + \mathbf{E}_T$, where by definition $\nabla \cdot \mathbf{E}_T = 0$ and $\nabla \times \cdot \mathbf{E}_L = 0$. In this way, it is easy to see that the first solution is valid for a longitudinal field, while the second one is valid for a transversal field. Therefore, in the case $\mathbf{E} = \mathbf{E}_L$, eq. 6.5 leads to

$$\epsilon_r(\omega) = 1 - \frac{\omega_P^2}{\omega^2 + i\gamma\omega} = 0, \tag{6.7}$$

which is verified for $\omega = \omega_P$ in a lightly damped system ($\gamma = 0$). Plasmon oscillations are then longitudinal waves generated by the collective oscillations of the free electrons in the metal with frequency $\omega = \omega_P$ in the condition $\epsilon_r = 0$ and in the small damping approximation.

When a metal is exposed to an electric field, it also undergos interband transitions, *i. e.* promotions of electrons to higher bands by absorption of photons at the correct energy. The total dielectric function is then made by two terms, the first one calculated with the Drude model

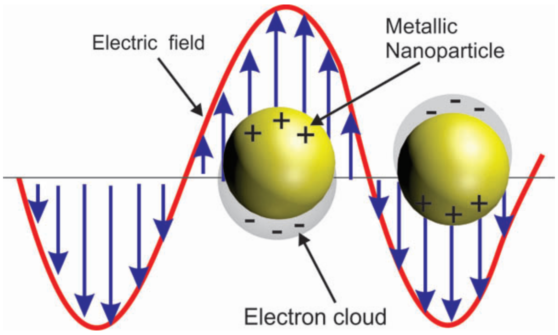

Figure 6.1: Schematic representation of the oscillations of the electrons in a AuNP exposed to an incident electric field.

($\epsilon_D = \epsilon_r$ in Eq. 6.4) and the second one referring to interband transitions (ϵ_{ib}) [91]. We can then write

$$\epsilon(\omega) = \epsilon_1(\omega) + i\epsilon_2(\omega) = (\epsilon_{D1} + \epsilon_{ib1})(\omega) + i(\epsilon_{D2} + \epsilon_{ib2})(\omega), \tag{6.8}$$

where ϵ_1 and ϵ_2 are respectively the real and the imaginary part of the dielectric function.

6.1.2 Plasmon formation in metal nanoparticles

When the size of the material becomes smaller than the wavelength of the exciting light, electron oscillations cannot propagate in the material due to the small size of the particle. The oscillation becomes therefore localized; hence the name localized surface plasmons. Typical objects that can sustain this kind of plasmons are metallic nanospheres and nanoellipsoids (see Figure 6.1). The response of a metal nanosphere with radius R to an external electric field $\mathbf{E}_0$ with wavelength λ can be calculated in the quasi-static approximation under the assumptions that $R << \lambda$ (static field) and that the electric field inside the particle is uniform. By exploiting the spherical symmetry of the system and by imposing the continuity of the field at the interface, it is possible to calculate the electric potential inside (ϕ_{in}) and outside (ϕ_{out}) the particle. It can thus be shown [80] that the internal electric field is approximated by the following equation:

$$\mathbf{E}_{in}(\omega) = -\frac{3\epsilon_m}{\epsilon + 2\epsilon_m}\mathbf{E}_0, \tag{6.9}$$

where ϵ is the dielectric function of the NP and ϵ_m is the dielectric function of the embedding medium.
The condition of excitation of the surface plasmon resonance is then verified for

$$\epsilon_1(\omega) = -2\epsilon_m. \tag{6.10}$$

By substituting the expression of ϵ_1 from Eq. 6.4 and 6.8, it is possible to calculate the surface plasmon resonance (SPR) frequency for a metal nanoparticle:

$$\omega_{SPR} = \sqrt{\frac{\omega_P^2}{1 + 2\epsilon_m + \epsilon_{ib1}} - \gamma^2}. \tag{6.11}$$

The SPR frequency thus depends on the characteristics of the NP through the parameters ω_P and γ and on the properties of the external medium through the function ϵ_m.

When a metallic nanoparticle is illuminated with a laser tuned at the resonance frequency, localized surface plasmons are excited and the free electrons start scattering on phonons, other electrons, and defects of the crystal lattice. Such scattering causes the damping of plasma oscillations that leads to heating of the NP with subsequent transfer of heat to the surrounding medium.

Since metal NPs have a very low light emission quantum yield, almost all the absorbed light energy is conversed to the heat energy. Heat transfer in any plasmonic NP system can be described by the following equation:

$$\rho(\mathbf{r})c(\mathbf{r})\frac{\partial T(\mathbf{r},t)}{\partial t} = \nabla k(\mathbf{r})\,\nabla T(\mathbf{r},t) + Q(\mathbf{r},t), \tag{6.12}$$

where T is the temperature profile as a function of the coordinate r and the time t; ρ, c and k are the mass density, the specific heat, and thermal conductivity, respectively, and Q is the local heat intensity. Q can be defined as the time integral of the incident electric field and the absorption cross-section area as follows:

$$Q(\mathbf{r},t) = \int_{t_{start}}^{t_{end}} I_0(t)\, C_{abs,NP}(\lambda_{NP})\, dt, \tag{6.13}$$

where I_0 is the temporally dependent intensity of the electric field and $C_{abs,NP}(\lambda_{NP})$ is the absorption cross-section area at the excitation wavelength.

Several experiments have been performed to estimate the temperature increase at the surface of gold nanoparticles (AuNPs) by using DNA molecules as probes. Typically, two different types of illumination have been employed for thermoplasmonic excitation: continuous and pulsed. Continuous illumination results in a steady-state temperature profile because the time-scale of continuous wave (CW) sources is longer (seconds) than the transient non-equilibrium regime, whereas pulsed sources (femto- to nano- seconds) may generate non-equilibrium behaviors. For instance, J. Stehr et al. [82] used DNA bound-AuNPs aggregates as light absorbers to locally convert optical energy from 300 ns laser pulses into thermal energy; the thermal energy melted the dsDNA on a microsecond time scale, thus disintegrating the aggregates on a millisecond time scale. In this way, they showed that DNA bound-AuNPs clusters could be profitably used as spectral reporter of DNA melting that allows for the discrimination of different targets for diagnostic applications. L. Poon et al.[83] developed a method to efficiently elicit the release of ssDNA from AuNPs by photothermal dehybridization of a thiolated duplex in response to pulsed laser irradiation for therapeutical purposes. They then managed to control the local temperature at the surface of the NPs in the range between the melting temperature of the dsDNA linked to the AuNP and the temperature of the cleavage of the Au-S bond. In a following work [84], F. Thibaudau reported results on ultrafast photothermal relase of DNA from AuNPs: he showed that dehybridization of dsDNA anchored to a AuNP surface could be achieved with a single laser pulse, leading to the release of ssDNA in solution. Also in this case, temperature control during laser irradiation was fundamental, as the local temperature needed to be lower than the one for breaking the Au-S bond anchoring the duplex (in fact non-functionalized AuNPs are not stable in solution). A similar approach has been followed also by H. Asanuma et al. in their paper of 2013 [86]. The authors demonstrated that laser-induced plasmonic heating can locally and selectively dehybridize DNA double helices in solution without damaging the gold nanostructures, *i.e.* by avoiding the breakage of the gold-sulphur bond. Thanks to the possibility to control the melting temperature and the consequent dehybridization process by tuning the laser wavelength and power, interesting applications in gene sequences and DNA nanotechnology were envisioned.

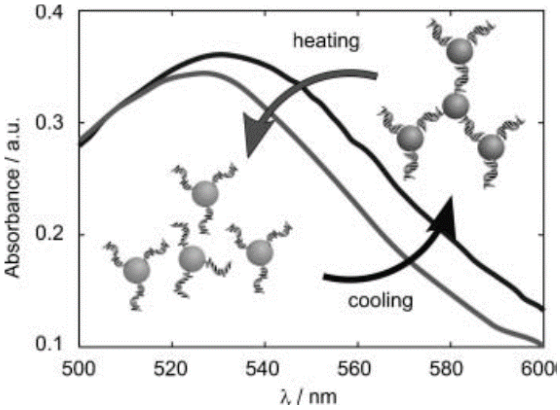

Figure 6.2: Shift of the SPR frequency peak as a consequence of DNA dehybridization and cluster disaggregation, as shown in the work of Reisman and coworkers [93].

6.2 DNA dehybridization induced by laser illumination

We tried to calibrate the temperature increase in proximity of a AuNP as a function of the power of the irradiating laser by performing an experiment similar to that described in the work of Reisman et al. [93]. The key idea was to measure the temperature on the surface of a AuNP under laser illumination by inducing dsDNA dehybridization in a cluster of functionalized AuNPs; the dehybridization of the dsDNA filaments that keep together the AuNPs - thus creating a cluster - makes the network disassemble and this phenomenon causes a shift in the SPR frequency. By measuring the SPR frequency in situ with a spectrometer, the cluster disaggregation can be detected and consequently the temperature increase can be evaluated. A representation of the expected SPR peak shift (blueshift) due to dsDNA dehybridization and then cluster disassembly is illustrated in Figure 6.2 [93].

Clusters of AuNPs were realized by incubating overnight two distinct solutions of 20 nm AuNPs functionalized with two complementary sequences of ssDNA (see Figure 6.3). The protocol for functionalizing 20 nm AuNPs is described in section 3.3.2. The effective assembly of the NPs was monitored by checking the optical properties of the solution: in fact, AuNPs functionalized with ssDNA are stable in solution and have a red colour, but the colour turns into purple as they aggregate, exactly because of the shift in the SPR frequency and the resulting different range of reflected light frequencies. In this way, clusters of AuNPs were formed but their dimensions could not be controlled, so the resulting heat generation under laser illumination was expected to be slightly different depending on the sample.
The melting temperature of the DNA duplexes formed during the assembly of the functionalized AuNPs was $T_m = 58.5\,°\mathrm{C}$, so the local temperature increase needed to disaggregate the clusters was $\Delta T = T_m - T_0 = 58.5\,°\mathrm{C} - 25\,°\mathrm{C} = 35\,°\mathrm{C}$. By referring to the calculations presented in the work by A.O. Govorov and H.H. Richardson [87], the necessary light flux of the illuminating laser was then $\Phi > 10^5\,\mathrm{W\,cm^{-2}}$ (see Figure 6.4). Nonetheless, these simulations were done for single AuNPs and not for networks of particles, therefore the effective increment in temperature was expected to be higher due to collective effects.
The SPR wavelength of 20 nm AuNPs (Sigma Aldrich, Darmstadt, Germany) is at λ_{SPR}=524 nm, so the sample was irradiated with a continuous-wave (CW) green laser (Changchun New Industries Optoelectronics Tech, Co, LTD, China) characterized by an emission spectrum peaked at $\lambda = 532\,\mathrm{nm}$ and by an output power of $P = 100\,\mathrm{mW}$. The laser was focused with a lateral resolution of 1 µm and an axial resolution of 4 µm; the resulting flux was then $\Phi = 2.5 \cdot 10^6\,\mathrm{W\,cm^{-2}}$. The SPR wavelength of the clusters solution is expected to be red-shifted with respect to the single particles one. After preparing the sample, we measured its absorption spectrum with a

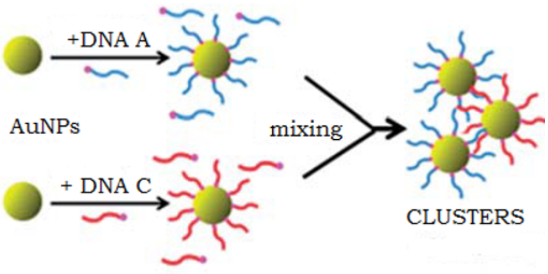

Figure 6.3: Formation of clusters by mixing two different solutions of AuNPs functionalized with two complementary ssDNA sequences (DNA A and DNA C). Image adapted from the paper of Piantanida et al. [88]

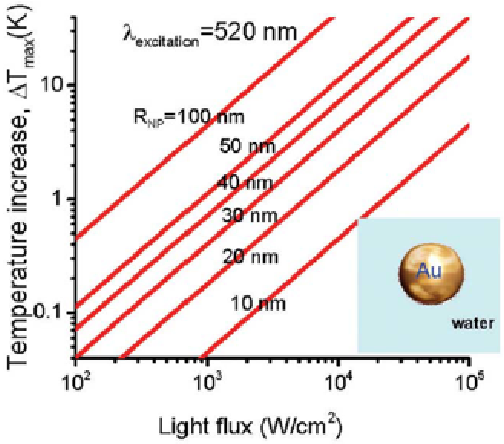

Figure 6.4: Calculated temperature increase at the surface of a single AuNP in water as a function of illumination power at the plasmon resonance [87].

spectrometer to have a reference value for further experiments. The absorption spectra of the single functionalized AuNPs and of the DNA-AuNPs networks solutions are shown in Figure 6.5 below: the peaks of the two spectra are respectively at 526 ± 1 nm and at 531 ± 1 nm.

The solution containing clusters of functionalized GNPs was placed inside a 140 μm diameter capillary and it was illuminated with an halogen lamp - necessary to obtain the absorption spectrum - from the top and with the CW green laser from the bottom (see Figure 6.6 for a representation of the experimental configuration). The absorption spectrum of the sample was recorded with a spectrometer while irradiating with the CW laser: we then expected to detect a progressive blue-shift of the SPR peak corresponding to the gradual disaggregation of the clusters. Some representative absorption spectra collected during the DNA dehybridization experiments are shown in Figures 6.7, 6.8 and 6.9 below. A blue shift of the SPR peak (from 528 nm to 522 nm) was observed after more than 15 min irradiation with the CW laser working at 11 mW (see respectively the orange line and the light blue line in Figure 6.7 and the green line and the light blue line 6.8). The final peak of the absorption spectrum had a value $\lambda = 522\,\text{nm}$ smaller than the SPR wavelength of 20 nm AuNPs in stock solution ($\lambda = 524\,\text{nm}$), because the power of the illuminating laser was so strong that it caused bubble formation in the sample solution and it induced a change in the dielectric constant of the medium (from ϵ_{water} to ϵ_{air}), thus reducing the SPR frequency.

In this experimental configuration only a micrometric region of the sample was illuminated

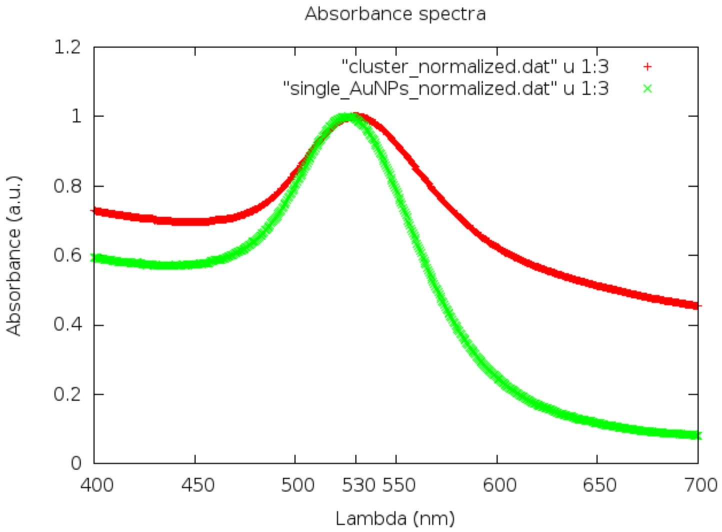

Figure 6.5: Absorbance spectra of single AuNPs functionalized with ssDNA and of clusters of AuNPs.

Figure 6.6: Experimental setup: the image on the top represents the irradiating laser and the bottom shows the sample holder and the microscope used for imaging.

.

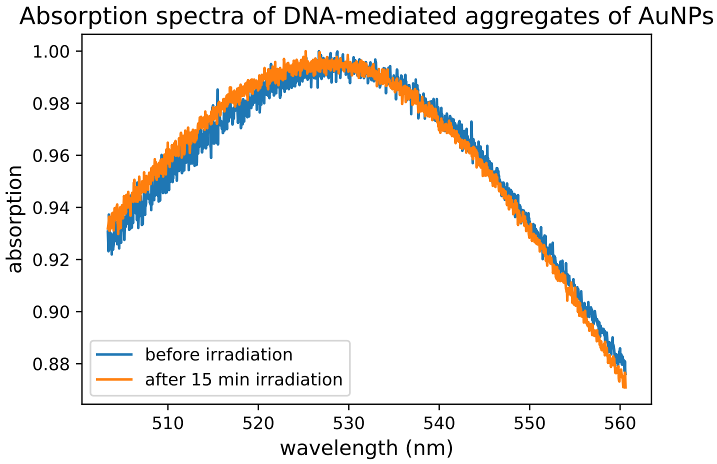

Figure 6.7: Absorbance spectra of DNA-AuNPs networks before and after laser irradiation.

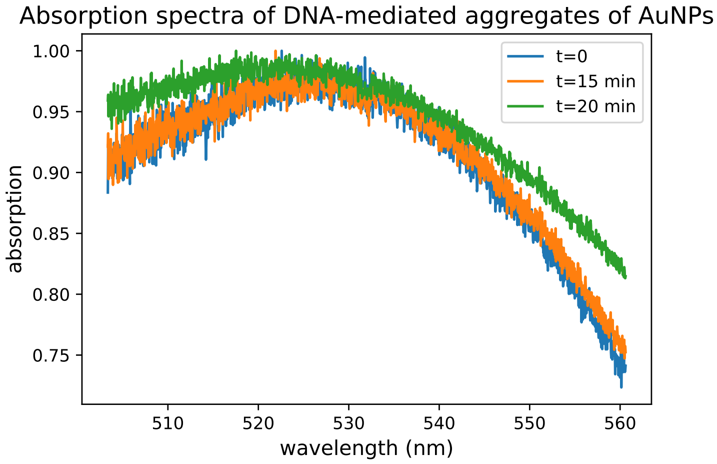

Figure 6.8: Absorbance spectra of DNA-AuNPs networks before and after laser irradiation.

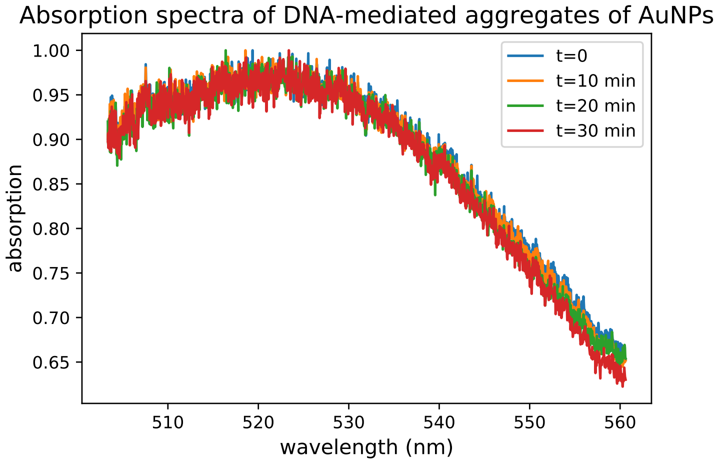

Figure 6.9: Absorbance spectra of DNA-AuNPs networks during laser irradiation. Each absorption curve is averaged over 5 measurements.The time interval between two consecutive measurements is $\Delta t = 10\,\text{min}$.

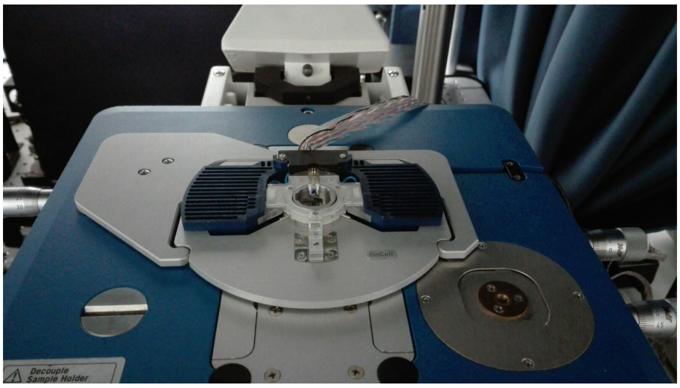

Figure 6.10: Picture of the sample holder of the JPK thermostat cell. The cell allowed to reach a nominal temperature of 60 °C, that corresponded to an effective temperature of 50 °C inside the sample compartment.

by the CW laser ($A_{\text{focus}} = 1\,\mu\text{m} \times 4\,\mu\text{m}$), while the absorption spectrum was measured from the whole sample ($V_{\text{sample}} \approx 15\,\text{mm}^3$). As a consequence, recorded absorption spectra were dependent on the illuminated region - where cluster disaggregation actually occurs - only to a minor extent, and they were strongly influenced by clusters from the non-irradiated region. This consideration explains why the blueshift of the SPR peak is visible in the first plot in Figure 6.7 but not in the second one in Figure 6.8.
Further experiments were then performed in a slightly different configuration: an aliquot of the sample solution (V=50 µL) was placed in a small compartment obtained from two coverslips glued together with double-sided tape and then put inside a thermostat cell (JPK BioCell, Berlin, Germany), as illustrated in Figure 6.10. The thermostat temperature was set at the maximum possible value of 60 °C and the cell was illuminated from the bottom with the 532 nm laser. In this way, it was possible to directly observe the disaggregation process of the GNPs clusters by simply using an optical microscope. In fact, even if the actual temperature of the sample was lower than the nominal one ($T_{\text{sample}} = 50\,^\circ\text{C}$ *vs* $T_{\text{thermostat}} = 60\,^\circ\text{C}$), the thermostat cell was keeping all the AuNPs clusters in thermal agitation in proximity of the melting temperature of DNA. A small increase in temperature -as induced by the irradiating laser- was thus sufficient to induce the transition between the aggregated-state to the single particles-state. We observed with an optical microscope the disaggregation process of the clusters of functionalized AuNPs kept in thermal agitation at 50 °C after illuminating for $\Delta t = 60\,\text{min}$ with a 532 nm CW laser working at 5 mW.

In conclusion, this set of experiments confirmed that a temperature increase of $\Delta T \approx 35\,^\circ\text{C}$ is reached when irradiating clusters of AuNPs with a CW laser with a light flux of $2.5 \cdot 10^5\text{W}\,\text{cm}^{-2}$. We could then evaluate the laser power and the irradiation time necessary to induce heat generation with a cluster of AuNPs functionalized with ssDNA. These values will be used as a starting point for future experiments aimed at estimating local temperature variations caused by illuminating single 20 nm AuNPs with a 532 nm laser. We expect that a higher flux will be needed when working with single nanoparticles, due to the absence of collective effects.

Chapter 7

Mechanical measurements on sliding DNA origami nanostructures

7.1 Force measurement on a gold-nanoparticle mediated sliding of doublet DNA origami filaments

Molecular machines are ubiquitous in living organisms, performing various types of physiological functions, including mechanical actuation, intracellular transport and signal transduction [94]. In DNA nanotechnology, there has been a deep interest in constructing DNA-based artificial systems that imitate motor proteins and that can move on a substrate [95], [96]. On this subject, Urban et al. [16] realized an artificial nanosystem which mimics sliding motor proteins and which is characterized by two DNA origami filaments that can slide on top on each other by coordinated nanoscale motions of gold nanoparticles powered by DNA fuels, as schematically illustrated in Figure 7.1.

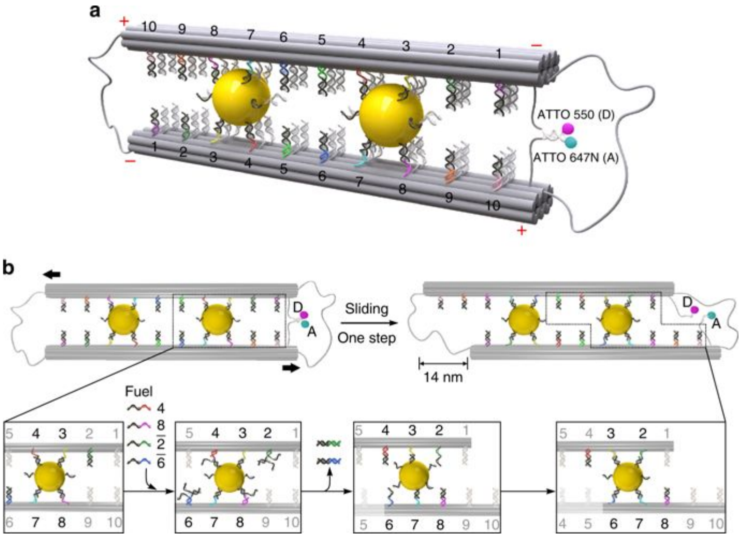

Figure 7.1: (a) Schematic representation of the slider origami characterized by two parallel 14-helix bundles folded out of the same scaffold and bound to two 10 nm AuNPs. (b) Schematic representation of the sliding mechanism: when the DNA fuels are added to the slider origami, the configuration of the bonds between the AuNPs and the DNA origami bundles changes and this process allows sliding of the two parallel filaments, thus inducing a 14 nm displacement. In both pictures, the fluorescent ATTO molecules are included in the schemes because they were used for FRET analysis. Images are adapted from the work of Urban et al. [16].

The sliding process is caused by the partial rotation of the two AuNPs bound to the DNA origami bundles when the specific DNA fuels (*i.e.* oligos with a particular sequence) are added in solution: this modification in the binding configuration induces a relative displacement of 14 nm between the two parallel filaments. The slider DNA origami is designed in such a way that it allows two consecutive sliding steps of 14 nm each, as illustrated in Figure 7.2, so the total possible displacement is of $\Delta x_{\text{tot}} = 28\,\text{nm}$. The correct sliding of the two filaments has been checked with Transmission Electron Microscopy (TEM) imaging and with Fluorescence Resonance Energy Transfer (FRET) experiments.

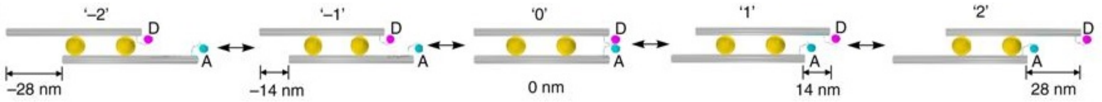

Figure 7.2: Schematic representation of the possible sliding steps of the slider origami: starting from an initial 0 configuration, the subsequent addition of DNA fuels allows the transition to configurations 1 and 2, where displacements of respectively $\Delta x_1 = x_1 - x_0 = 14\,\mathrm{nm}$ and $\Delta x_2 = x_2 - x_0 = 28\,\mathrm{nm}$ have taken place. The system is perfectly symmetric, so it can also undergo sliding along the opposite direction from the initial 0 configuration to configurations -1 and -2.

Since it has been proven that sliding can be induced in the doublet DNA origami filaments, an interesting further characterization is to estimate the intensity of the force exerted by the structure itself during motion. To this purpose, we performed magnetic tweezer (MT) experiments to measure the force applied by a single DNA origami filament on a magnetic bead during induced sliding. Also in this case, as in the previous measurements described in chapter 4, we used a DNA origami structure (6-helix bundle) as a tether to anchor the target structure to the surface of the flow cell: one extremity of the slider origami was then modified with biotin in order to bind to the streptavidin coated MT bead, while the other extremity was designed in such a way to match with the final part of the 6-helix bundle (6HB) attached to the surface through the digoxigenin-antidigoxigenin interaction. For clarity, the experimental configuration is illustrated in Figure 7.3.

As can be seen in this scheme, when the DNA fuels are added in solution, the doublet DNA origami filaments undergo sliding and consequently they exert a force on the MT bead ($F_{\mathrm{slid}} \parallel z$). The direction of the force can be upwards or downwards depending on the set of DNA fuels used; in fact, the slider origami can move from configuration 0 to 1 and 2, but also to move symmetrically from the state 0 to -1 and -2, as displayed in Figure 7.2. Since, at the same time, the bead experiences the magnetic force of the permanent magnets F_{mag}, three different situations are possible depending on the intensity of the applied forces, in the condition that F_{slid} and F_{mag} are anti-parallel:

- if $F_{\mathrm{mag}} > F_{\mathrm{slid}}$ the slider origami is pulled upwards by the magnetic force, so the z-position of the MT bead is expected to increase;
- if $F_{\mathrm{mag}} < F_{\mathrm{slid}}$ the slider origami is pulled downwards by the sliding force, so the bead z-position should decrease in progressive steps of $\Delta z = -14\,\mathrm{nm}$ each;
- if $F_{\mathrm{mag}} = F_{\mathrm{slid}}$ an equilibrium between the two forces is reached and the bead trajectory is expected to be a stable line.

We then performed MT experiments in which we applied a constant magnetic force to the beads (F_{mag} in the range between 1 and 10 pN) and we injected the DNA fuels in the MT flow cell while recording the bead position. By analyzing the bead trace along the z-axis, we expected to be able to attribute its behaviour to one of the three cases described above. By reaching the equilibrium condition, it would then be possible to evaluate the intensity of the force applied by the sliding origami.

To have a rough estimate of the sliding force, we calculated the variation in the free energy of the system made by the doublet DNA origami filaments and the two AuNPs due to the sliding process. As explained schematically in Figure 7.1, the addition of the DNA fuels changes the oligonucleotides of the DNA origami structure that are bound to the AuNPs and those that are

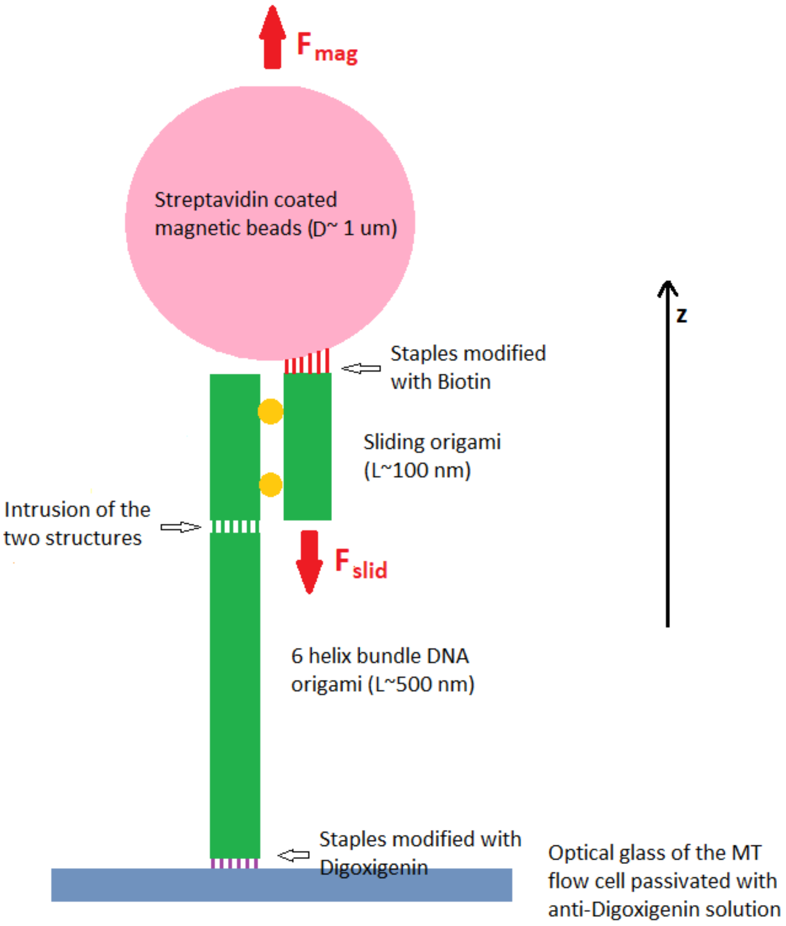

Figure 7.3: Schematic representation of the experimental configuration to measure the force applied by the doublet DNA origami filaments during sliding. From top to bottom: the streptavidin coated MT bead is bound to one filament of the slider origami through the streptavidin-biotin interaction, while the opposite end of the other filament is attached to the tether 6HB by intrusion; the other extremity of the 6HB includes digoxigenin-modified staples, so it can bind to the anti-digoxigenin coated surface of the flow cell.

unbound, thus inducing a variation in the total free energy. By using the Oligo Analyzer Tool of the Integrated DNA Technology (IDT) company website, we calculated the free energy G associated to the binding oligos in the initial configuration (state 0) and in the final configuration after one step of sliding (state 1). Since this change is associated to a displacement of $\Delta x = 14\,\text{nm}$, the resulting force can be computed with the following relation:

$$F_{\text{slid}} = \frac{\Delta\Delta G}{\Delta x}. \tag{7.1}$$

The difference in free energy is $\Delta\Delta G = \Delta G(\text{state1}) - \Delta G(\text{state0}) = -117.13\,\text{kcal mol}^{-1}$, hence the sliding force is approximately

$$F_{\text{slid}} = \frac{-117.13\,\text{kcal mol}^{-1}}{14\,\text{nm}} = 58\,\text{pN}. \tag{7.2}$$

Based on these calculations, the doublet DNA origami filaments were then expected to always slide if stretched with magnetic forces in the range between 1 and 10 pN (*i.e.* forces compatible with 1 µm MT beads).

In the following sections I will report the protocols to synthesize and purify the slider origami and the 6HBs and to realize the final structure. I will then describe the MT experiments performed so far.

7.2 Design and synthesis of the sample

To fold the slider origami, we set up the following folding reaction:

Reagent	**Final concentration**
Scaffold (p8064)	10 nM
Staples	100 nM
$MgCl_2$	20 mM
NaCl	5 mM
50× TAE	1×
H_2O	

The solution was first heated up to 65 °C to denaturate the scaffold, then it progressively reached a final temperature of 25 °C in 16 h. Each step of this thermal ramp helps to overcome the energy barrier of the hybridization reaction between the scaffold and each staple, thus allowing the origami formation. After folding, the sample was purified from excess staples with PEG precipitation, because this purification process allows to obtain high values of the final sample concentration, which are necessary when the origami have to be bound to gold nanoparticles. The PEG purification protocol includes the following steps:

- adjust the $MgCl_2$ concentration of the origami solution to 20 mM;
- add to the sample to be purified an equal volume of PEG buffer (7.5% PEG-8000, 250 mM NaCl, 1 × Tris Acetic Acid)
- spin at 16 000 RCF at room temperature for 30 min;
- remove the surnatant, resuspend the pellet in the buffer used for folding and leave the sample in thermal agitation at 27 °C for 30 min;
- after centrifuging again the sample in the PEG buffer, remove the surnatant and leave the sample in the folding buffer in thermal agitation overnight.

In parallel to the slider synthesis, we functionalized 10 nm AuNPs with ssDNA oligos by using the freeze and thaw method described in section 3.3.2. The functionalized AuNPs were then incubated at 23 °C with the slider origami for 24 h. Since 20 × excess of AuNPs was added to the origami to facilitate binding, a further gel electrophoresis step was necessary to get rid of the surplus of nanoparticles. As AuNPs bound to the origami migrate slowlier than free NPs, two distinct bands form in the gel, as can be seen in Figure 7.4. The bands were cut and squeezed to extract the sample and then it was imaged with the TEM to check the correct assembly of the slider origami with the nanoparticles.

The 6HB DNA origami used as tethers in MT experiments were folded by mixing the p8634 scaffold and the staples in a solution made of Tris-Acedic Acid-EDTA buffer and 20 mM $MgCl_2$ and by incubating them in the thermocycler for 16 h. They were then purified from excess staples by centrifuging them for 5 times in Amicon filters (Amicon Utra 0.5 mL 100 kDa (Millipore, Massachusetts) at 8000 g for 10 min. The 6HB DNA origami were finally stained with Uranyl

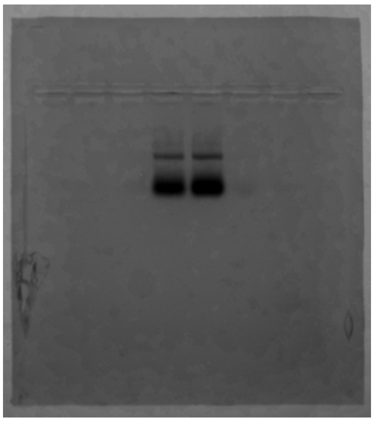

Figure 7.4: A 0.7% agarose gel for band separation of the AuNPs correctly assembled to the origami and of the excess of AuNPs.

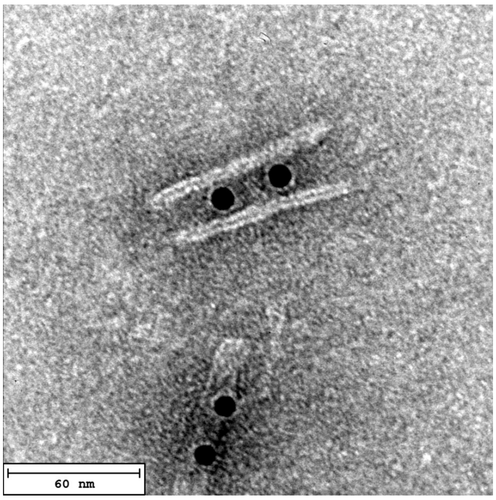

Figure 7.5: A representative TEM image of a slider origami with two 10 nm AuNPs. The slider DNA origami were previously stained with Uranyl Formate.

Formate and deposited on a carbon-coated grid for TEM imaging to check the correct folding. A TEM picture is illustrated in Figure 7.6.

The last step for the sample preparation consisted in the incubation of the slider origami and the 6HB origami in a molar ratio 1:1 at 23° for 24 h. NaCl in a concentration of 500 mM was added to the buffer solution to facilitate the binding process. Gel electrophoresis analysis was then performed to confirm the effective assembly of the complex structure. In Figure 7.7 a picture of the 1.5% agarose gel prepared for checking the structure is shown. The different bands correspond respectively to the 1 kilobases (kb) ladder for control, the 6HBs, a first aliquot of slider origami, the complex structure made of 6HBs + slider and a second aliquot of slider origami. The fourth column - corresponding to the 6HBs bound to the slider origami - shows two distinct bands with similar intensity, thus indicating that approximately half of the structures has been formed. We expected the band closer to the well to contain the assembled structure, because they are more massive and migrate more slowly. We then cut and squeezed that band to extract the final DNA origami structures. The collected nanostructures were finally stained with Uranyl Formate and imaged with the TEM.

A representative TEM image of the complex DNA origami structures made of the 6HBs and the sliders decorated with the AuNPs is illustrated in Figure 7.8.

In Figure 7.9, a detail of a *cadnano* image of the intrusion between the 6HB and the slider

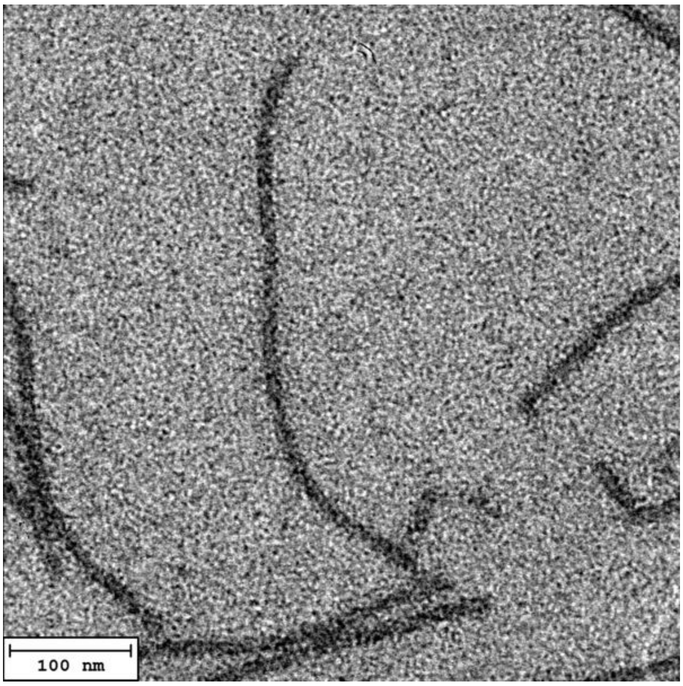

Figure 7.6: A representative TEM image of a 6HB DNA origami. The 6HB DNA origami were previously stained with Uranyl Formate.

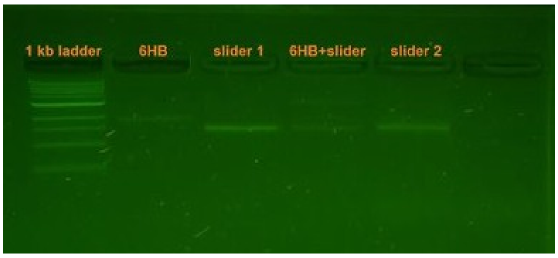

Figure 7.7: Gel electrophoresis analysis to check the correct assembly of the 6HBs and the slider origami.

origami is represented: their ends were designed to be wedged in like a puzzle, to assure stability to the complex system. Association of two distinct origami units can indeed be easily mediated by base pairing between complementary strands extending from the helices of two facing edges and by stacking. In fact, DNA origami shapes can be viewed as compact multilayers of antiparallel helices, resulting in the display of a dense set of nucleobases at the edges of the structures. Such bases are then able to establish $\pi - \pi$ stacking interactions with the terminal bases exposed at the boundaries of a different origami unit. Of course, geometric matching is of relevance to allow maximum surface contact between facing edges [27]: for this reason the 6HB had to be specifically design to match with the slider origami.

7.3 Magnetic tweezer measurements of the sliding force

7.3.1 Sample and setup preparation

For preparing the sample for MT measurements, the complex origami were mixed with MyOne beads and left in incubation overnight. The reported binding capacity for 1 mg of magnetic beads is 20 µg of biotinylated dsDNA. For oligonucleotides, the binding capacity is inversely related to the molecule size due to steric hindrance, so we added an amount of DNA origami in

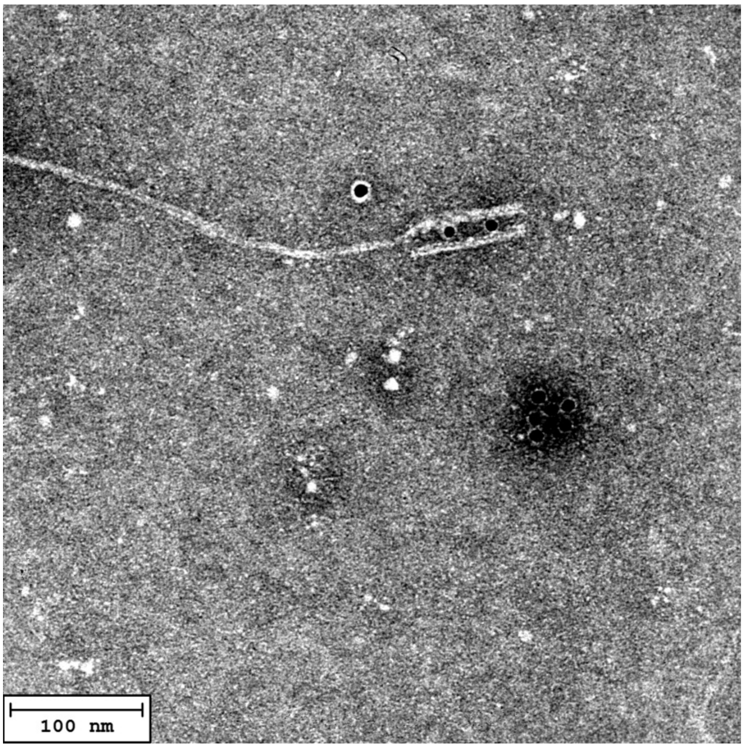

Figure 7.8: A representative TEM image of the slider origami assembled with the 6HB. The DNA origami were previously stained with Uranyl Formate.

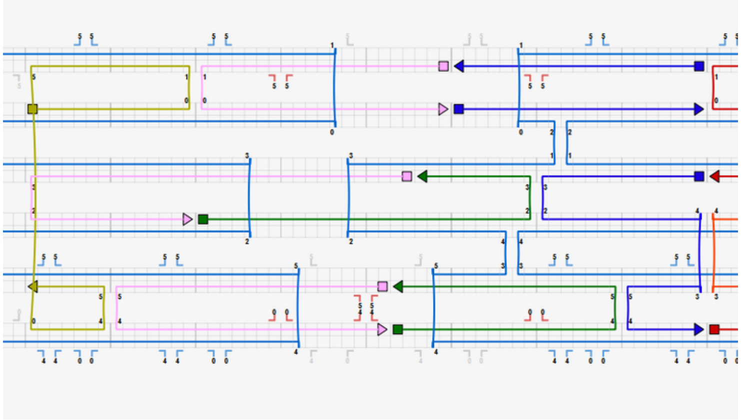

Figure 7.9: Intrusion between one extremity of the 6HB and one extremity of part of a filament of the slider origami

a 10× excess with respect to the recommended quantity for dsDNA.
We prepared the MT flow cell as described in chapter 4, by passivating the epoxy-silane coated surface of the glass slide with anti-digoxigenin for 1 h and then with Blocking Aid solution for 1 h. The sample (formed by the complex origami previously mixed with the streptavidin coated beads) was incubated in the flow cell for 1 h to let the digoxigen-modified extremity of the 6HBs attach to the surface of the flow cell. The buffer solution was made up of Tris-Acetic Acid, EDTA and 5 mM $MgCl_2$,0.1 mg mL^{-1} of Bovine Serum Albumine (BSA) and 0.1% of Tween20 and it was used both for incubating the origami and the beads and for filling the flow cell. The $MgCl_2$ concentration was reduced with respect to the synthesis condition, to prevent stacking of the beads to the surface.
After incubation of the sample, beads that were not attached to the surface were removed by

applying a small force of 1 pN and then flushing repeatedly with buffer solution. In this series of measurements, it was extremely important to remove beads floating inside the flow cell. In fact, the AuNPs-mediated sliding of the DNA origami filaments was induced by adding into the flow cell the oligonucleotides necessary for the toehold-mediated process, just before to recording the bead position at constant force. In each experimental step, the addition of the oligos for sliding (the fuels) was thus causing the formation of a liquid current inside the flow cell and consequently the flushing of all the free beads in the field of view (FOV) involved in the measurements. Since the flushing beads were a huge obstacle to the detection of the bead displacement caused by the sliding of the DNA origami filaments, it was fundamental to remove them before starting the experiments.

As explained in chapter 4, the first step in each MT experiment consisted in measuring the tethering length of the beads under a constant force of 1 pN to check if they were correctly bound to the origami. If the bead was not showing any significant fluctuation while applying a pulling force, it was used as a reference bead for further measurements. In this case, it was also crucial to identify a very stable reference bead, as the length variations involved were extremely small ($\sim$14 nm for each sliding step). On the contrary, if the difference between the $z-$position of the bead with the force *off* and with the force *on* was $L \approx 570\,\text{nm}$ (*i.e.* compatible with the length of the complex origami), it was assumed that it was anchored to the surface through the DNA origami nanostructures.

After selecting the beads of interest, a constant force in the order of 1 pN was applied to the samples. The 1 µm$-$diameter MyOne beads allow indeed to exert forces in the range between 1 pN and 10 pN in standard experimental condition. The fuels for generating the first sliding step (0 $\rightarrow$ 1) were added into the flow cell in a 1000$\times$ excess with respect to the expected amount of complex origami. The bead position along the vertical $z-$axis was then recorded at constant force for 30 min to let the two DNA origami filaments slide on top of each other. After that, the second aliquot of fuels for the sliding step 1 $\rightarrow$ 2 was added, while keeping the force constant to prevent the origami from lying down on the flow cell surface in between the measurements. The z-position of the bead was then acquired for 30 min. The same procedure was repeated for the back sliding steps 2 $\rightarrow$ 1 and 1 $\rightarrow$ 0. As illustrated in Figure 7.2, with the forces involved we expected to detect a variation $\Delta z = 14\,\text{nm}$ in each sliding step, respectively an increment of the bead height for the transitions from the configuration 0 to 1 and 2, and a decrease of the bead $z-$coordinate for the backwards displacements from the state 2 to 1 and 0.

The mechanism of flushing the fuels inside the flow cell had the advantage of removing the excess oligos from the previous sliding step before the addition of the following aliquot, thus avoiding the problem of having competitive ssDNA filaments for toehold-mediated displacement of the AuNPs on top on the DNA origami bundles. In the following paragraph, I will show some preliminary data from the MT experiments on the slider origami.

7.3.2 Results

The first test was done by flushing inside the flow cell only the oligos for inducing the sliding step from the configuration 0 to 1, while applying a constant force of 6.6 pN and then recording the bead position for 140 s. The measure of the tethering length of the bead reveals that it is bound to the surface *via* the complex origami and that the fluctuations at zero force are large. A step $\Delta z \approx 20\,\text{nm}$ can be observed after the addition of the fuels. This variation is consistent with the 14 nm displacement expected for the first sliding step.

Experiments were then repeated by changing the magnetic force to see if there were any variations in the behaviour of the origami. The moles of fuels were always in a 1000$\times$ excess with respect to the quantity of nanostructures inside the flow cell: this was done to facilitate the toehold-mediated process that allowed the motion of the slider origami. The pump flow was set to the minimum value to avoid the detachment of the samples from the surface while flushing.

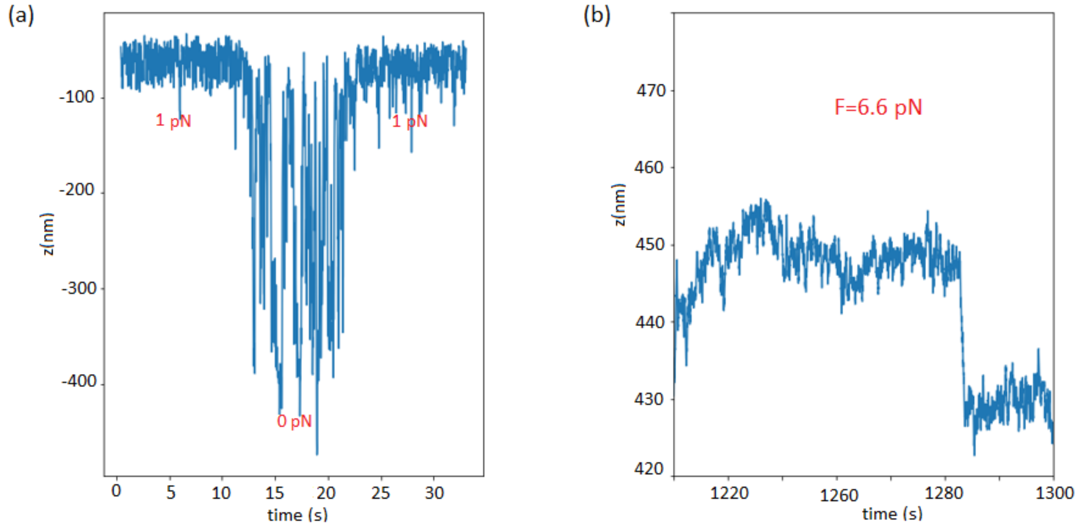

Figure 7.10: (a) Measure of the tethering length of the bead with a force F=1 pN. (b) Measure of the $z-$position of the bead with a force F=6.6 pN after addition of the fuels to induce the sliding step 0 → 1.

Figure 7.11 represents a series of data acquired on the same complex origami. The first test was done by applying a force of 1 pN and then switching off the force: since the difference in the $z-$position is $l \approx 600\,\text{nm}$, it was assumed that the bead was correctly attached to the complex origami. A force of 3 pN was then applied and kept constant for further measurements. The fuels to induce sliding were added in sequence and the bead position was recorded immediately after flushing the oligos inside the flow cell. In Figure 7.11b a step $\Delta z \approx 30$ nm can be observed. Since no variations in the bead height can be noted in the plot (a) after the addition of the first fuels, a direct transition from the configuration 0 to the configuration 2 may have occurred in the slider origami when also the second aliquot of fuels had diffused inside the flow cell. The bead position after the addition of the oligos for the back-sliding does not show any variation. In all these plots the data are very noisy because of the intrusion of floating beads and/or impurities in the FOV under investigation as a consequence of flushing.

The set of data presented in Figure 7.12 is similar to the ones just shown. The tethering length is compatible with the contour length of the complex origami. The sequence of measurements at 6.6 pN force after progressive addition of the fuels reveals that a transition between two states - most probably from 0 to 1, as the transition from 1 to 2 cannot take place without the previous step - has occurred. The variation in the $z-$coordinate of the bead is indeed $\Delta z \approx 15\,\text{nm}$. The displacements from state 2 to 1 seem to not be detectable.

7.3.3 Critical points and future plans

The acquired data proved that the protocol of preparation of the beads and the complex origami was successful, as the tethering length of the beads was compatible with the expected one in more than 25% of the cases. The attachment of the 6HBs to the passivated surface was stable in the range of tested forces and the composite origami structure did not disassemble during

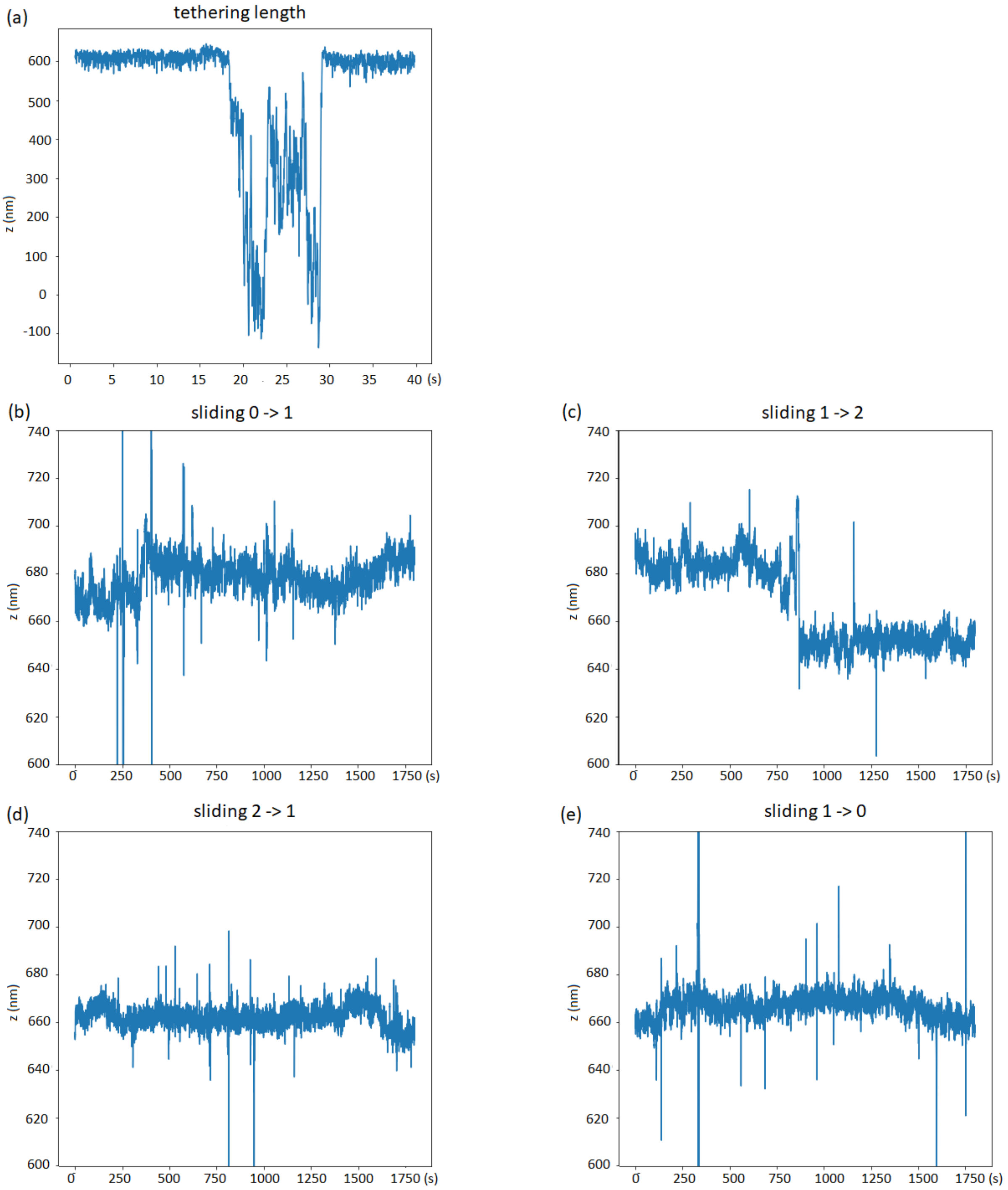

Figure 7.11: (a) Measure of the tethering length of the bead with a force F=1 pN. (b) Measure of the $z-$position of the bead with a force F=3 pN after addition of the fuels to induce the sliding steps $0 \rightarrow 1 \rightarrow 2$ and then $2 \rightarrow 1 \rightarrow 0$.

measurements, thus indicating that the binding between the two elements *via* staples-intrusion was well designed.

Further measurements will be necessary to confirm that the observed variations in the bead height are actually due to the sliding of the origami and are not caused by external factors. It will also be important to understand why only a single sliding step (instead of the whole sequence) is observed in the experiments. To this purpose, it could be useful to increase the duration of

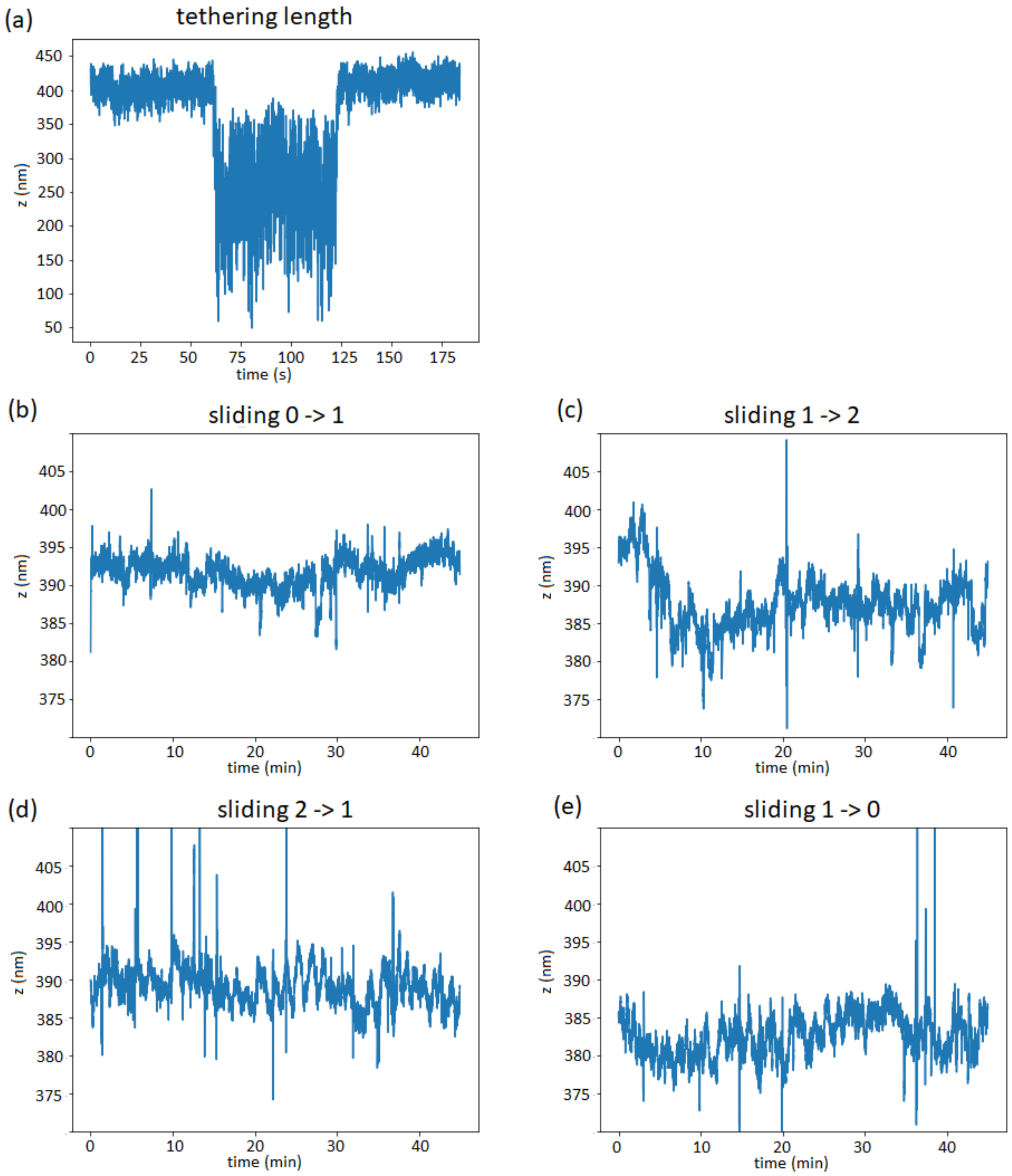

Figure 7.12: (a) Measure of the tethering length of the bead with a force F=1 pN. (b) Measure of the $z-$position of the bead with a force F=6.6 pN after addition of the fuels to induce the sliding step $0 \to 1 \to 2$ and then $2 \to 1 \to 0$.

the measurements. Finally the flushing protocol for the fuels need to be further optimized to drastically reduce the noise in the data.

Chapter 8

Conclusions and Outlook

During my PhD, I combined different experimental techniques to validate a method to investigate the effects of local temperature variations on the dynamics of biomolecules. The central element of the suggested system was the DNA origami nanotechnology, as DNA origami nanostructures can be efficiently used to manipulate biomolecules and they can be functionalized with gold nanoparticles (AuNPs) [14]. The possibility to locate AuNPs with nanometric precision was crucial to our purposes, as we intended to exploit plasmon formation in metal nanoparticles as a source of local heating. A ssDNA hairpin was used as a probe to test the effectiveness of the system at a constant temperature. Its dynamics was then investigated with two different approaches, *i.e.* by performing magnetic tweezer (MT) experiments and by using DNA origami force spectroscopy: both methods enabled us to apply the forces necessary to induce the unzipping of a 24 bp-hairpin (1-20 pN).

I designed, synthesized and characterized two different origami, a rigid 680 nm-long 4-helix bundle (4HB) and a force clamp similar to that presented in the paper of P. Nickels[17] and I modified both structures so that they included the 24 bp-long ssDNA hairpin of the scaffold in a region suitable for measuring. I established a protocol for performing magnetic tweezer measurements and applying forces between 1 pN and 20 pN on the target biomolecule by using 4HB DNA origami nanostructures as tethers. The resulting noise amplitude $\sigma \approx 5\,\text{nm}$ is compatible with the value reported in literature for similar experiments [55] and enables in principle the detection of the zipping/unzipping mechanism of the target 24 bp-long hairpin, whose length is $\Delta z \approx 24\,\text{nm}$. By repeating MT experiments, I found out that the unzipping force of the hairpin was $F = 12 \pm 1\,\text{pN}$, in accordance with the data presented in the literature for hairpins with a similar length and sequence ($F_{unfolding} \approx 15\,\text{pN}$ for a 25 bp long ssDNA hairpin [60]). Nonetheless, the main limitation of MT force spectroscopy is the requirement of a physical connector to the micrometer-sized probe, which prevents direct access to the molecule under investigation and which causes drift and noise in the bead traces. Our measurements were indeed affected by the interaction between the probe/connector system and the substrate and this observation lead us to the conclusion that a better scheme had to be used to precisely control force and temperature. For this reason, we decided to perform DNA origami force spectroscopy experiments, by using an hairpin-modified force clamp origami. We thus adapted the nanosensor designed by P. Nickels to study a different biological system (*i.e.* the 24 bp-long ssDNA hairpin) and to investigate a wider range of forces, between 1 pN and 20 pN.

I folded 1 pN- and a 12 pN- force clamp DNA origami and I measured the Förster Resonance Energy Transfer (FRET) signal between a pair of fluorophores placed at the neck of the target hairpin to detect changes in the configuration. In this way, I had direct access to the dynamics of the ssDNA hairpin and I found the same unzipping force $F_{unzip} \approx 12 \pm 4\,\text{pN}$. The two methods hence confirmed the same results, but DNA origami force spectroscopy represents a more linear way to characterize the dynamics of a biomolecule and so it is more appropriate to study how that dynamics is affected by an additional parameter, *i.e.* temperature variations.

Moreover, the comparison between MT and DNA origami force spectroscopy demonstrated the validity of the calculations for estimating the force in our particular force clamp configuration, with the introduction of a 24-bp ssDNA hairpin and with the addition of two fluorophores-modified staples. The calculations were based on the modified Freely Jointed Chain model and I estimated the force under the assumption that the contour length of the ssDNA spring did not have to include the parts of the ssDNA filament bound to the dyes-modified staples for FRET signalling.

Based on the results presented in the literature [87] [91] [89] and of the experiments aimed at investigating local heating by exploiting the DNA dehybridization process as a probe of effective heating in plasmon resonance conditions, I figured out two possible ways of combining temperature variations and DNA origami force spectroscopy. A first approach could be that of attaching a AuNP to the force clamp origami with the target hairpin and to use it as a local heating source by illuminating it with a laser tuned at the surface plasmon resonance frequency. In fact, the experiments on plasmon-induced heating presented in this thesis provided an estimation of the light flux and the irradiation conditions necessary to induce local heating. A second approach could involve the addition of two AuNPs at the neck of the hairpin - instead of the fluorophores. The AuNPs would be simultaneously used as local heating sources and labels for detecting changes in the hairpin configuration, as any zipping/unzipping event would cause a shift in the surface plasmon resonance peak.

In this thesis, I also presented the preliminary data relative to a side project, which was aimed at detecting the force exerted by the DNA origami structure designed by M. Urban[16] during the sliding process between two DNA origami filaments mediated by two gold nanoparticles after addition of specific fuels. On the basis of my previous work, I figured out a method to identify the sliding force with a magnetic tweezer test. To this purpose, I designed a 6-helix bundle (6HB) that was matching one extremity of the slider origami in such a way that they formed a single composite structure. The 6HB had the role to increase the total end-to-end distance of the origami and to reduce interactions with the surface of the MT flow cell. I adapted the experimental protocol developed for measuring the 4HBs so that the complex origami could bind to the 1 µm paramagnetic beads and to the passivated surface of the MT flow cell and I performed MT measurements. I recorded with a complementary metal-oxide-semiconductor (CMOS) sensor camera the bead position over the $z-$direction at constant forces while adding the fuels necessary to induce the sliding and I observed Δz variations compatible with the expected movement of the two filaments of the slider. Further measurements need to be done to confirm these results and different forces have to be tested. The comparison of the recorded bead positions at increasing forces will enable to determine the force exerted by the origami: in fact, the $z-$position should resemble a stable line when the external magnetic force reaches the sliding force.

Bibliography

[1] R. Feynman, *There's Plenty of Room at the Bottom*, transcript of the talk given at the annual meeting of the American Physical Society at Caltech, 1960

[2] J.H. Chen and N.C. Seeman, *Synthesis from DNA of a molecule with the connectivity of a cube*, Nature, 1991

[3] P.W.K. Rothemund, *Folding DNA to create nanoscale shapes and patterns*, Nature, 2006

[4] F. Hong, F. Zhang, Y. Liu and H. Yan, *DNA origami: scaffolds for creating higher order structures*, Chemical Reviews, 2016

[5] D. M. Sagar, S. Aoudjane, M. Gaudet, G. Aeppli and P. A. Dalby, *Optically Induced Thermal Gradients for protein characterization in nanoliter-scale samples in microfluidic devices*, Scientific Reports, 2013

[6] X. Yanga, J. Liua, Y. L. Xieb, Y. Wangb, H. Yinga, Q. Wua, W. Huanga, G. Jenkins, *A novel microfluidic system for the rapid analysis of protein thermalstability*, Journal of Royal Chemical Society, 2014

[7] M. Iwaki, A.H. Iwane, K. Ikezaki, T. Yanagida, *Local heat activation of single myosins based on optical trapping of gold nanoparticles*, Nanoletters, 2015

[8] M. Iwaki, S. Wickham, K. Ikezaki, T. Yanagida and W. Shih, *A programmable DNA origami nanospring that reveals force-induced adjacent binding of myosin VI heads*, Nature Communications, 2016

[9] Y. Kamei, M. Suzuki, K. Watanabe, K. Fujimori, T. Kawasaki, T. Deguchi, Y. Yoneda, T. Todo, S. Takagi, T. Funatsu and Shunsuke Yuba, *Infrared laser–mediated gene induction in targeted single cells in vivo*, Nature Methods, 2008

[10] Q. Liu, M.J. Frerck, H. A. Holman, E.M.Jorgensen, R.D.Rabbitt, *Exciting Cell Membranes with a Blustering Heat Shock*, Biophysical Journal, 2014

[11] K. Oyama, A. Mizuno, S.A. Shintani, H. Itoh, T. Serizaw, N. Fukuda, M. Suzuki, Shin'ichi Ishiwata, *Microscopic heat pulses induce contraction of cardiomyocytes without calcium transients*, Biochemical and Biophysical Research Communications, 2012

[12] G. Baffou, H. Rigneault, D. Marguet and Ludovic Jullien, *A critique of methods for temperature imaging in single cells*, Nature, 2014

[13] K. Okabe, N.o Inada, C. Gota, Y. Harada, T. Funatsu and S. Uchiyama, *Intracellular temperature mapping with a fluorescent polymeric thermometer and fluorescence lifetime imaging microscopy*, Nature Communications, 2012

[14] J.A.Johnson, A. Dehankar, A. Robbins, P. Kabtiyal, E. Jergens, K.H. Lee, E. Johnston-Halperin, M. Poirier, C.E.Castro, J.O.Winter, *The path towards functional nanoparticle-DNA origami composites*, Science, 2019

[15] C. Gosse and V. Croquette, *Magnetic Tweezers: micromanipulation and force measurement at the molecular level*, Biophysical Journal, 2002

[16] M.J. Urban, S. Both, C. Zhou, A. Kuzyk, K. Lindfors, T. Weiss and L. Na Liu, *Gold nanocrystal-mediated sliding of doublet DNA origami filaments*, Nature Communications, 2018

[17] P. C. Nickels, B. Wünsch, P. Holzmeister, W. Bae, L. M. Kneer, D. Grohmann, P. Tinnefeld and T. Liedl, *Molecular force spectroscopy with a DNA origami–based nanoscopic force clamp*, Science, 2016

[18] *A single-molecule technique: a laboratory manual*, Cold Spring Harbor Laboratory Press, 2008

[19] D. Han, S. Pal, J. Nangreave, Z. Deng, Y. Liu, H.Yan, *DNA origami with complex curvatures in three-dimensional space*, Science, 2011

[20] E.S. Andersen, M. Dong, M.M. Nielsen, K. Jahn, R. Subramani, W. Mamdouh, M.M. Golas, B. Sander, H. Stark, C.L. Oliveira, *Self-assembly of a nanoscale DNA box with a controllable lid*, Nature 2009

[21] S. M. Douglas, H. Dietz, T. Liedl, B. Hogberg, F. Graf and W. M. Shih, *Self-assembly of DNA into nanoscale three-dimensional shapes*, Nature, 2009

[22] Y. Ke, S.M. Douglas, M. Liu, J. Sharma, A. Cheng, A. Leung, Y. Liu, W.M. Shih, H. Yan, *Multilayer DNA origami packed on a square lattice*, Journal of the American Chemical Society, 2009

[23] H. Dietz, S.M. Douglas, W.M. Shih, *Folding DNA into twisted and curved nanoscale shapes*, Science, 2009

[24] T. Liedl, B. Hoegberg, J. Tytell, D.E. Ingber and W.M. Shih, *Self-assembly of 3D prestressed tensegrity stuctures from DNA*, Natue Nanotechnology, 2010

[25] D. Han, S. Pal, Y. Liu, H. Yan, *Folding and cutting DNA into reconfigurable topological nanostructures*, Nature Nanotechnology, 2010

[26] Z. Zhao, H. Yan, Y. Liu, *A route to scale up DNA origami using DNA tiles as folding staples*, ACS Nano, 2010

[27] W. Pfeifer and B. Saccá, *From Nano to Macro through Hierarchical Self-Assembly: The DNA Paradigm*, ChemiBioChem, 2016

[28] W. Liu, H. Zhong, R. Wang, N.C. Seeman, *Crystalline two-dimensional DNA-origami arrays*, Angewandte Chemie, 2011

[29] A.A. Rafat, T. Pirzer, M.B. Scheible, A. Kostina, F.C. Simmel, *Surface-assisted large-scale ordering of DNA origami tiles*, Angewandte Chemie, 2014

[30] H. Gu, J. Chao, S.J. Xiao, N.C. Seeman, *A proximity-based programmable DNA nanoscale assembly line*, Nature, 2010

[31] A.E. Marras, L. Zhou, H.-J. Su and C.E. Castro, *Programmable motion of DNA origami mechanismst*, PNAS, 2014

[32] B. Ding, Z. Deng, H. Yan, S. Cabrini, R.N. Zuckermann, J. Bokor, *Gold nanoparticle self-similar chain structure organized by DNA origami*, Journal of the American Chemical Society, 2010

[33] Z. Zhao, Y. Liu, H. Yan, *Encapsulation of gold nanoparticles in a DNA origami cage*, Angewandte Chemie, 2011

[34] G. Mie, *Beitraege zur Optik Trueber Medien, Speziell Kolloidaler, Metalloesungen*, Ann. Physik, 1908

[35] E. Prodan, C. Radloff, N.J. Halas, P.A. Nordlander, *Hybridization model for the plasmon response of complex nanostructures*, Science 2003

[36] Q. Jiang, C. Song, J. Nangreave, X. Liu, L. Lin, D. Qiu, Z.G. Wang, G. Zou, X. Liang, H. Yan, *DNA Origami as a carrier for circumvention of drug resistance*, Journal of American Chemical Society, 2012

[37] J.D. Watson and F.H.C. Crick, *Molecular structure of nucleid acids*, Nature, 1953

[38] O.Saleh, *Biopolymer mechanics: force-extension of FJC and WLC*, 2018

[39] R. Petrosyan, *Improved approximations for some polymer extension models*

[40] N.B. Becker, A. Rosa and R. Everaers, *The radial distribution function of worm-like chains*, The European Physical Journal, 2010

[41] J.F. Marko and E.D. Siggia, *Stretching DNA*, Macromolecues, 1995

[42] C. Bouchiat, M.D. Wang, J.-F. Allemand, T. Strick, S.M. Block and V. Croquette, *Estimating the persistence length of worm-like chain molecule from force-extension measurements*, Biophysical Journal, 1999

[43] S.M. Douglas, A.H. Marblestone, S. Teerapittayanon, A. Vazquez, G.M. Church and W.M. Shih, *Rapid prototyping of 3D DNA-origami shapes with caDNAno*, Nucleic Acid Research, 2009

[44] H. Dietz, S.M. Douglas and W.M. Shih, *Folding DNA into twisted and curved nanoscale shapes*, Science, 2009

[45] Y. Ke, S.M. Douglas, M. Liu, J. Sharma, A. Cheng, A. Leung, Y. Liu, W.M. Shih and H. Yan, *Multilayer DNA origami packed on a square lattice*, Journal of American Chemical Society, 2010

[46] C.E. Castro, F. Kilchherr, D.N. Kim, E.L. Shiao, T. Wauer, P. Wortmann, M. Bathe and H. Dietz, *A primer to scaffolded DNA origami*, Nature Methods, 2011

[47] K. Jahn, T. Tørring, N. V. Voigt, R. S. Sørensen, A. L. Bank Kodal, E. S. Andersen, K. V. Gothelf, and J. Kjems, *Functional Patterning of DNA Origami by Parallel Enzymatic Modification*, Bioconjugate Chemistry, 2011

[48] P.U. Walker, *Fast Dynamics of Biological Systems Investigated with Magnetic Tweezers and Small-Angle X-Ray Scattering*, Ph.D. Thesis of the Ludwig Maximilians Universitaet, 2018

[49] J. Lipfert, M. Wiggin, J. W. Kerssemakers, F. Pedaci, and N. H. Dekker, *Freely orbiting magnetic tweezers to directly monitor changes in the twist of nucleic acids*, Nature Communication, 2011

[50] J. Lipfert, X. Hao, and N. H. Dekker, *Quantitative modeling and optimization of magnetic tweezers*, Biophysical Journal, 2009

[51] P. Hinterdorfer and A. Oijen, *Handbook of Single-Molecule Biophysics*, Springer-Verlag New York, 2009

[52] N. Ribeck and O.A. Saleh, *Multiplexed single-molecule measurements with magnetic tweezers*, Review of Scientific Instruments, 2008

[53] A.J.W. te Velthuis, J.W.J. Kerssemakers, J. Lipfert, and N.H. Dekker, *Quantitative guidelines for force calibration through spectral analysis of magnetic tweezers data*, Biophysical Journal, 2015

[54] D. Dulin, T.J. Cui, J. Cnossen, M.W. Docter, J. Lipfert and N.H. Dekker, *High spationtemporal-resolution magnetic tweezers: calibration and applications for DNA dynamics*, Biophysical Journal, 2015

[55] E. Pfitzer, C. Wachauf, F. Kilchherr, B. Pelz, W. M. Shih, M. Rief and H. Dietz, *Rigid DNA beams for high-resolution single-molecule mechanics*, Angewandte Chemie, 2013

[56] F. Kriegel, N. Ermann, R. Forbes, D. Dulin, N.H. Dekker, J. Lipfert, *Probing the salt dependence of the torsional stiffness of DNA by multiplexed magnetic torque tweezers*, Nucleid Acid Research, 2017

[57] J.P. Cnossen, D. Dulin, N. H. Dekker, *An optimized software framework for real-time, high-throughput tracking of spherical beads*, Review of Scientific Instruments, 2014

[58] B. Liu and J. Liu, *Freezing directed construction of Bio/Nano interfaces: reagentless conjugation, denser spherical nucleid acids and better nanoflares*, Journal of American Chemical Society, 2017

[59] M.N. Dessinges, B. Maier, Y. Zhang, M. Peliti, D. Bensimon and V. Croquette, *Stretching single stranded DNA, a model polyelectrolyte*, Physical Review Letters, 2002

[60] M. T. Woodside, W. M. Behnke-Parks, K. Larizadeh, K. Travers, D. Herschlag and S. M. Block, *Nanomechanical measurements of the sequence-dependent folding landscapes of single nucleic acid hairpins*, Proceedings of the National ACademy of Science (PNAS), 2006 *digoxigenin* G.Neuert, C.Albrecht, E. Pamir and H.E. Gaub, *Dynamic force spectroscopy of the digoxigenin–antibody complex*, FEBS Letters, 2006

[61] S. Trachtenberg and I. Hammel, *Determining the persistence length of biopolymers and rod-like macromolecular assemblies from electron microscope images and deriving some of their mechanical properties*, Microscopy: Science, Technology, Applications and Education, 2010

[62] A. Brunet, C.Tardin, L. Salome, P.Rousseau, N.Destainville, and M. Manghi, *Dependence of DNA persistence length on ionic strength of solutions with monovalent and divalent salts: A Joint Theory Experiment Study*, Macromolecules, ACS, 2015

[63] H. Isambert, P. Venier, A.C. Maggs, A. Fattoum, R. Kassab, D. Pantaloni, M. Carlier, *Flexibility of actin filaments derived from thermal fluctuations*, Journal of Biological Chemistry, 1995

[64] P.Gutjahr, R.Lipowsky and J.Kierfeld, *Persistence length of semiflexible polymers and bending rigidity renormalization*, Europhysics Letters, 2006

[65] I. Usov and R. Mezzenga, *FiberApp: An Open-Source Software for Tracking and Analyzing Polymers, Filaments, Biomacromolecules, and Fibrous Objects*, Macromolecules, ACS, 2015

[66] D.J. Kauert, T. Kurth, T. Liedl and R. Seidel, *Direct mechanical measurements reveal the material properties of three-dimensional DNA origami*, Nanoletters, 2011

[67] T. Brouns, H. De Keersmaecker, S.F. Konrad, N. Kodera, T. Ando, J. Lipfert, S. De Feyter, and W. Vanderlinden, *Free energy landscape and dynamics of supercoiled DNA by high-speed Atomic Force Microscopy*, ACS Nano, 2018

[68] C.E. Castro, H.-J. Su, A. E. Marras, L. Zhou, J. Johnson, *Mechanical Design of DNA nanostructures*, The Royal Society of Chemistry, 2015

[69] K. Jahn, T. Torring, N.V. Voigt, R.S. Sorensen, A.L.B. Kodal, E.S. Andersen, K. V. Gothelf and J. Kjems, *Functional patterning of DNA origami by parallel enzymatic modification*, Bioconjugate Chemistry, 2011

[70] K.D. Bloch adn B. Grossmann, *Current protocols in molecular biology*, 1995

[71] S.B. Smith, Y. Cui and C. Bustamante, *Overstretching B-DNA: the elastic response of indiviudual double-stranded and single-stranded DNA Molecules*, Science, 1996

[72] A. Bosco, J. Camunas-Soler and F. Ritort, *Elastic properties and secondary structure formation of single-stranded DNA at monovalent and divalent salt conditions*, Nucleid Acid Research, 2013

[73] R. Roy, S. Hohng and T. Ha, *A practical guide to single molecule FRET*, Nature Methods, 2008

[74] B. Hellenkamp, S. Schmid, O. Doroshenko, O. Opanasyuk, R. Kühnemuth, S. R. Adariani, B. Ambrose, M. Aznauryan, A. Barth, V. Birkedal, M. E. Bowen, H. Chen, T. Cordes, T. Eilert, C. Fijen, C. Gebhardt, M. Götz, G. Gouridis, E. Gratton, T. Ha, P. Hao, C. A. Hanke, A. Hartmann, J. Hendrix, L. L. Hildebrandt, V. Hirschfeld, J. Hohlbein, B. Hua, C. G. Hübner, E. Kallis, A. N. Kapanidis, J.-Y. Kim, G. Krainer, D. C. Lamb, N. Lee, E. A. Lemke, B. Levesque, M. Levitus, J. J. McCann, N. Naredi-Rainer, D. Nettels, T. Ngo, R. Qiu, N. C. Robb, C. Röcker, H. Sanabria, M. Schlierf, T. Schröder, B. Schuler, H. Seidel, L. Streit, J. Thurn, P. Tinnefeld, S. Tyagi, N. Vandenberk, A. M. Vera, K. R. Weninger, B. Wünsch, I. S. Yanez-Orozco, J. Michaelis, C. A. M. Seidel, T. D. Craggs and T. Hugel, *Precision and accuracy of single-molecule FRET measurements—a multi-laboratory benchmark study*, Nature Methods, 2018

[75] J. J. McCann, U. B. Choi, L. Zheng, K. Weninger and M. E. Bowen, *Optimizing Methods to Recover Absolute FRET Efficiency from Immobilized Single Molecules*, Biophysical Journal, 2010

[76] C. Eggeling, J. Widengren, L. Brand, J. Schaffer, S. Felekyan and C. A. M. Seidel, *Analysis of Photobleaching in Single-Molecule Multicolor Excitation and Fo1rster Resonance Energy Transfer Measurements*, Journal of Physical Chemistry, 2006

[77] R.B. Mujumdar, L.A. Ernst, S.R. Mujumdar, C.J. Lewis, A.S. Waggoner, *Cyanine dye labeling reagents: sulfoindocyanine succinimidyl esters*, Bioconj Chem, 1993

[78] S. Preus, S. L. Noer, L. L. Hildebrandt, D. Gudnason and V. Birkedal, *iSMS: single-molecule FRET microscopy software*, Nature Methods, 2015

[79] J.D. Jackson, *Classical Electrodynamics*, Zanichelli, 2001

[80] U. Kreibig and M. Vollmer, *Optical Properties of Metal Clusters*, Springer, Berlin, Heidelberg, 1995

[81] C.F. Bohren and D.R. Huffman, Absorption and Scattering of Light by Small Particle, Wiley, New York, 1998.

[82] J. Stehr, C. Hrelescu, R.A. Sperling, G. Raschke, M. Wunderlich, A. Nichtl, D. Heindl, K. Kurzinger, W.J. Parak, T.A. Klar and J. Feldmann, *Gold nanostoves for microsecond DNA melting analysis*, Nanoletters, 2008

[83] L. Poon, W. Zandberg, D. Hsiao, Z. Erno, D. Sen, B.D. Gates and N.R. Branda, *Photothermal release of single-stranded DNA from the surface of gold nanoparticles through controlled denaturating and Au-S bond breaking*, ACS Nano, 2010

[84] F. Thibaudau, *Ultrafast photothermal release of DNA from gold nanoparticles*, ACS Publications, 2012

[85] M. Honda, Y. Saito, N.I. Smith, K. Fujita and S. Kawata, *Nanoscale heating of laser irradited single gold nanoparticles in liquid*, Optics Express, 2011

[86] H. Asanuma, Z. Jiang, K. Ikeda, K. Uosaki and H.Z. Yu, *Selective dehybridization of DNA-Au nanoconjugates using laser irradiation*, PCCP, 2013

[87] A.O. Govorov and H. H. Richardson, *Generating heat with metal nanoparticles*, NanoLetters, 2007

[88] L. Piantanida, D. Naumenko, M. Lazzarino, *Highly efficient gold nanoparticle dimer formation via DNA hybridization*, RSC Advances

[89] L.Piantanida, D.Naumenko, E.Torelli, M.Marini,D.M. Bauer, L.Fruk, G.Firrao and M. LazzarinoPlasmon resonance tuning using DNA origamiactuation*, Chemical Communication, 2015

[90] M. Honda, Y. Saito, N.I. Smith, K. Fujita and S. Kawata, *Nanoscale heating of laser irradiated single gold nanoparticles in liquid*, Optics Express, 2011

[91] O.A. Yeshchenko, I.S. Bondarchuk, V.S. Gurin, I.M. Dmitruk, A.V. Kotko, *Temperature dependence of the surface plasmon resonance in gold nanoparticles*, Surface Science, 2012

[92] O.A. Yeshchenko, N.V. Kutsevol and A.P.Naumenko, *Light-induced heating of gold nanoparticles in colloidal solution: dependence of detuning from surface plasmon resonance*, Plasmonics, 2016

[93] M. Reismann, J.C. Bretschneider, G. von Plessen and U. Simon, *Reversible Photothermal Melting of DNA in DNA-Gold Nanoparticle Networks*, Small, 2008

[94] X. Qu, D. Zhu, G. Yao, S. Su, J. Chao, H. Liu, X. Zuo, L. Wang, J. Shi, L. Wang, W. Huang, H. Pei and C. Fan, *An ExonucleaseIII-powered, on-particle stochastic DNA walker*, Angewandte Chemie, 2017

[95] A.J. Thubagere, W. Li, R.F. Johnson, Z. Chen, S. Doroudi, Y. Lim Lee, G. Izatt, S. Wittman, N. Srinivas, D. Woods, E. Winfree, L. Qian, *A cargo-sorting DNA robot*, Science, 2017

[96] C. Zhou, X. Duan and N. Liu, *A plasmonic nanorod that walks on DNA origami*, Nature Communications, 2015